Dissertation zur Erlangung des Doktorgrades

der Fakultät für Chemie und Pharmazie

der Ludwig-Maximilians-Universität München

Reactions of pnictogen hydrides under extra-terrestrial conditions and Matrix NMR Spectroscopy

Florian Tobias Zischka

aus

Dachau

2020

Erklärung

Diese Dissertation wurde im Sinne von § 7 der Promotionsordnung vom 28. November 2011 von Herrn Prof. Dr. Andreas Kornath betreut.

Eidesstattliche Versicherung

Diese Dissertation wurde eigenständig und ohne unerlaubte Hilfe erarbeitet.

München, den 28.04.2020

……..………………………

(Florian Zischka)

Dissertation eingereicht am 12.03.202

1. Gutachter Prof. Dr. Andreas Kornath

2. Gutachter Prof. Dr. Thomas Klapötke

Mündliche Prüfung am 28.04.2020

Erklärung zu Veröffentlichungen aus dieser Arbeit

Mein Doktorvater, Prof. Dr. Andreas Kornath, darf – unter Abgabe der Co-Autorenschaft an den Verfasser dieser Doktorarbeit – hieraus Daten verwenden und in wissenschaftlichen Zeitschriften veröffentlichen.

Danksagung

Mein besonderer Dank gebührt:

- Herrn Prof. Dr. Andreas Kornath für die interessante und herausfordernde Themenstellung, für die konstruktive Unterstützung bei der Anfertigung dieser Arbeit und für die gewährte sehr große Forschungsfreiheit.
- Herrn Prof. Dr. Klapötke für die Zweitbegutachtung der vorliegenden Arbeit.
- Herrn Prof. Dr. Karaghiosoff, Herrn Prof. Dr. Hartschuh, Herrn Prof. Dr. Böttcher und Herrn Prof. Dr. Evers für die Bereitschaft Teil der Prüfungskommission meines Rigorosums zu sein.
- Herrn Dr. Alexander Kaufmann und Herrn Dr. Michael Feller für die Einführung in die Matrix Isolationstechnik und die vielen interessanten Diskussionen bei der Optimierung der Matrix Isolations Apparatur.
- Herrn Dr. Thomas Bräuninger und Herrn Christian Minke für die Unterstützung bei allen Herausforderungen, welche die Festkörper NMR Spektroskopie für mich bereitgehalten hat.
- Frau Gabrielle Schmeißer, weil sie immer ein offenes Ohr und einen passenden Ratschlag parat hat.
- Meinen Arbeitskollegen Joe, Alan, Chris, Steffi, Marie, Manu, Domi, Yvonne, Ines, Basti und Alex für die gute Zeit, die wir zusammen hatten.
- Meinen Praktikanten Lukas, Helena, Sean, Andreas, Marlo und Marius für ihren tatkräftigen Beitrag zu dieser Arbeit.
- Meiner Freundin Freya, meinem Bruder Max und meinen Eltern für die ausdauernde Unterstützung während der Anfertigung dieser Arbeit.

Table of Contents

1 Introduction to Raman and NMR Matrix Isolation Spectroscopy

The investigation of intermediates or highly reactive molecules is an important part of research in modern natural sciences. These include, for example, free radicals, molecules in transition states and other highly reactive species. Their short life time is problematical, since it makes the characterization challenging. The matrix isolation technique, which was developed independently by *Pimentel* and *Porter* in 1954, offers the possibility to realize a characterization using different spectroscopic methods. [1-3] The basic idea of this method is to capture a reactive molecule at a low temperature in a rigid matrix that prevents further reactions and ensures sufficient substrate concentration for detection. [2, 4] *Pimentel* et al. lists the following key requirements for such a matrix material: [3]

1. *Inertness*: The matrix must be inert with respect to its reaction with the active species. Therefore, noble gases are often preferred.
2. *Rigidity*: The matrix must be sufficiently rigid to prevent diffusion of the active species. In addition, the matrix must be suitable for accommodating the active molecules.
3. *Transparency*: The matrix must not absorb in the spectral region of interest. Even a weak signal can interfere with a substrate signal of interest.

Noble gases meet the above requirements particularly well and are therefore preferred as host materials. For the preparation it is essential that the host material is vaporizable without decomposition. Furthermore, condensation at low temperatures on a cold surface must be possible.

For this, a low vapor pressure at the corresponding temperature must be present, otherwise the host cannot condense on the cold surface. Thus, a material-dependent upper temperature limit is 70 K for xenon, 35 K for argon and 30 K for nitrogen. [3]

In general for matrix isolation experiments a matrix to substrate ratio of about $\frac{1}{100}$ to $\frac{1}{5000}$ is chosen. [5] The substrate species is enclosed by the host lattice and is thus isolated from other reactive species due to its rigidity and cryogenic temperature, which suppresses the diffusion. This prevents the reaction of the species with each other as well as a disturbance by undesired foreign molecules and a reaction of these with the guest species to be investigated. However, the mobility of the guest species can be increased by selective heating to higher temperatures, the so-called tempering or annealing, which enables a certain diffusion and controlled reactions.

Depending on the problem and the technical equipment, different analytical methods can be used. UV and infrared spectroscopy are most frequently chosen due to their high sensitivity and applicability in the gas phase. [6] The spectroscopic methods, Raman and NMR spectroscopy, used in the course of this dissertation are rather uncommon analytical methods for matrix isolation experiments. If the *scifinder* database is searched with the term “Matrix Isolation Spectroscopy” only 10% of the results concern Raman spectroscopy and merely 1% relates to NMR spectroscopy. An overview of the analysis techniques of a *scifinder* search for the term “Matrix Isolation Spectroscopy” is given in FIG. 1. [7]

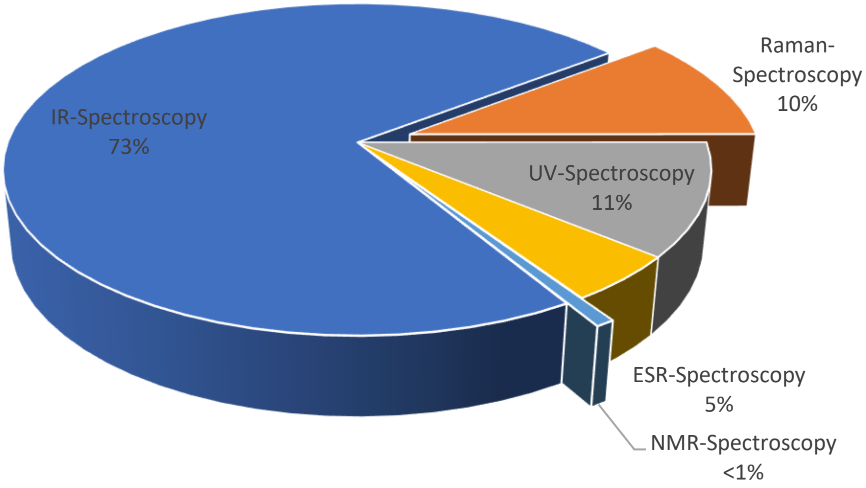

FIG. 1: Types of spectroscopy used in matrix isolation experiments.

1.1 Raman Spectroscopy

Investigation of molecular vibrations began in 1801 with the discovery of infrared radiation by *F.W. Herschel*. Nevertheless, the systematic evaluation of vibrational spectra remained a highly challenging task for a long time. [8] More than one hundred years after the discovery of the Raman effect by *C.V. Raman*, the present day vibrational spectroscopy began. [8] For his discovery he was awarded the Nobel Prize in Physics in 1930. [9]

When *Raman* began his experiments, the effect of the molecular tidal radiation postulated by *Lord Rayleigh*, today known as Rayleigh scattering, was already discovered. [10] *Raman* studied this effect not only in white light, but first used a light filter which was only transparent for the violet end of the spectrum and later a mercury vapor lamp. [10] When scattering light on liquid benzene, he noticed that the scattered light contained several frequency shifted lines. [9] At the beginning it was suspected that the samples were fluorescent. The decisive proof for a new kind of radiation was finally provided by the observation of the scattering behavior of N_2O and CO_2. Here, the Raman lines appear in a spectral range in which fluorescence is excluded. [10]

The first experiments employing Raman laser spectroscopy in matrix isolation experiments were performed by *Nibler* and *Coe* [11], *Shirk* and *Claasen* [12] and *Ozin* and co-workers [13] in 1971. Many of the Raman matrix isolation studies are based on special Raman effects, such as stimulated Raman spectroscopy (SRS), in order to overcome detection problems resulting from the low sensitivity of Raman spectroscopy. [14] The application of resonance Raman spectroscopy is another possibility to solve this problem. [15-17] Moreover, Multi-Channel Raman Matrix Isolation Spectroscopy was invented in 1997 by *Kornath*. It is capable to detect species in high dilutions in a region from 20 cm^{-1} to 5000 cm^{-1} at moderate integration times, without external excitation. In the course of this PhD study Multi-Channel Raman matrix Isolation Spectroscopy was used to investigate the reaction behavior of pentel hydrides with hydrogen halides, in order to mimic extra-terrestrial atmospheric conditions (see Chapter 2 “Pnictogen Hydrides and Hydrogen Halides under Extra-Terrestrial Conditions”). Moreover, it was used to investigate the reaction behavior of thermalized arsine (see Chapter 3 “Investigation on the Dimerization of Arsanyl in noble Gas Matrices (Prepared Manuscript)”).

1.2 NMR Spectroscopy

Only few groups have studied matrix isolated samples with NMR spectroscopy so far. To our knowledge, the first published study is the matrix isolation of HCl and $(HCl)_2$ in argon by *White* and his co-workers in 1978. [18] Further early examples are studies by *Grant* and *Michel*, presenting a ^{13}C NMR spectrum of a mixture of ethylene, ethane and methane or ethylene in argon. [19] Further studies were reported by *White.* [20, 21] All the approaches have in common, that they attempt to build an NMR spectrometer around a cold surface. Here, the sample is condensed on the surface during the experiment (FIG. 2). Apart from those, only very few further publications exist that treat matrix isolation studies. [22-28]

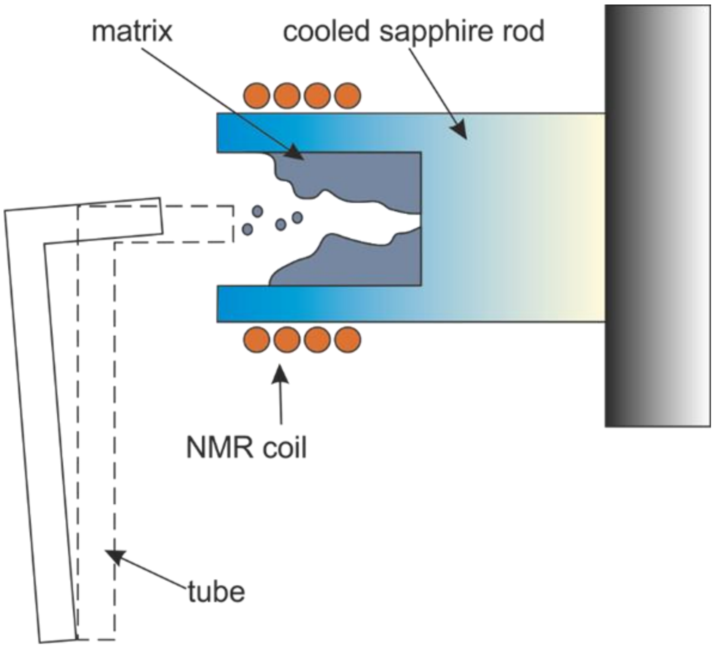

FIG. 2: Concept drawing of the apparatus used in the mentioned matrix isolation experiments employing NMR spectroscopy.

In 2009 *Kaufmann* started to study a new approach to achieve matrix isolation conditions applicable to NMR spectroscopy. The method employs adamantane instead of noble gases as the host material. [29] Consequently, the rigidity of the matrix is also maintained at higher temperatures. In the course of this PhD project the mobility of white phosphorus and its thermalization products inside the adamantane matrix are studied and discussed in relation to *Kaufmann's* results in CHAPTER 4 ("Spectroscopic Studies of Di- and Tetra-Phosphorus in Adamantane Matrices – an approach to room temperature stable matrices. (Prepared Manuscript)").

2 Pnictogen Hydrides and Hydrogen Halides under Extra-Terrestrial Conditions

2.1 Introduction

The composition of Saturn and Jupiter's atmospheres is well investigated by several probes and space missions. The major part of their atmosphere consists of hydrogen and helium, though further compounds have been identified in minor concentrations. Examples are pnictogen hydrides and hydrogen halides. In TABLE 1 a comprehensive overview of compounds detected by space missions or probes is given.

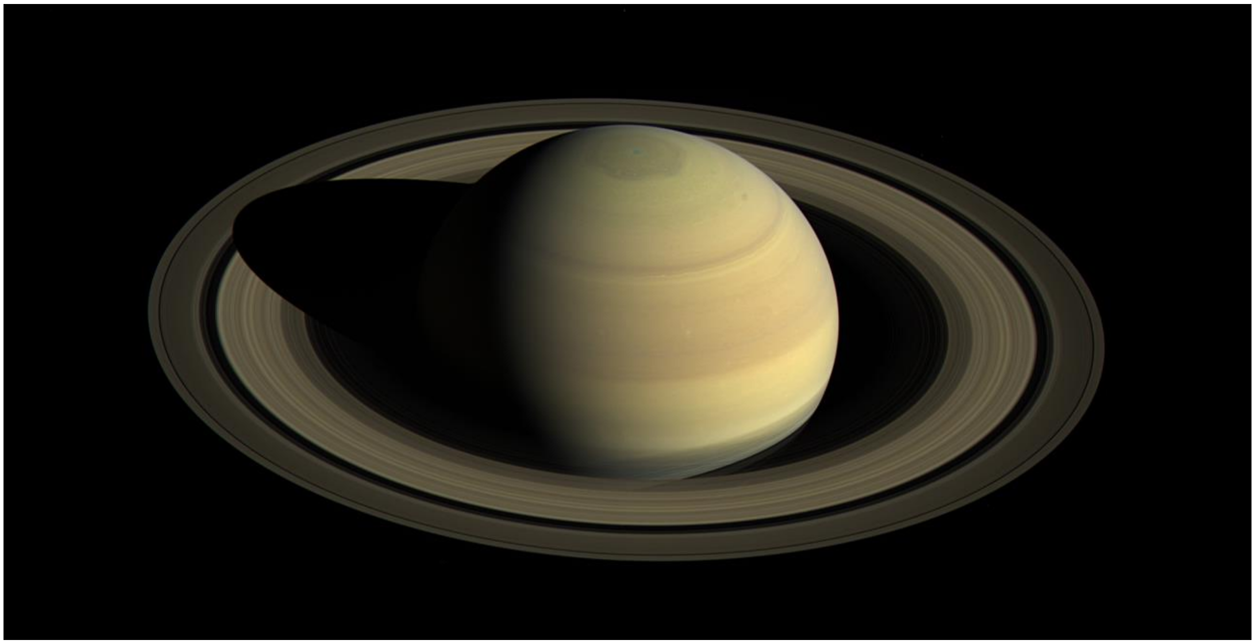

FIG. 3: Picture of Saturn by the NASA space probe Cassini from 2016, published by the *NASA Jet Propulsion Laboratory; California Institut of Technology* showing the northern hemisphere of the gas giant. [30]

TABLE 1: Composition of the atmospheres of Saturn und Jupiter. [31-33]

Compound	Composition Saturn		Composition Jupiter	
H_2	96.00	%	86.20	%
He	3.00	%	13.60	%
CH_4	0.40	%	0.21	%
NH_3	0.01	%	0.025	%
PH_3	4.00	ppm	60.00	ppm
H_2S	-	%	77.00	ppm
C_2H_6	0.10	ppm	4.00	ppm
C_2H_2	3.50	ppm	0.20	ppm
CH_3CCH	0.60	ppb	-	%
C_4H_2	90.00	ppt	-	%
H_2O	1015	molec/cm^2	1015.00	molec/cm^2
CO_2	$3*10^{14}$	molec/cm^2	$3*10^{14}$	molec/cm^2
AsH_3	3.00	ppb	0.30	ppb
GeH_4	0.40	ppb	0.70	ppb
HF	8.00	ppt	27.00	ppt
HCl	67.00	ppt	2.30	ppb
HBr	130.00	ppt	1.00	ppb
HI	1.40	ppb	7.60	ppb

The coexistence of NH_3, PH_3 and AsH_3 with hydrogen halides raised our interest, as these compounds are known to eventually yield onium salts under laboratory conditions. [31-33] While the ammonium salts are stable, which is based on the *Brønsted* basicity of ammonia (pK_B=4,75), their heavier homologs are unstable. [34] The most stable example, $PH_4^+ I^-$ is known to decompose at a pressure of 70 mbar. This behavior is caused by the considerably lower *Brønsted* basicity of phosphine (pK_B=26). [34, 35] Similarly, the products of the co-condensation of arsine and HBr or HI are even less stable and decompose at −103°C and −123°C. [35]

The mean temperatures of Saturn and Jupiter are −139°C and −108°C respectively on the zero-elevation surface. For a gas planet, this is the level at which the gas pressure is 1 bar. Jupiter's zero-elevation level is located at an altitude of 71392 km at the equator. At higher altitudes of the atmosphere the respective temperatures are lower. Jupiter, for example, has a temperature of −161 °C at a pressure of 0.1 bar. [36]

Taking the decomposition temperatures of the onium halides and the temperatures of the gas giants into consideration, we decided to investigate whether the formation of such halides is possible in their atmospheres. Here, special focus is put on the relation of the pK_B values and the period of the pnictogen atom. In the course of our studies, three different experimental systems have been studied under matrix isolation conditions by Raman spectroscopy. These systems are AsH_3 - HX, PH_3 - HX (X = F, Br) and SbH_3 - HF. At first, each experiment is discussed separately in the Chapters 2.2, 2.3 and 2.4. In a second step all experiments are discussed with regard to each other in the Chapter 2.5 "Theoretical comparative studies on the System PnH_3 – HX (Pn = P, As, Sb; X = F, Br)".

2.2 Raman Matrix Isolation Study on the System AsH_3 – HF (Prepared Manuscript)

Florian Zischka,[1] Andreas V. Hulm,[1] Sean Hartmann[1] and Andreas J. Kornath,[1a]

[1] *Inorganic Chemistry, Department of Chemistry, Ludwig-Maximilians-University Munich, Butenandtstr. 5-13-(D) in 81377 Munich, Germany*

Abstract: Noble gas matrices containing AsH_3 and HF were prepared by co-condensation on a cold surface at 10 K and investigated by Raman spectroscopy. The Raman spectra indicate the formation of a new species. The molecules AsH_4^+, AsH_4F, AsH_2^+ and AsH_2F are discussed as reaction products. The analysis of the spectra proves the existence of AsH_2^+ and AsH_2F. The antisymmetric and symmetric As-H stretching modes of AsH_2^+ are observed at 2184 cm^{-1} and 2173 cm^{-1}. At lower dilutions in argon and xenon matrices the formation of AsH_2F is achieved (ν_{as} = 2116 cm^{-1}, ν_s = 2107 cm^{-1}). The observations are verified by deuterium substitution experiments showing redshifted As-D stretching modes, which agree with the H/D isotopic effect. [8] The vibrational frequencies are compared to vibrational frequencies calculated on the CCSD/aug-cc-pvtz level of theory. An intermolecular H_2 elimination pathway, including two possible transition states, is discussed theoretically at the MP2/aug-cc-pvtz level of theory.

2.2.1 INTRODUCTION

Saturn and Jupiter are the two heaviest planets of our solar system. Saturn is 95 times heavier than earth. Jupiter is even more than three times heavier than Saturn. Both planets have been the destination of many space missions in recent history. Until today, eight space probes have orbited or passed the two gas giants. The last probes which passed or orbited Saturn and Jupiter were Cassini–Huygens and the New Horizon Space mission. The composition of the atmosphere of the planets has been studied by these space missions as well as spectroscopically by observations from earth. The main components of the atmosphere are hydrogen and helium. Jupiter contains 15.7% and Saturn contains 3.4% of helium. [37] In addition, the existence of further elements and molecules in minor concentrations has been proven. [38, 39] In 1991, *Noll* and *Larson* showed by 4.5 to 5.0 µm microwave spectroscopy that the mole fraction of AsH_3 is about 3 ppm in Saturn’s atmosphere and about one order of magnitude lower in Jupiter’s atmosphere. The abundances of the elements As and P has been linked to the solid components of the solar nebula. [38] Hydrogen fluoride was also detected by the Cassini/CIRS mission on Jupiter and Saturn in reasonable concentrations. [32, 33] In Jupiter’s atmosphere 27 ppm of HF were measured, whilst Saturn’s atmosphere merely contains 8 ppm of HF. Especially the existence of hydrogen fluoride and AsH_3 attracted our attention, because laboratory experiments and infrared spectra at approximately 80 K have already proven that the arsonium halide salts, $AsH_4^+\ Br^–$ and $AsH_4^+\ I^–$ can be formed by co-condensation of arsine and the corresponding hydrogen halide. [40] Jupiter, for example, has a temperature of approximately 113K C at a pressure of 0.1 bar. [36] In contrast to the room temperature stable $PH_4^+\ I^–$, which is the most stable of the onium halides besides $NH_4^+\ I^-$, arsonium iodide decomposes at 190 K. [40] Furthermore, the analogous bromide compound $AsH_4^+\ Br^–$ is stable up to 150 K. [40] In general, the phosphonium salts are substantially more stable, than the corresponding arsonium salts. [35] To our knowledge, no reactions of arsine with pure HF have been described in literature. Only reactions of arsine with anhydrous hydrogen fluoride and the presence of a Lewis acid have been reported yet. In the respective superacidic solution of Hydrogen fluoride and metal fluorides the corresponding salts AsH_4^+ MF_6^- (M=As, Sb) and AsH_4^+ $Ta_2F_{11}^-$ are formed. [41, 42] These observations prompted us to investigate whether an arsonium fluoride can be formed under extra-terrestrial conditions like in Saturn's or Jupiter's atmosphere.

2.2.2 EXPERIMENTS

2.2.2.1 Apparatus and Materials

The Multi-Channel Raman matrix Isolation Spectroscopy apparatus and the general procedure are described in detail elsewhere. [43] Argon (99.9996%) and nitrogen (99.996%) (Messer Griesheim) was dried over P_4O_{10}. Xenon (99.99%) was used without further purification. AsH_3 was synthesized from Zn_3As_2 and diluted sulfuric acid as described in the literature. [44] For the deposition experiments, the gas mixture was expanded from an apparatus consisting of a reservoir steel cylinder, a regulation valve and a pressure sensor (MKS Baratron) into to the matrix isolation apparatus (see supporting information for detailed description). The reservoir contained an AsH_3 and HF or DF mixture with a ratio of 1 to 1.1. Synthesis and handling of AsH_3 and HF or DF was performed by employing standard Schlenk techniques and a stainless steel vacuum line.

The matrix layers were prepared by continuous injection of the AsH_3/HF or AsH_3/DF mixture into a noble gas flow and subsequent condensation on the cold tip. The ratio is referred to as S/M, meaning arsenic species to noble gas in a molar ratio. The inert gas flow of approximately 4 mmol (100 cm^3 at standard temperature and pressure) at a flow rate of 3 mmol/h (75 cm^3/h) was controlled by a needle valve. The AsH_3/HF or AsH_3/DF mixture was filled in a small separate volume of approximately 20 ml every five minutes. The decrease of the pressure in the separate expansion vessel was monitored in order to calculate the S/M ratio. The average thickness of the layers deposited on the 10 K cold tip was approximately 100 µm. If required, a layer of nitrogen for the calibration of the Raman spectrometer was added on top of the deposited matrix layers. A drawing of the apparatus is shown in the supporting information (FIG S. 2). After a deposition time of one and a half hours, a white homogenous layer had formed. Annealing cycles of the argon matrices showed no influence on the Raman spectra until 45 K. After the spectroscopic measurements it has been observed that evaporation of the matrix layer, leads to remained arsenic as a metallic residue on the cold tip, due to the at least partial decomposition of the arsenic species. For the Raman spectroscopy, a CCD Raman spectrometer (Jobin-Yvon T64000) was used, equipped with a frequency doubled Nd:YAG DPSS laser (Cobolt 05-01 Series Samba; 532 nm) as the light source.

2.2.2.2 Computational Methods

The optimized geometries and vibrational frequencies for all arsenic hydrogen species were calculated using the Coupled Cluster Singles and Doubles (CCSD) post Hartree Fock coupled cluster method. [45-49] All Raman intensities and the geometry optimization used for the elimination pathway calculations were conducted employing second order *Møller Plesset* perturbation theory (MP2). [50-55] In all calculations the triple zeta *Dunning's* correlation-consistent basis set, augmented with diffuse orbitals (aug-cc-pvtz) was used. [56-61] All methods are implemented in the program package GAUSSIAN 09. [62] All vibrational frequencies are scaled by an empirical factor of 0.95.

2.2.3 RESULTS AND DISCUSSION

2.2.3.1 Theoretical Considerations

For the analysis of the experimental results several reaction products must be considered. The first one is the tetrahedral arsonium cation, which is formed by the protonation of arsine by hydrogen fluoride. The second possibility is the formation of a covalent arsonium fluoride, with the point group C_{3v}. In a subsequent reaction step the decomposition of the arsonium species into fluoro arsine, AsH_2F or $AsH_2^+F^-$ can occur. The existence of AsH_2F has to be considered since fluoro arsine already has been observed by *Lester Andreas via* fluorination of arsine in an argon matrix. [63] The decomposition of AsH_4^+ or AsH_4F may take place by a hydrogen elimination. For a better understanding of the elimination, the decomposition of AsH_4^+ and AsH_4F was simulated with *Gaussian09*. [62] The optimizations and the energy calculations of the stationary points were conducted at the MP2/aug-cc-pvtz level of theory. The vibrational analysis of the stationary points on the hypersurface marking the transitions states, exhibits a single negative frequency as expected. Because of the high symmetry of AsH_4^+, all hydrogen atoms are indistinguishable, and it is therefore irrelevant which hydrogen atoms are approaching each other in order to form the arsine-like transition state. However, the reaction is endothermic with 173 kJ/mol and exhibits a high activation barrier of 209 kJ/mol. (FIG. 4)

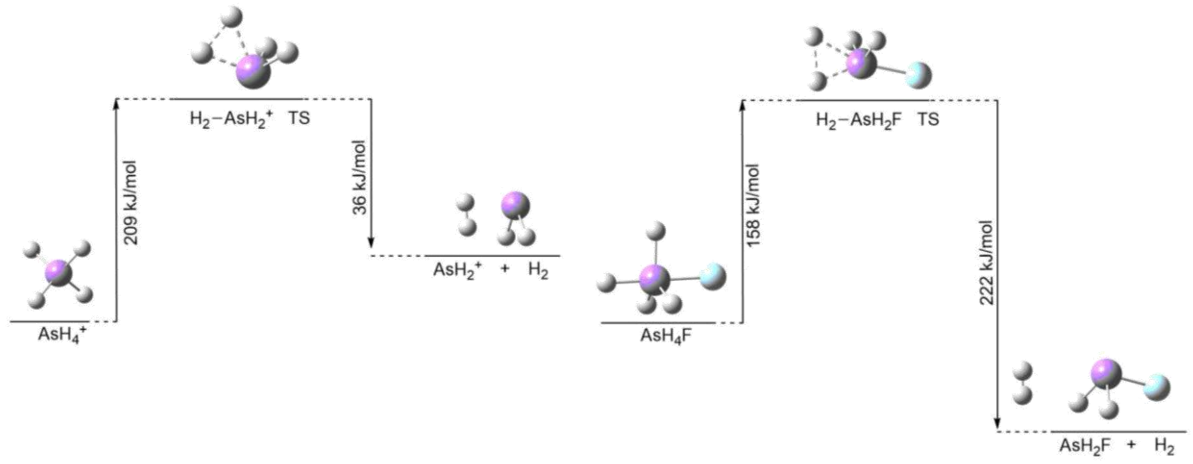

FIG. 4: Reaction pathways and transition states (TS) for the hydrogen elimination and the formation of AsH_2^+ and AsH_2F, respectively.

The formation of hydrogen from AsH_4F is more complex. Altogether, it is possible to either form hydrogen inside the H-As-H plane of the bipyramid or by the approach of one hydrogen atom in the plane towards the hydrogen on the top of the pyramid. The angle, which separates the two atoms in the plane is 120° and the axial angle is only 90°. Therefore, a mechanism *via* the second option is supposed. As expected, only one true transition state can be estimated for option 2. According to the quantum chemical calculations, the reaction is exothermic with 64 kJ/mol in the gas phase. Although the activation barrier of the reaction is 158 kJ/mol, it was taken into consideration for the analysis of the Raman data. Overall, in the present study the vibrational frequencies of the following species are taken into consideration: AsH_3, AsH_4F, AsH_4^+, AsH_2F and AsH_2^+. The formation of AsH_2^+ or AsH_2F is discussed in Chapter 2.5.3.4 in detail.

2.2.3.2 Calculated Vibrational Frequencies

The calculated vibrational frequencies of the arsine hydrogen species are summarized in TABLE 2 and TABLE 3. The quantum chemical calculations at the CCSD/aug-cc-pvtz level of theory predict the As-H stretching vibrations of arsine at 2171 cm^{-1} and 2146 cm^{-1}. Compared to the experimental values of 2123 cm^{-1} and 2116 cm^{-1}, which are found by gas phase IR spectroscopy, they are slightly overestimated but still in reasonable agreement. [64] The antisymmetric and symmetric H-As-H bending vibrations are predicted at 990 cm^{-1} and 892 cm^{-1}, respectively. Experimental values of 1003 cm^{-1} and 906 cm^{-1} show that the As-H bending modes are underestimated by the calculations only by 13 cm^{-1} and 14 cm^{-1} respectively. [64] The overestimation of the As-H stretching modes and underestimation of the As-H bending modes is observed for all discussed arsenic hydrogen species.

Compared to the As-H stretching vibrations of arsine, the As-H valence modes of AsH_4^+ are shifted to higher wavenumbers by about 180 cm^{-1} and are observed at 2348 cm^{-1} and 2321 cm^{-1}. A discussion of the reason for the observed blueshift is presented later in Chapter 2.2.3.3. Like for the arsonium cation, the As-H stretching modes of AsH_2^+ are expected to be shifted to higher wavenumbers, compared to the As-H valence modes of arsine and are predicted at 2176 cm^{-1} ($\nu_{as)}$ and 2156 cm^{-1} (ν_s). The most characteristic mode of the deuterium isotopomeric species is the As-D stretching vibration, which is found at 1540 cm^{-1} (AsH_2D), 1663 cm^{-1} (AsH_3D^+) and 1542 cm^{-1} ($AsHD^+$). The vibrational data of the deuterium isotopomeric species is summarized in TABLE 3.

TABLE 2: Calculated and literature-known vibrational data of AsH_3, AsH_4^+ and AsH_2^+. Vibrational frequencies calculated on the CCSD/aug-cc-pvtz level of theory.

Assignment	Vibrational Frequencies [cm^{-1}]				
	AsH_3		AsH_4^+		AsH_2^+
	calc.[a]	Lit. (gas) [64]	calc. [a]	Lit. (AsF_6^-) [65]	calc. [a]
ν_{as} (AsH)	2171	2123	2348	2341	2176
ν_s (AsH)	2146	2116	2301	2321	2156
δ_{as} (AsH_2)	990	1003	996	1024	
δ_s (AsH_2)	892	906	854	941	981

[a] scaled with an empirical factor of 0.95

TABLE 3: Calculated data of AsH_2D, AsH_3D^+ and $AsHD^+$. Vibrational frequencies calculated on the CCSD/aug-cc-pvtz level of theory.

Assignment	Vibrational Frequencies [cm^{-1}]			
	AsH_2D calc. [a]	Assignment	AsH_3D^+ calc. [a]	$AsHD^+$ calc.
ν_{as} (AsH)	2171	ν_{as} (AsH)	2348	2165
ν_s (AsH)	2155	ν_s (AsH)	2313	
ν (AsD)	1540	ν (AsD)	1663	1542
δ_s (AsH_2)	969	δ_{as} (AsH_2)	959	
δ_{as} (AsH_2D)	855	δ_s (AsH_2)	854	
δ_s (AsH_2D)	794	δ (AsHD)	739	852

[a] scaled with an empirical factor of 0.95

For the calculated molecules AsH_4F and AsH_2F, the vibrational frequencies are listed in TABLE 4. Three observable As-H valence modes of arsonium fluoride (C_{3v}) are expected, which are all Raman active. The As-H valence modes in the plane of the bipyramid are predicted at higher wavenumbers as the axial As-H stretching mode. The As-F vibration is anticipated at 483 cm^{-1} by quantum chemical calculations.

The antisymmetric and the symmetric As-H valence modes of AsH_2F are expected at 2145 cm^{-1} and 2129 cm^{-1} respectively and are shifted to lower wavenumbers in comparison to the As-H valence modes of AsH_2^+. The ν (As-F) is predicted at 654 cm^{-1}. For the deuterated isotopomer AsHDF, the calculations predict the A-H valence mode at 2178 cm^{-1} and the As-D valence mode at 1522 cm^{-1}. In comparison to AsH_2F, the As-F stretching mode remains the same and for AsHDF and it is calculated at 657 cm^{-1}. All vibrational data concerning AsH_4F, AsH_2F and AsHDF is summarized in TABLE 4.

TABLE 4: Summarized calculated and literature-known vibrational data of AsH_4F, AsH_2F and AsHDF. Vibrational frequencies calculated on the CCSD/aug-cc-pvtz level of theory.

	AsH_4F		AsH_2F			AsHDF	
Assignment	calc. [a]	Assignment	calc. [a]	lit. [63]	Assignment	calc. [a]	lit. [63]
ν_{as} (AsH)	2294	ν_{as} (AsH)	2145	2117	ν (AsH)	2178	2113
ν_s (AsH)	2245	ν_s (AsH)	2129	2108	ν (AsD)	1522	1522
ν (AsH)	2010	δ_s (AsH_2)	980	984	δ (AsHD)	851	
δ (AsH)	1135	δ_s (AsHF)	814	842	δ (AsHF)	799	
δ_{as} (AsH)	990	δ_{as} (AsHF)	782		ν (AsF)	657	654
δ_s (AsH)	814	ν (AsF)	654	649	δ (AsDF)	577	
δ (AsH)	517						
ν (AsF)	483						

[a] scaled with an empirical factor of 0.95

2.2.3.3 Structure of the considered arsenic Species

The structures of AsH_4^+, AsH_2^+, AsH_2F and AsH_3 were calculated with the post Hartree Fock Method CCSD and with the correlation consistent basis set aug-cc-pvtz, which is known to yield precise results for small to medium sized molecules. [45, 57] The calculated geometry parameters of the discussed species are summarized in TABLE 5. The calculation of the structure of arsine was used to verify the applicability of the mentioned level of theory by comparison with experimental results. The molecular structure of arsine has been investigated by gas electron diffraction (GED) by *Noble*. [66] In the GED experiment, an As-H bond length of 1.503(2) Å and a H-As-H angle of 93.2(9)° were observed. The calculations on the CCSD level of theory yield an As-H bond length of 1.508 Å, which is within three standard deviations (Ω) of the experimental value, and a H-As-H angle of 92.6°, which is within one Ω of the experimental value. In conclusion, the chosen level of theory reproduces the experimental results well. In AsH_3, the H-As-H angle is close to 90°, which is different from the H-N-H angle in NH_3 of 107.8°. According to chemical behavior of second row main group elements, the formation of four equivalent sp^3-hybrid orbitals, which widen the H-As-H angle up to the tetrahedron angle like in NH_3, is expected. Nevertheless, this rule cannot be transferred to heavier pnictogen hydrides, showing a reduced trend to isovalent hybridization. According to *Kunzelnigg*, the distance of the s-AOs and p-AOs to the atom core and the consequent enlargement of the valence angle, which causes a reduction of the *Pauli* repulsion, are decisive for the hybridization manner. [67] Compared to NH_3, the 4p-AOs of arsine are locates significantly more distant from the atom core than the 4s-AOs. Consequently, the *Pauli* repulsion in AsH_3 between the As-H bond is lower than between the N-H bonds in NH_3. As a result, AsH_3 is less likely to form hybrid orbitals.

In order to form the arsonium species by protonation of AsH_3, the generation of a fourth binding site is required. Consequently, the 4s-AO must be promoted to a higher level of energy and four equivalent sp^3-hybrid orbitals have to be formed with a widened H-As-H angle. According to the quantum chemical calculations, the arsonium cation is predicted as a tetrahedron with an As-H bond length of 1.475 Å and a H-As-H angle of 109.5° like in an ideal tetrahedron. As a result, AsH_4^+ must have four sp^3-hybrid valence orbitals. Compared to AsH_3 the s-orbital proportion in the valence orbitals of the arsonium cation is increased, which leads to a shortening of the As-H bond and as a consequence the As-H valence modes are shifted to higher wavenumbers. The blueshift and the associated strengthening of the As-H bond of arsine by its protonation is an unusual behavior. Nevertheless, the blueshift of the tetrahedral arsonium cation and pnictogen cations in general is also reported in the literature by experiments in superacidic solutions or by co-condensation experiments. [40, 68] In case of the

AsH_4^+ AsF_6^- salt, the As-H stretching vibrations are detected at 2341 cm^{-1} and 2321 cm^{-1}, respectively.

TABLE 5: Geometric parameters of AsH_4^+, AsH_3, AsH_2^+ and AsH_2F calculated at the CCSD/aug-cc-pvtz level of theory.

	Point group	Bond length [Å]	Bond angle
AsH_3	C_{3v}	As-H: 1.508	H-As-H: 92.6°
AsH_2^+	C_{2v}	As-H: 1.514	H-As-H: 91.7°
AsH_2F	C_s	As-H: 1.513 As-F: 1.745	H-As-H: 91.6° H-As-F: 95.4°
AsH_4^+	T_d	As-H: 1.475	H-As-H: 109.5°

Compared to AsH_4^+, the As-H bond (1.514 Å) of the AsH_2^+ is elongated, which is consistent with the shift to lower wavenumbers of the H-As stretching modes. The H-As-H angle of AsH_2^+ (C_{2v}) is 91.7°.. Furthermore, the As-H bonds are slightly elongated. The length of the As-H bond and the H-As-H angle remain unchanged irrespective whether AsH_2^+ is simulated as a naked cation or as AsH_2F. The As-F bond of 1.475 Å is expected to be shorter than the As-F bond of AsF_3 with 1.706 Å. [69] Nevertheless, the As-F bond of AsH_2F is a regular As-F single bond. [70]

2.2.3.4 Raman Spectra of the System AsH_3 − HF

For the matrix deposition experiments dilution series of AsH_3 with and without HF in argon, noble matrices with a S/M ratio from 1/10 to 1/100 were condensed and Raman spectroscopically investigated. The vibrational frequencies are summarized in TABLE 6 and are depicted in FIG. 5. For the sake of completeness, it has to be stated, that in the Raman experiments two of the vibrational modes of the As_4 tetrahedron are detected at 357 cm^{-1} and 254 cm^{-1}, which are not depicted in FIG. 5.

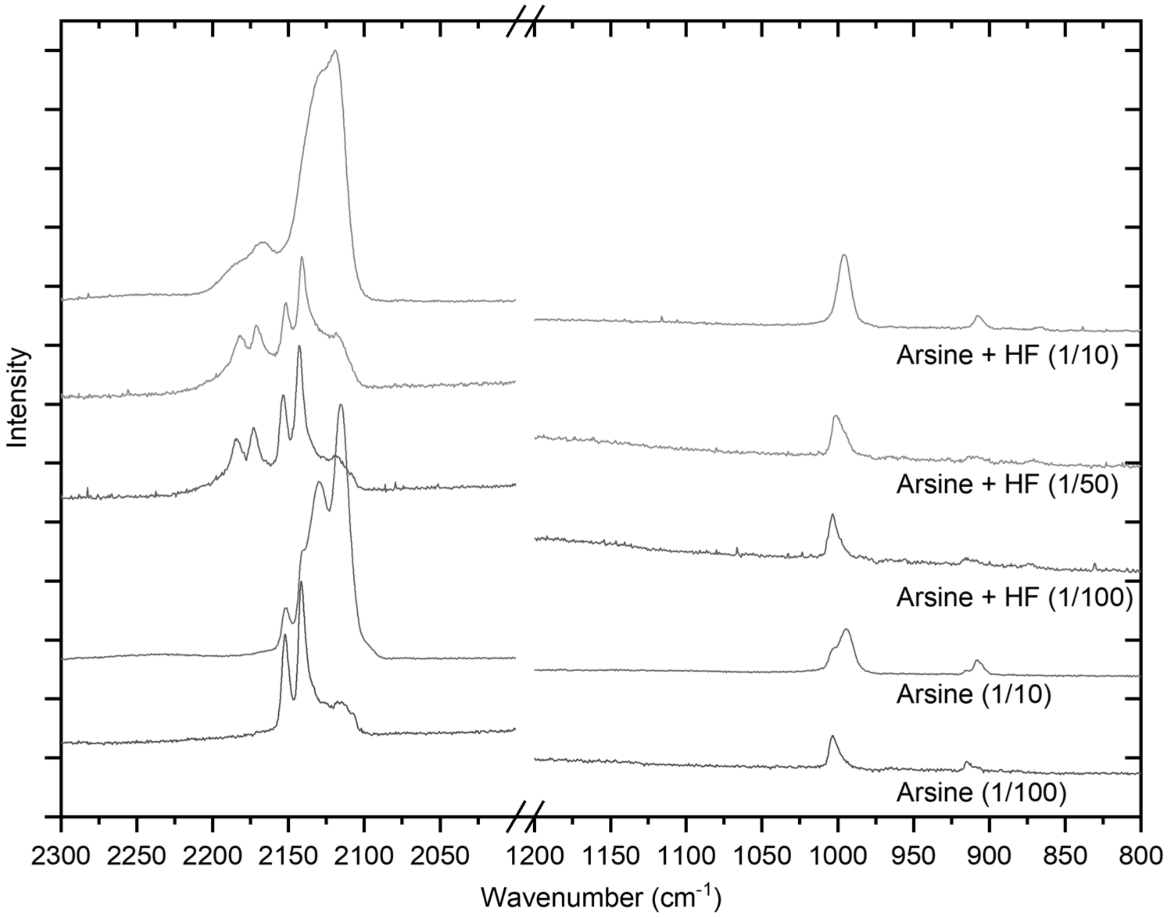

FIG. 5: Raman matrix spectra of AsH_3 co-condensed with and without HF in argon at 10 K (experimental conditions: 100 μm layer, laser wavelength 532 nm, laser power 1000 mW, Raman intensity is normalized).

The antisymmetric and symmetric As-H valence modes of arsine in argon matrices are observed at 2152 cm^{-1} and 2142 cm^{-1}, respectively. The antisymmetric and symmetric As-H bending modes of AsH_3 are detected at 1003 cm^{-1} and 915 cm^{-1}. At lower dilutions (arsine / argon 1/10) the As-H valence modes of AsH_3 are red-shifted. Here, the symmetric and antisymmetric As-H stretching modes are observed at 2130 cm^{-1} and 2116 cm^{-1}, respectively and the antisymmetric and symmetric As-H bending modes are detected at 994 cm^{-1} and 908 cm^{-1}. This red-shift from experiment Arsine + HF / Argon (1/100) to Arsine + HF / Argon (1/10) in FIG. 5 of up to 24 cm^{-1} can be explained by the increased interactions between the AsH_3 molecules.

The first As-H species to be discussed in this context is AsH_4^+. The two As-H valence modes of AsH_4^+ are predicted at 2348 cm^{-1} and 2301 cm^{-1}, by quantum chemical calculations. Therefore, the As-H stretching modes of AsH_4^+ are expected to be blue-shifted by more than 180 cm^{-1} compared to the antisymmetric As-H stretching vibration of arsine. No vibrational modes are detected at wavenumbers higher than 2184 cm^{-1}. In addition, no Raman lines can be attributed to the H-As-H deformation modes of AsH_4^+. Therefore, the formation of AsH_4^+ can be excluded for the system AsH_3 – HF. Further experimental information on AsH_4^+ is given in the experiment of the system AsH_3 – HBr, which is discussed in Chapter 2.2.3.6.

Even though AsH_4^+ is absent in the Raman spectra, the possible existence of the arsorane structure AsH_4F must be taken into consideration. According to calculations the two in-plane As-H stretching modes of AsH_4F are predicted at slightly lower wavenumbers than the corresponding As-H modes of AsH_4^+ at 2348 cm^{-1} and 2301 cm^{-1}. The third As-H valence mode is expected to be observed at 2009 cm^{-1}. However, none of the predicted valence and deformation modes of the arsorane are detectable in the course of the matrix isolation experiments. Taking all observations into consideration, the arsorane species as well as AsH_4^+ are not formed from arsine and hydrogen fluoride under the conditions of the experiment.

As discussed in the theoretical part 2.2.3.2, the As-H valence modes of AsH_2^+ and AsH_2F are expected at higher wavenumbers than the two As-H valence modes of arsine. In the course of the AsH_3 - HF dilution series experiments, the ν_{as} (As-H) of AsH_2^+ is observed at 2184 cm^{-1} and the ν_s at 2173 cm^{-1}. The H-As-H deformation mode is superimposed with the antisymmetric H-As-H deformation mode of arsine at 998 cm^{-1}. At a higher S/M ratio of 1/10, new broadened Raman lines are observed in superposition with the As-H valence modes of arsine. In experiments employing xenon as host material, these vibrational modes are distinguishable from the valence modes of arsine. The spectra are depicted in FIG S. 1 in the supporting information. The broadened Raman lines are assigned to the As-H valence modes of AsH_2F. The precise frequencies of 2116 cm^{-1} for the ν_{as} and 2107 cm^{-1} for the ν_s are derived from experiments in xenon and are in good agreement with the observations of *Lester Andrews*. [63] The δ (H-As-H) of AsH_2F is observed in superposition with the δ_s (H-As-H) of AsH_3 at 995 cm^{-1}. Additional bending modes of AsH_2F are detectable in the isotopic exchange experiments and are discussed in the following chapter.

2.2.3.5 Raman Spectra of the System AsH_3 – DF

For a complete vibrational analysis, the mixture AsH_3 - DF was investigated in an argon matrix. In these experiments an isotopic exchange was detected. The spectra of these experiments are shown in FIG. 6.

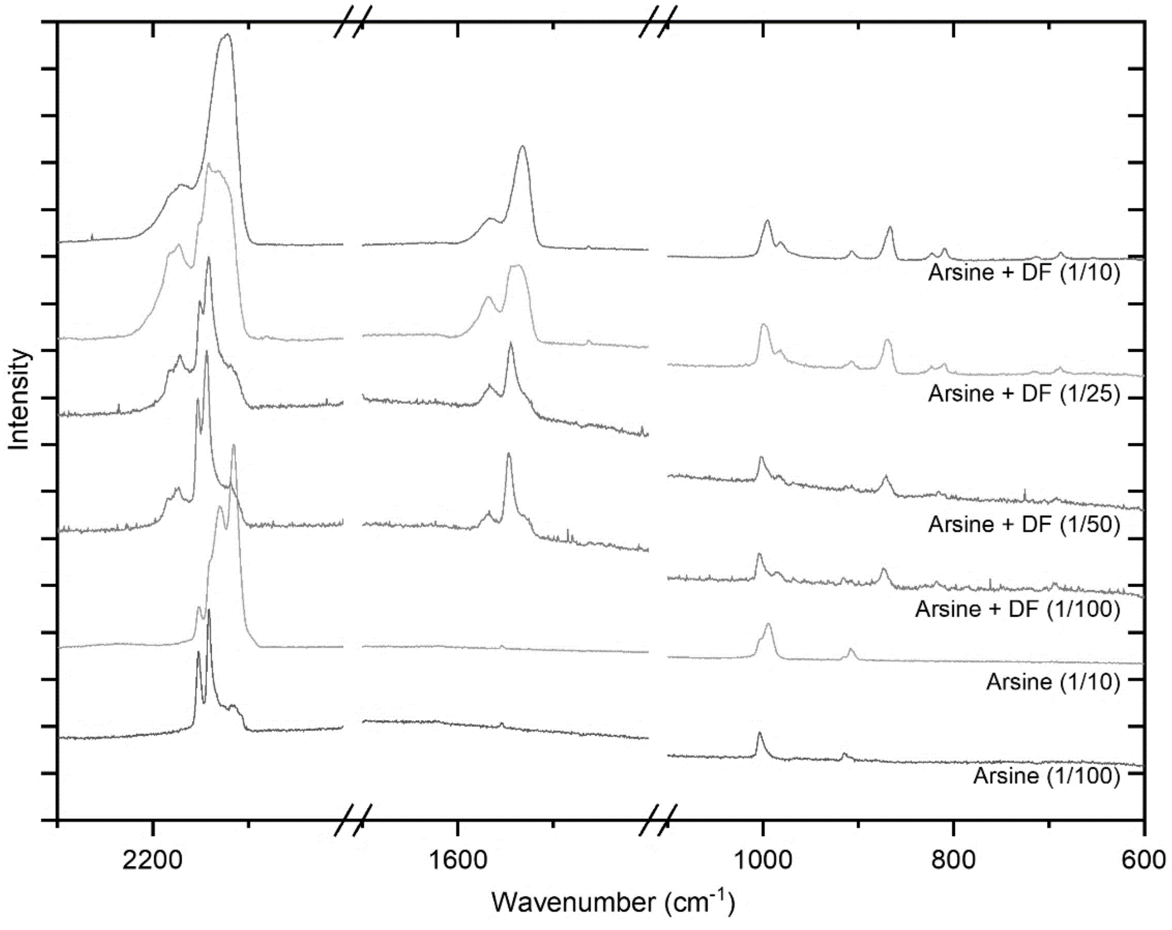

FIG. 6: Raman matrix spectra of AsH_3 co-condensed with DF in argon at 10 K (experimental conditions: 100 μm layer, laser wavelength 532 nm, laser power 1000 mW, Raman intensity is normalized)

All Raman lines, which have been identified as As-H vibrational modes of AsH_3, AsH_2^+ and AsH_2F by the experiments discussed in 2.2.3.4 are observable. Therefore, the matrices must contain a mixture of the deuterium and the corresponding hydrogen substituted arsenic species. This is achieved by either an incomplete H-D exchange or the decomposition mechanism mentioned in the theoretical part 2.2.3.1 of this study. The ν (As-D) of AH_2D, which may result from a H/D exchange at arsine in the reservoir vessel, is observed at 1545 cm^{-1}, whilst the ν (As-D) of $AsHD^+$ is detected at 1569 cm^{-1} (FIG. 6). The experimental shift is in good agreement with the H/D isotopic effect [8] and the quantum chemical calculations, which predict a Raman line at 1542 cm^{-1} for the As-D valence mode. The As-H stretching mode of $AsHD^+$ is observed at 2179 cm^{-1} and it is located between the two As-H stretching modes of AsH_2^+. The δ (H-As-H) and δ (H-As-D) of AsH_2^+ and $AsHD^+$ are observed as shoulders of the δ_s (H-As-H) of AsH_3 and AsH_2D at 1004 cm^{-1} and 873 cm^{-1} respectively.

At a S/M ratio of 1/25 or higher, the ν_s (As-D) of AsHDF is observed at 1534 cm^{-1}. This is in satisfying agreement with the H/D isotopic effect. [8] The ν (As-H) of AsHDF superimposes with the As-H valence modes of AsH_3 and AsH_2F at approximately 2119 cm^{-1}. This value is in reasonable agreement with *Lester Andrews*, who observed this mode at 2113 cm^{-1} as well as with the quantum chemically calculated value of 2145 cm^{-1}. [63] The deformation modes of AsHDF are observed at 867 cm^{-1} (H-As-D), 809 cm^{-1} (H-As-F) and 588 cm^{-1} (D-As-F). The most meaningful vibrational mode in order to prove the existence of AsH_2F or AsHDF is the As-F stretching vibration, which is detected at 654 cm^{-1} as a weak Raman line at a dilution of 1/10 for the protonated and the deuterated molecule. The intensity decreases with the dilution of the matrix and the amount of formed AsH_2^+.

At a S/M ratio of 1/25 the amount of AsH_2F or AsHDF in the sample is enough to observe the H-As-F bending mode at 822 cm^{-1} and 809 cm^{-1}, respectively. (FIG. 6) The Raman line of the δ_{as} (H-As-H) of AsH_3, δ (H-As-H) of AsH_2^+ and δ_s (H-As-H) of AsH_2F, shifts from 1004 cm^{-1} at a S/M of 1/100 to 995 cm^{-1} at S/M of 1/10. The same effect is observed for the Raman lines of their deuterated counterparts, which shift from 873 cm^{-1} at S/M 1/100 to 867 cm^{-1} at a S/M of 1/10. The δ_{as} (H-As-D/H) of AsHDF and AsH_2F are assigned to the Raman lines at 588 cm^{-1} and 822 cm^{-1} respectively.

TABLE 6: Experimental and calculated vibrational frequencies of AsH_2F and AsHDF at 10 K. Vibrational frequencies were calculated at the CCSD/aug-cc-pvtz level of theory and are given in cm^{-1}. Raman intensities are calculated at the MP2/aug-cc-pvtz level of theory and are listed in Å^4/*u*.

	Vibrational Frequencies [cm^{-1}]					
Species	Experimental	Rel. Int.	Lit. [63]	Calc.[a]	Int. [˚A^4/u]	Assignment
AsH_2F	2116 (Xe) (± 3)	0.68	2117	2145	130	ν_{as} (AsH)
	2107 (Xe) (± 3)	1.00	2108	2129	271	ν_s (AsH)
	995 (± 3)	0.07	984	980	7	δ_s (AsH_2)
	822	0.05	842	814	10	δ_s (AsHF)
	809	0.05		782	9	δ_{as} (AsHF)
	645	0.01	649	654	8	ν (AsF)
AsHDF	2119 (Ar) (± 5)	1.00	2113	2178	199	ν (AsH)
	1535	0.73	1522	1522	103	ν (AsD)
	867	0.23		851	5	δ (AsHD)
	809	0.07		799	9	δ (AsHF)
	654	0.01	654	657	7	ν (AsF)
	588	0.02		577	5	δ (AsDF)
AsH_2^+	2184	0.75		2176	91	νas (AsH)
	2173	1.00		2156	213	νs (AsH)
	998	shoulder		981	9	δ (AsH_2)
$AsHD^+$	2179	1.00		2165	150	ν (AsH)
	1569	0.48		1542	78	ν (AsD)
	873	shoulder		852	7	δ (AsHD)

[a] scaled with an empirical factor of 0.95

In summary, the H/D isotopic exchange experiments support the hypothesis, that AsH_2^+ and AsH_2F are formed by the co-condensation of the system AsH_3 and HF in noble gases. If the AsH_2 species are formed *via* a protonation or deuteration of AsH_3 and a subsequent condensation step, as sketched in FIG. 4, either H_2 or HD can be eliminated. As a result of this elimination, a mixture of AsH_2^+, $AsHD^+$, AsH_2F and AsHDF must be observed in the experiments. (FIG. 7) All these species have been identified during the Raman measurements. Taking these vibrational observations into consideration, the formation of the AsH_2 species must take place *via* the protonation of arsine and a subsequent partly decomposition of AsH_4^+ or AsH_4F.

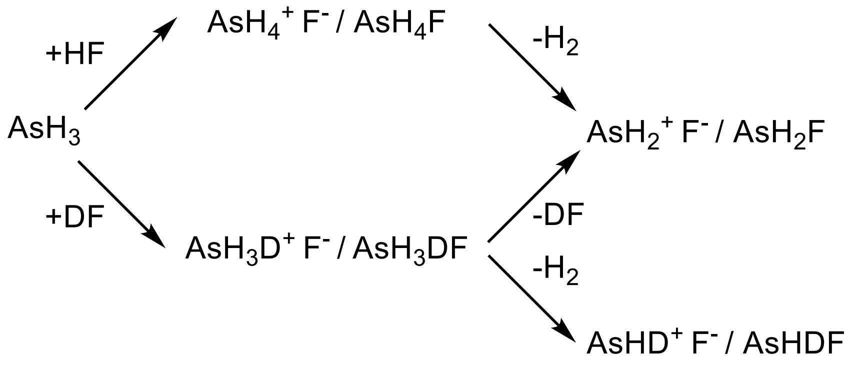

FIG. 7: Possible reaction pathway leading to the formation of AsH_2^+, $AsHD^+$, AsH_2F and AsHDF.

2.2.3.6 Raman Spectra of the System AsH_3 − HBr

The experiments of AsH_3 with hydrogen fluoride had shown that no tetrahedral arsonium species was formed. In order to investigate, weather the tetrahedral arsonium species can be observed under different conditions, the co-condensation of arsine and hydrogen bromide, which is known to form the AsH_4^+ Br^- species as a pure solid, was studied. [40] If arsine in argon and HBr in argon are separately condensed on the cold tip at a S/M of 1/500, two additional blue-shifted As-H valence modes are detected at wavenumbers higher than 2300 cm^{-1}. (FIG. 8) These modes are assigned to the AsH_4^+ cation. The antisymmetric As-H valence mode is observed at 2378 cm^{-1} and the symmetric As-H valence mode at 2367 cm^{-1}. Unscaled calculations at the CCSD/aug-cc-pvtz level of theory predict the antisymmetric As-H valence vibration at 2472 cm^{-1} and the symmetric As-H stretching mode at 2422 cm^{-1}. The symmetric H-As-H deformation mode of AsH_4^+ is coincident with the antisymmetric H-As-H bending mode of AsH_3.

To examine, if a bromo arsorane might be present AsH_4Br and its vibrational data have been calculated. The arsorane is supposed to exhibit a third As-H valence mode at 2081 cm^{-1} due to its reduced C_{3v} symmetry, which is not detected and therefore, it can be excluded. The experimental and calculated data is summarized in TABLE 7.

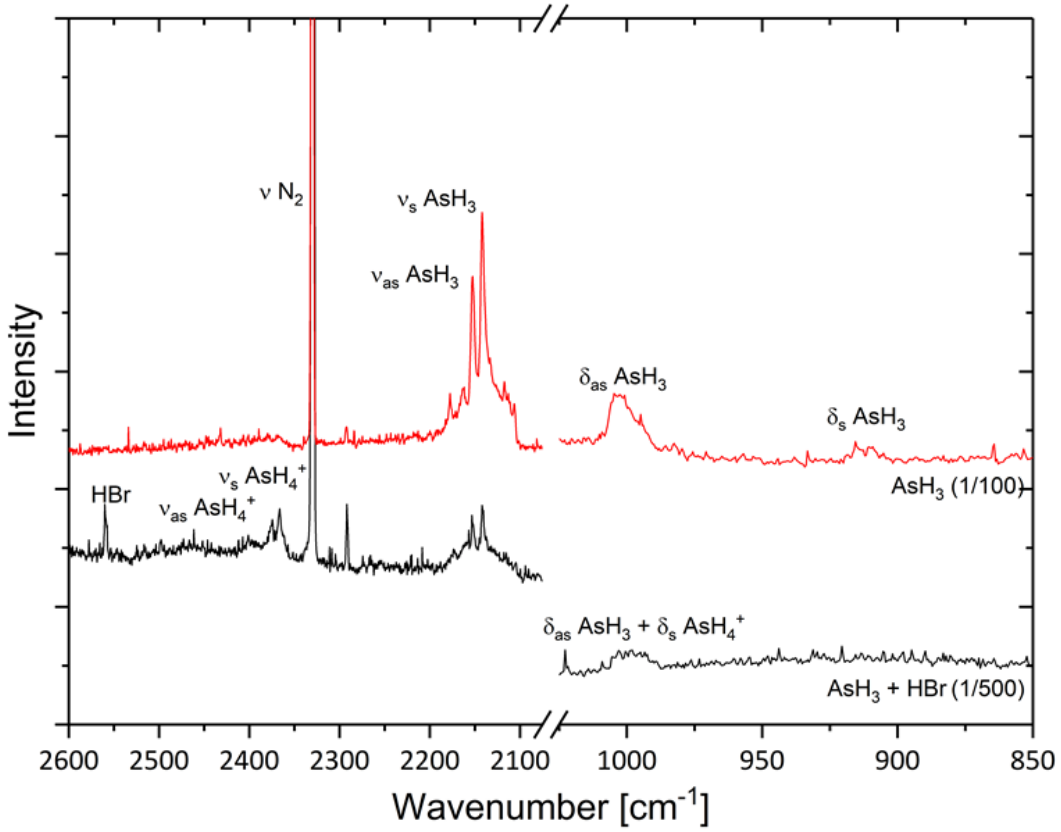

FIG. 8: Raman spectrum of the co-condensation experiment of AsH_3 and HBr on to the cold tip in an argon matrix at a S/M of 1/500 and the spectrum of arsine (1/100). (experimental conditions: 100 μm layer, laser wavelength 532 nm, laser power 1000 mW, Raman intensity is normalized)

TABLE 7: Comparison of experimental and calculated frequencies of AsH_4^+ and AsH_4Br. Vibrational frequencies were calculated at the CCSD/aug-cc-pvtz level of theory and are given in cm^{-1}. Raman intensities are calculated at the MP2/aug-cc-pvtz level of theory and are listed in $Å^4/u$.

	Vibrational Frequencies [cm^{-1}]					
Species	Experimental	Rel. Int.	Calc.	Calc. [a]	Int. [˚A^4/u]	Assignment
AsH_4^+	2398	0.20	2472	2348	150	ν_{as} (AsH)
	2371	0.50	2422	2301	310	ν_s (AsH)
	1001	0.01	1048	996	30	δ_s (AsH)
	-	-	899	854	6	δ_{as} (AsH)
AsH_4Br	-	-	2466	2343	89	ν_{as} (AsH)
	-	-	2402	2282	297	ν_s (AsH)
	-	-	2191	2081	480	ν (AsH)
	-	-	1104	1049	40	δ (AsH)
	-	-	853	810	10	δ_{as} (AsH)
	-	-	840	798	40	δ_s (AsH)
	-	-	470	447	4	δ (AsH)
	-	-	165	157	3	ν (AsF)

[a] scaled with an empirical factor of 0.95

2.2.4 CONCLUSION

AsH_3 and HF have been co-condensed in argon and xenon matrices in order to study their reaction behavior. The formation of AsH_2^+ and AsH_2F was observed by Raman spectroscopy and is confirmed by isotopomeric exchange experiments. The corresponding tetrahedral AsH_4^+ cation was not observed. Matrix isolation experiments of the system $AsH_3 - HBr$ prove that the generation of AsH_4^+ is possible with heavier hydrogen halides. The experimental vibrational data are discussed together with calculations at the CCSD/aug-cc-pvtz level of theory, which predict a C_{2v} structure for AsH_2^+ and a C_s structure for AsH_2F.

Supporting Information on the Experiments of the System AsH_3 − H*X* (*X* = F, Br) (Chapter 2.2)

The vibrational data of co-condensation experiments of premixed AsH_3 and HF experiments is summarized in TABLE S 1. The corresponding Raman spectra are depicted in FIG. 5.

TABLE S 1: Experimental and calculated vibrational frequencies of AsH_3, or AsH_3 and HF in argon at 10 K. Vibrational frequencies were calculated at the CCSD/aug-cc-pvtz level of theory and are given in cm^{-1}. Raman intensities are calculated at the MP2/aug-cc-pvtz level of theory and are listed in $Å^4/u$.

Arsine		Arsine + HF						Calculated			
1/100	1/10	1/100	Int.	1/50	Int.	1/10	Int.	Scaled[a]	Int.	Species	Assignment
-	-	2184	0.79	2182	0.81	2184	0.35	2276	91	AsH_2^+	ν_{as} (AsH)
-	-	2173	0.81	2171	0.83	2167	0.42	2156	213	AsH_2^+	ν_s (AsH)
2152	-	2154	0.98	2152	0.89	-	-	2171	120	AsH_3	ν_{as} (AsH)
2142	-	2143	1.00	2141	1.00	2143	0.66	2146	331	AsH_3	ν_s (AsH)/
						2119	0.90	2145	130	AsH_2F	ν_{as} (AsH)
-	2130	-	-	-	-	2130	0.83	2171	120	AsH_3	ν_{as} (AsH)
-	-	-	-	-	-	-	-	2128	271	AsH_2F	ν_s (AsH)
	2116	2116	0.27	2116	0.43	2116	1.00	2146	331	AsH_3	ν_s (AsH)
-	-	1547*	0.71	1547a	0.70	1535a	0.25	1540	103	AsHDF	ν (AsD)
1003	994	1003	0.21	1003	0.22	996	0.35	990	8	AsH_3	δ_{as} (AsH)/
								981	9	AsH_2^+	δ (AsH)
915	908	915	0.10	909	0.12	906	0.18	892	2	AsH_3	δ_s (AsH)
-	-	874	0.06	870	0.06	866	0.10	841	9	AsHDF	δ (AsHD)

*artifacts of previous experiments with DF.

[a] scaled with an empirical factor of 0.95

The vibrational data of the co-condensation experiments of premixed AsH_3 and DF in an argon matrix is summarized in TABLE S 2. The corresponding Raman spectra are depicted in FIG. 6.

TABLE S 2: Experimental and calculated vibrational frequencies of AsH_3, or AsH_3 and DF in argon at 10 K. Vibrational frequencies were calculated at the CCSD/aug-cc-pvtz level of theory and are given in cm^{-1}. Raman intensities are calculated at the MP2/aug-cc-pvtz level of theory and are listed in Å^4/*u*.

			Arsine + DF					Calculated			
1/100	Int.	1/50	Int.	1/25	Int.	1/10	Int.	Scaled[a]	Int.	Species	Assignment
2184	0.32	2182	0.41	2182	0.58	2178	0.22	2176	91	AsH_2^+	ν_{as} (AsH)
2179	0.30	2178	0.37	2178	0.55	-	-	2165	150	$AsHD^+$	ν (AsH)
2173	0.35	2173	0.47	2173	0.61	2171	0.30	2156	213	AsH_2^+	ν_s (AsH)
2152	0.88	2151	0.85	2150	0.72	-	-	2171	120	AsH_3/	ν_{as} (AsH)
								2171	120	AsH_2D	ν_{as} (AsH)
2147	0.50	2145	0.57	-	-	-	-	2155	257	AsH_2D	ν_s (AsH)
2143	1.00	2142	1.00	2115	1.00	2115	0.67	2146	331	AsH_3/	ν_s (AsH)/
				2124	0.90	2124	0.96	2145	130	AsH_2F	ν_{as} (AsH)
-	-	-	-	2130	0.93	2130	0.93	2171	120	AsH_3	ν_{as} (AsH)
-	-	-	-	2111	sh	2111	sh	2129	271	AsH_2F	ν_{as} (AsH)
2119	0.40	2118	0.33	2118	0.82	2118	1.00	2146	331	AsH_3	ν_s (AsH)
1569	0.25	1567	0.22	1567	0.39	1566	0.24	1542	78	$AsHD^+$	ν (AsD)
1547	0.56	1545	0.54	1543	0.48	-	-	1540	100	AsH_2D	ν (AsD)
-	-	-	-	1535	0.47	1532	0.42	1522	103	AsHDF	ν_{as} (AsD)
1004	0.35	1001	0.31	999	0.36	995	0.25	990	8	AsH_3/	δ_{as} (AsH_2)
								981	9	AsH_2^+/	δ (AsH_2)
								980	7	AsH_2F	δ_s (AsH_2)
985	0.11	985	0.17	983	0.19	981	0.20	969	7	AsH_2D	δ_s (AsH_2)
915	0.10	914	0.09	907	0.13	906	0.09	892	2	AsH_3	δ_s (AsH_3)
873	0.28	871	0.24	868	0.23	867	0.24	855	6	AsH_2D/	δ_s (AsHD)/
								852	7	$AsHD^+$/	δ (AsHD)
								851	5	AsHDF/	δ_s (AsHD)/
-	-	-	-	823	0.12	822	0.08	814	10	AsH_2F	δ_s (AsHF)
809	0.12	809	0.08	809	0.14	809	0.10	799	9	AsHDF/	δ_{as} (AsHF)/
								794	2	AsH_2D	δ_s (AsH_2D)
								782	9	AsH_2F	δ_{as} (AsHF)
693	0.09	691	0.10	689	0.09	687	0.07			?	?
						654	0.01	657	7	AsHDF/	ν (AsF)
								654	8	AsH2F	ν (AsF)
589	0.25	588	0.12	588	0.11	588	0.08	577	5	AsHDF	δ_{as} (AsHD)
357	0.24	-		356	0.06	358	0.03	-	-	As4	ν_s (As-As)
255	0.29	256	0.24	252	0.10	254	0.05	-	-	As4	ν_{as} (As-As)

[a] scaled with an empirical factor of 0.95

The vibrational data of the experiments of premixed AsH_3 and HF in a xenon matrix is summarized in TABLE S 3 and the spectra are depicted in FIG S. 1.

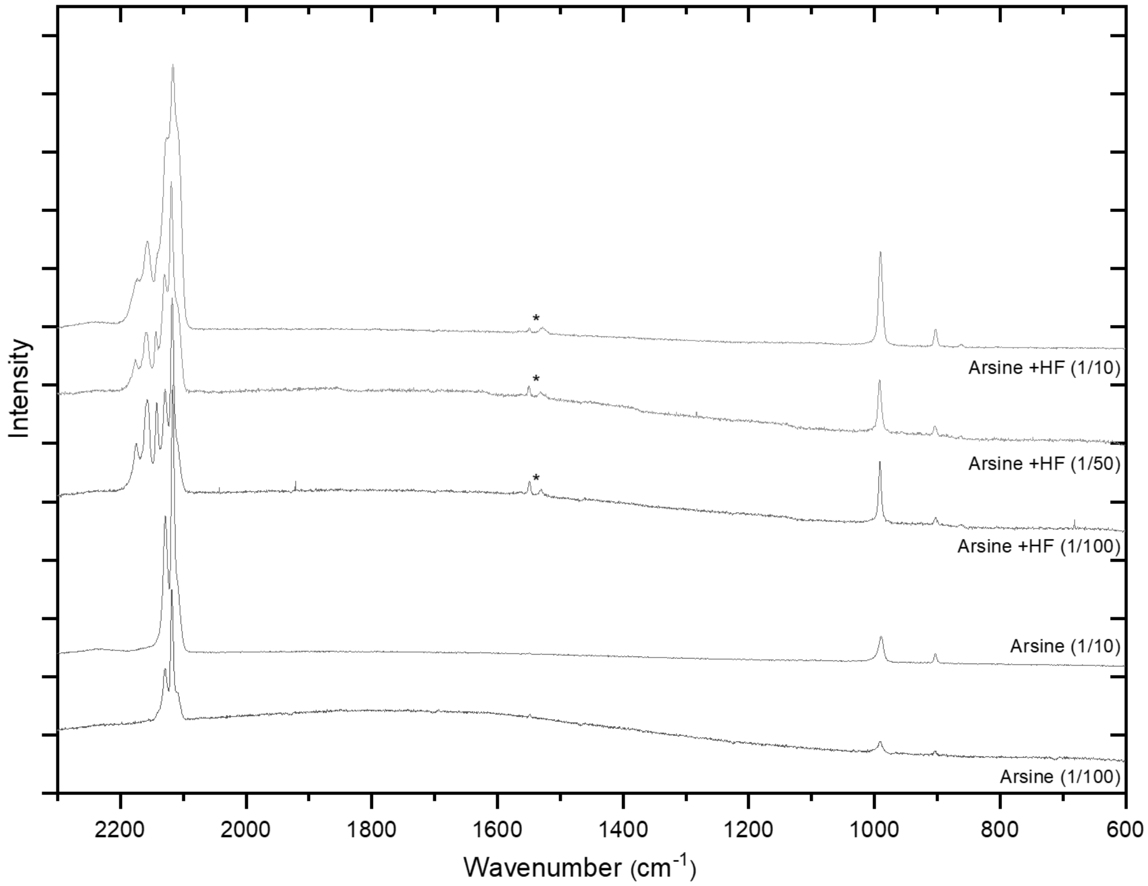

FIG S. 1: Raman matrix spectra of AsH_3 co-condensed with HF in xenon at 10 K (experimental conditions: 100 μm layer, laser wavelength 532 nm, laser power 1000 mW, Raman intensity is normalized) *marks deuterated residues from former experiment.

TABLE S 3: Experimental and calculated vibrational frequencies of AsH_3, or AsH_3 and HF in xenon at 10 K. Vibrational frequencies were calculated at the CCSD/aug-cc-pvtz level of theory and are given in cm^{-1}. Raman intensities are calculated at the MP2/aug-cc-pvtz level of theory and are listed in $Å^4/u$.

Arsine		Arsine		+		HF		Calculated			
1/100	1/10	1/100	Int.	1/50	Int.	1/10	Int.	Scaled[a]	Int.	Species	Assignment
-	-	2174	0,26	2176	0,15	2174	0,17	2176	91	AsH_2^+	ν_{as} (AsH)
-	-	2158	0,48	2159	0,28	2157	0,32	2156	213	AsH_2^+	ν_s (AsH)
-	-	2142a	0,46	2143a	0,28	2143a	0,24	2137	199	AsHDF	ν (AsH)
-	-	-	-	-	-	2116	0,71	2145	130	AsH_2F	ν_{as} (AsH)
2129	2129	2129	0,52	2130	0,56	2127	0,72	2171	120	AsH_3	ν_{as} (AsH)
-	-	-	-	-	-	2107	0,76	2129	271	AsH_2F	ν_s (AsH)
2118	2117	2117	1,00	2119	1,00	2117	1,00	2146	331	AsH_3	ν_s (AsH)
-	-	1531a	0,02	1531a	0,02	1530a	0,02	1522	103	AsHDF	ν (AsD)
990	989	991	0,32	992	0,24	991	0,37	990	8	AsH_3/	δ_{as} (AsH_2)/
								981	9	AsH_2^+	δ (AsH_2)
903	903	903	0,03	903	0,03	903	0,07	892	2	AsH_3	δ_s (AsH_2)
-	-	862*	0,01	862*	0,01	862*	0,01	841	9	AsHDF	δ_{as} (AsHD)

*artifacts of previous experiments with DF.

[a] scaled with an empirical factor of 0.95

The vibrational data of AsH_3, AsH_2^+ and AsH_2F was calculated based on different methods. The results are listed in TABLE S 4.

TABLE S 4: Calculated vibrational frequencies of AsH_3, AsH_2^+ and AsH_2F at different levels of theory in cm^{-1}.

	HF/ aug-cc-pvtz	B3LYP/ aug-cc-pvtz	MP2/ aug-cc-pvtz	QCISD/ aug-cc-pvtz	CCSD/ aug-cc-pvtz	Assignment
AsH_3	2330	2195	2285	2283	2285	ν_{as} (AsH)
	2328	2181	2259	2256	2259	ν_s (AsH)
	1106	1016	1042	1041	1042	δ_{as} (AsH_3)
	1002	932	939	939	939	δ_s (AsH_3)
AsH_2^+	2363	2211	2309	2290	2290	ν_{as} (AsH)
	2356	2200	2285	2269	2269	ν_s (AsH)
	1105	1012	1052	1033	1033	δ (AsH_2)
AsH_2F	2315	2145	2275	2257	2258	ν_{as} (AsH)
	2314	2131	2252	2239	2241	ν_s (AsH)
	1097	1003	1043	1031	1032	δ_s (AsH_2)
	916	820	869	855	857	δ_s (AsHF)
	867	784	838	820	823	δ_{as} (AsHF)
	724	644	691	683	688	ν (AsF)

The apparatus, which was used for the co-condensation experiments is depicted in FIG S. 2 as a schematic drawing and as a photography in FIG S. 3.

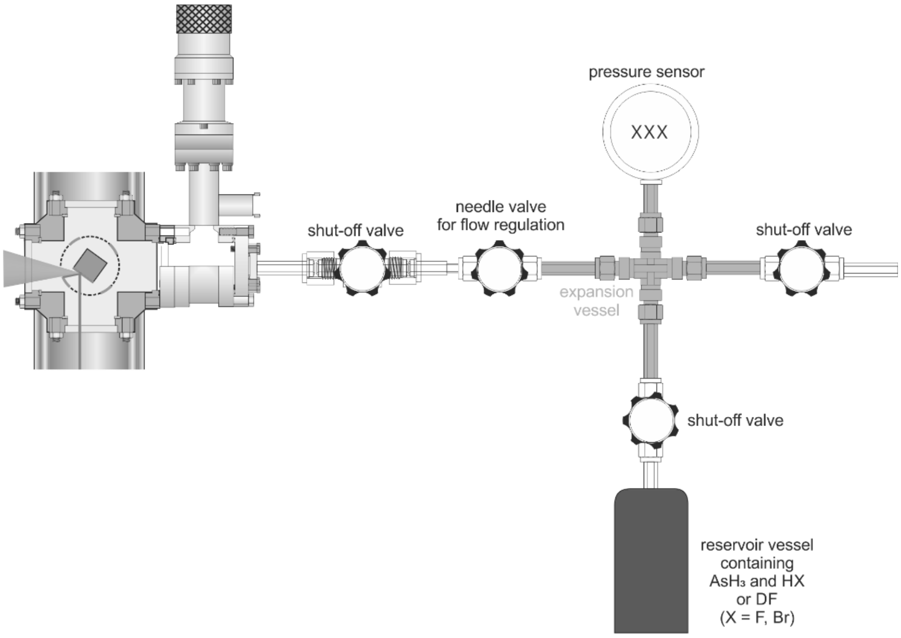

FIG S. 2: Schematic drawing of the apparatus for the deposition of AsH_2^+ and AsH_2F.

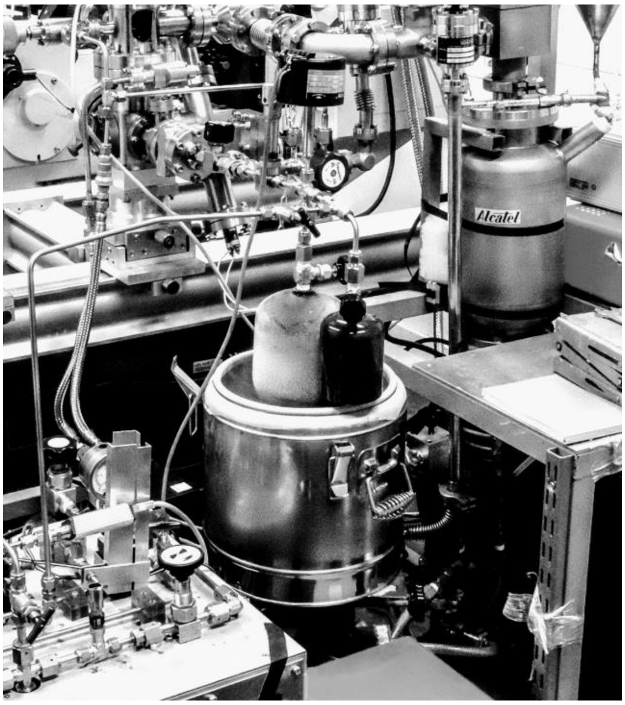

FIG S. 3. Photography of the apparatus for the deposition of AsH_2^+ and AsH_2F.

2.3 Raman Matrix Isolation Study on the System PH_3 – HX

2.3.1 INTRODUCTION

Earth's shell, atmosphere, hydrosphere, biosphere and lithosphere consist to 0.07 % by weight of phosphorus, which is mostly present in the form of compounds having coordination numbers of one to six. [71] The knowledge about the existence of different phosphorus species in space is strongly limited. [71, 72] Already in 1974, evidence for the existence of PH_3 in the Jupiter atmosphere by means of infrared spectroscopy has been provided. [73, 74] Three years later, the proof for the same compound followed in the atmosphere of Saturn. [74-76] Presumably, PH_3 is formed in the hot depths of the atmosphere of these planets and subsequently transported to higher altitudes by atmospheric turbulences.

FIG. 9: Picture of Jupiter. Taken on 10 July 2017 at 19:12 o'clock by the Juno spacecraft during its seventh close flyby. The turbulent Great Red Spot fades from Juno's perspective as the dynamic bands of the southern Jupiter region move into focus. North is on the left side of the picture, south on the right. [77]

In 1975, *Prinn* and *Lewis* proposed, based on a theoretical study, that the reddish coloration of the atmosphere and the "Great Red Spot", a giant oval anticyclone on the surface of Jupiter, could be traced back to the photolysis of PH_3 to red phosphorus. A reaction sequence was proposed including a disproportionation of the previously formed PH_2. [78, 79]

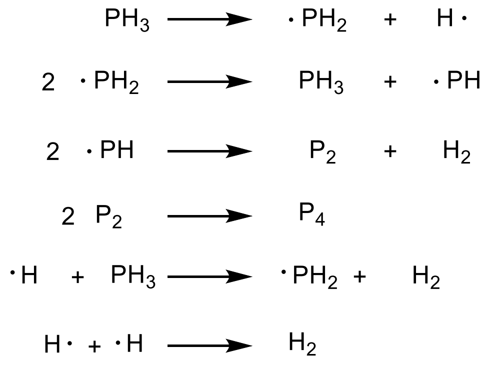

FIG. 10: Photolysis of PH_3 to P_4. [78, 79]

Another popular theory for the origin of the "Great Red Spot" was proposed by *Hudson* and *Loeffler,* which explains the color with NH_4SH and acetylene. Here, the reaction of the two compounds is supposed to form a reddish thiolin compound. [80] *Ferris* and *Benson* were able to show that P_2H_4 is formed as a photo product by simulating the conditions on Jupiter in the laboratory and thus describing an alternative mechanism that proposes the formation of P_2H_4 from PH_2. [81, 82]

Experiments that simulate the conditions present on Saturn and Jupiter in combination with quantum mechanical simulations contribute to the general understanding of the atmosphere on distant planets. In addition to phosphine, hydrogen halides were also detected on Saturn and Jupiter in concentrations comparable to PH_3. [32, 33] An investigation of the possible reaction between the two molecules under corresponding conditions has not yet been

$$PH_3 \longrightarrow \cdot PH_2 + H\cdot$$
$$2\ \cdot PH_2 \longrightarrow PH_3 + \cdot PH$$
$$2\ \cdot PH \longrightarrow P_2 + H_2$$
$$2\ P_2 \longrightarrow P_4$$
$$\cdot H + PH_3 \longrightarrow \cdot PH_2 + H_2$$
$$H\cdot + \cdot H \longrightarrow H_2$$

studied. This prompted us to investigate the behavior of the system $PH_3 - HF$ and $PH_3 - HBr$ under matrix isolation conditions. These experiments can give an insight whether the PH_4^+ species or related phosphorus hydrogen species could form in Jupiter's and Saturn's atmosphere.

2.3.2 RESULTS AND DISCUSSION

2.3.2.1 Theoretical Considerations

For the analysis of the experimental results several reaction products must be taken into account. The first one is the tetrahedral phosphonium cation, which could be generated by the protonation of phosphine by hydrogen halides. The formation of a covalent phosphonium fluoride has also been considered. Irrespective of the formed species between PH_3 and HF, a hydrogen elimination of the phosphonium species could lead to PH_2F or PH_2^+ in a subsequent reaction step. PH_2F has been observed by *Lester Andreas via* fluorination of phosphine in an argon matrix and by *Helmut Beckers via* the gas phase reaction of H_3PF_2 with hydrides by IR spectroscopy. [83-85]

The possible formation of PH_2^+ or PH_2F from PH_4^+ or PH_4F is assumed to take place by a hydrogen elimination. For a better understanding of the elimination, the decomposition pathway of PH_4^+ and PH_4F was calculated in order to investigate if the elimination is more likely to take place from PH_4^+ or PH_4F. The optimizations and the energy calculations of the stationary points were conducted under employment of the MP2/aug-cc-pvtz level of theory. The vibrational analysis of the stationary points on the potential energy surface exhibits a single negative frequency and therefore marks the transition state as anticipated. PH_4^+ exhibits tetrahedral symmetry and therefore all hydrogen atoms are indistinguishable. As a result, it is irrelevant which hydrogen atoms are approaching each other during the elimination process, forming the phosphine-like transition state. However, the reaction is endothermic by 221 kJ/mol and the activation barrier of 229 kJ/mol is relatively high. (FIG. 11)

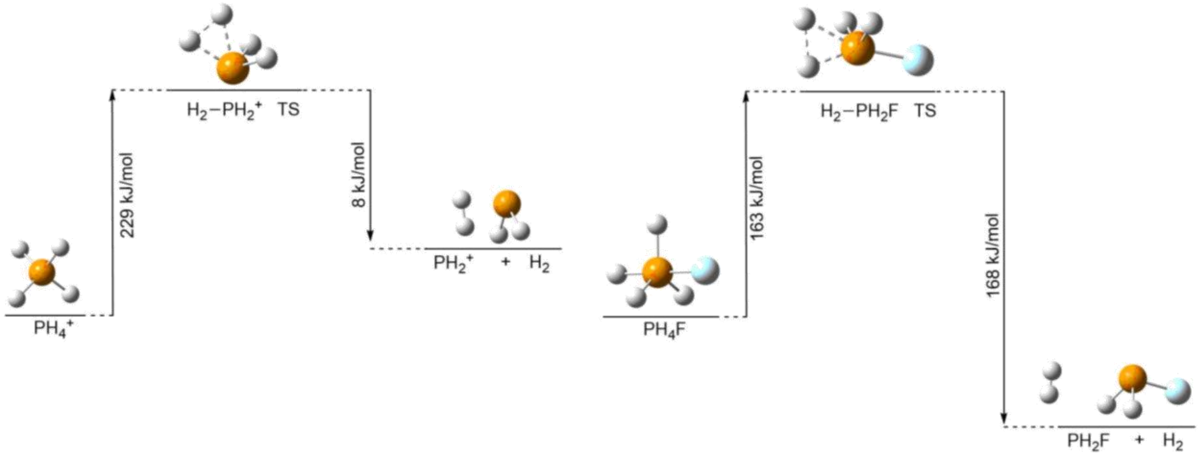

FIG. 11: Possible reaction pathways and transition states (TS) for the hydrogen elimination and the formation of PH_2^+ and PH_2F respectively.

The hydrogen elemination from PH_4F undergoes a different mechanism. Altogether, it is possible to either form hydrogen inside the H-P-H plane of the bipyramid or by approaching one hydrogen atom in the plane towards the hydrogen on the top of the pyramid. For the first option, the two atoms are separated by an angle of 120°, whilst for the second option the angle merely measures 90°. Therefore, a mechanism *via* the second possibility (top hydrogen towards plane hydrogen) is supposed. As expected, only one true transition state can be observed here. The quantum chemical calculations predict PH_2F and H_2 to be 5 kJ/mol more stable than PH_4F. The activation barrier of the reaction is 163 kJ/mol. On the bottom line, in this study the vibrational frequencies of the following species are considered: PH_3, PH_4F, PH_4^+, PH_2F and PH_2^+. The formation of PH_2^+ or PH_2F is discussed in Chapter 2.5.3.4 in detail.

2.3.2.2 Calculated Vibrational Frequencies

The vibrational frequencies of the considered phosphor hydrogen species are summarized in TABLE 8 and TABLE 9. The quantum chemical calculation at the CCSD/aug-cc-pvtz level of theory predicts the P-H stretching vibrations of phosphine at 2365 cm^{-1} and 2352 cm^{-1}. Compared to the experimental values of 2328 cm^{-1} and 2323 cm^{-1}, measured by gas phase IR spectroscopy, they are slightly blue-shifted but still in reasonable agreement. [64] The antisymmetric and symmetric H-P-H bending vibrations are predicted at 1103 cm^{-1} and 963 cm^{-1} respectively. The calculations underestimate the H-P-H bending modes by 14 cm^{-1} and 29 cm^{-1} respectively, compared to the experimental values of 1118 cm^{-1} and 992 cm^{-1}. [64] The overestimation of the H-P stretching modes and underestimation of the H-P-H bending modes is observed for all discussed phosphonium hydrogen species discussed later.

According to the vibrational analysis of the global minimum of PH_4^+, the P-H stretching modes are calculated at 2501 cm^{-1} and 2447 cm^{-1}. The P-H valence modes of $PH_4^+SbF_6^-$, reported by *Minkwitz* in 1992, are observed at 2528 cm^{-1} and 2473 cm^{-1}. [86] Here, the calculated and experimental values of the stretching modes are also in good agreement. In summary, the chosen quantum chemical model reflects the experimental values and therefore it is suitable for subsequent simulations of unreported species.

The calculations predict the ν_{as} (P-H) and the ν_{s} (P-H) of PH_2^+ at 2363 cm^{-1} at 2350 cm^{-1} respectively. The P-H stretching modes of PH_2^+ are expected between the P-H stretching modes of phosphine and the P-H stretching modes of PH_4^+. TABLE 8 summarizes the calculated vibrations of the deuterated analogs.

TABLE 8: Summarized calculated and literature-known vibrational data of PH_3, PH_4^+ and PH_2^+. Vibrational frequencies calculated on the CCSD/aug-cc-pvtz level of theory.

	Vibrational Frequencies [cm^{-1}]				
Assignment	PH_3		PH_4^+		PH_2^+
	calc.	Lit. (gas) [87]	calc.	Lit. (SbF_6^-)	calc.
ν_{as} (PH)	2365	2328	2501	2528[a]	2363
ν_s (PH)	2352	2323	2447	2473[a]	2350
δ_{as} (PH_2)	1104	1118	1108	1128[a]	
δ_s (PH_2)	963	992	967	991[a]	1102

[a] SbF_6^- salt described by *Minkwitz* in 1992 [86]

TABLE 9: Summarized calculated data of PH_2D, PH_3D^+ and PHD^+. Vibrational frequencies calculated on the CCSD/aug-cc-pvtz level of theory.

	Vibrational Frequencies [cm^{-1}]			
Assignment	PH_2D	Assignment	PH_3D^+	PHD^+
	calc.		calc.	calc.
ν_{as} (PH)	2358	ν_{as} (PH)	2460	2349
ν_s (PH)	2350	ν_s (PH)	2424	
ν (PD)	1690	ν (PD)	1758	1687
δ_s (PH_2)	1076	δ_{as} (PH_2)	1051	
δ_{as} (PH_2D)	952	δ_s (PH_2)	955	
δ_s (PH_2D)	863	δ (PHD)	830	958

The calculated vibrational modes of PH_4F and PH_2F are summarized in TABLE 10. Due to the C_{3v} structure of the fluoro phosphorane, three P-H valence modes are expected, which are all Raman active. The P-H valence modes in the bipyramidal plane are predicted at higher wavenumbers as the axial P-H stretching mode. The P-F vibration is anticipated at 602 cm^{-1}.

The P-H valence modes of PH_2F are expected slightly red-shifted compared to these of PH_2^+ at 2404 cm^{-1} and 2399 cm^{-1} respectively. Compared to the experimental vibrational frequencies of *Bürger*, the chosen quantum chemical model overestimates the valence modes of PH_2F by about 100 cm^{-1}. [85] Nevertheless, the difference between the symmetric and antisymmetric P-H bending modes is distinct. The ν (P-F) is predicted at 822 cm^{-1}, but should be expected at lower wavenumbers. The calculated vibrational data of the deuterated isotopomers of the above discussed compounds is summarized in TABLE 10.

TABLE 10: Summarized calculated and literature-known vibrational data of PH_4F and PH_2F. Vibrational frequencies calculated on the CCSD/aug-cc-pvtz level of theory.

	PH_4F		PH_2F		
Assignment	calc.	Assignment	calc.	lit.	Assignment
ν_{as} (PH)	2573	ν_{as} (PH)	2404	2287[a]	ν (PH)
ν_s (PH)	2515	ν_s (PH)	2399	2283[a]	ν (PD)
ν (PH)	2277	δ_s (PH_2)	1146		δ (PHD)
δ (PH)	1388	δ_s (PHF)	984		δ (PHF)
δ_{as} (PH)	1179	δ_{as} (PHF)	935		ν (PF)
δ_s (PH)	989	ν (PF)	822		δ (PDF)
δ (PH)	616				
ν (PF)	602				

[a] IR-study conducted by *Bürger* in 1995. [85]

2.3.2.3 Raman Spectra of the System PH_3 – HBr

The Raman spectra of system PH_3 – HBr display different features, depending on the M/S ratio (FIG. 12). Co-condensation experiments of the pure reactants [PH_3 + HBr (solid)] result in spectra with very strong and broad lines at 2379 cm^{-1} and 2327 cm^{-1}, which are identified as the P-H stretching modes of $PH_4^+Br^-$. The values are consistent with Raman spectroscopy experiments reported in 1969. [88] The experimental and aforementioned vibrational frequencies are summarized in TABLE 11.

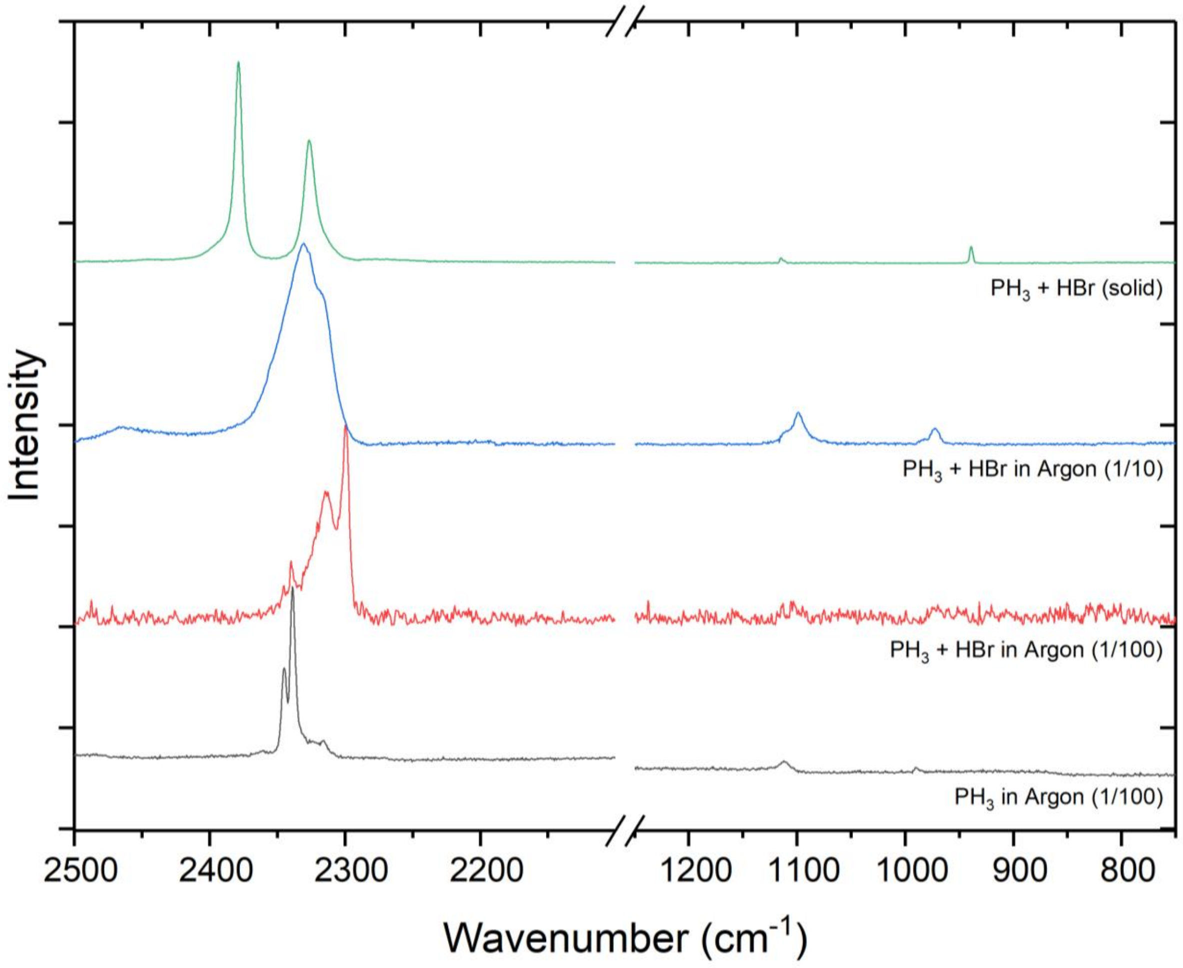

FIG. 12: Raman matrix spectra of PH_3 co-condensed with and without HBr in argon at 10 K (experimental conditions: 100 μm layer, laser wavelength 532 nm, laser power 1000mW, Raman intensity is normalized).

If the host material argon is mixed to the gas stream of the PH_3 – HBr mixture [PH_3 + HBr / argon (1/10)], the P-H valence modes of the PH species in FIG. 12 are shifted to lower wavenumbers. At an even higher dilution with argon (S/M 1/100) the superposition of the lines decreases and four well resolved vibrational modes are recorded at 2346 cm^{-1}, 2341 cm^{-1}, 2315 cm^{-1} and 2300 cm^{-1}. The two modes with the highest wavenumbers are assigned to the P-H stretching modes of phosphine, resulting from the direct co-condensation of phosphine in argon at the S/M ratio of 1/100. As discussed before by quantum chemical calculations in 2.3.2.2, the only P-H species in question showing red-shifted P-H valence modes in comparison to the valence modes of phosphine is PH_2^+. The P-H bending mode of PH_2^+ is than superimposed with the antisymmetric P-H bending mode of phosphine. The vibrational frequencies of all observed species are summarized in TABLE 12. In summary, the system PH_3 - HBr forms depending on the S/M ratio either: $PH_4^+Br^-$ or PH_2^+. The vibrational modes of the unreacted starting material PH_3 are detected in all matrix isolation experiments.

TABLE 11: Summary of the vibrational frequencies of $PH_4^+Br^-$.

Ra exp	PH_4^+ Br^- Lit.[a]	Assignment
2379	2379	ν_{as} (PH_4^+)
2327	2329	ν_s (PH_4^+)
1891	1891	2 x δ (PH_4^+)
1453	1444	δ (PH_4^+) + τ
1298	1287	δ (PH_4^+) + τ
1115	1114	δ (PH_4^+)
940	941	δ (PH_4^+)
351	343	T

[a] Raman-study conducted by *Rush* in 1969. [88]

TABLE 12: Summary of the vibrational frequencies of PH_3 and PH_2^+. Vibrational frequencies calculated on the CCSD/aug-cc-pvtz level of theory.

	PH_3		PH_2^+		
Ra exp	calc.	Lit.[a]	Ra exp.	calc	Assignment
2346	2365	2328	2315	2363	ν_{as} (PH)
2341	2352	2323	2300	2350	ν_{s} (PH)
1111	1104	1118	-	-	δ_{as} (PH_2)
990	963	992	1105	1102	δ_{s} (PH_2)

[a] several Raman studies [89-91]

2.3.2.4 Raman Spectra of the System PH_3 – AF (A=H, D)

Raman spectra of the system PH_3 – HF/DF in argon (S/M 1/100) are depicted in FIG. 13. A summary of the vibrational data is given in TABLE 13. The Raman spectra display none of the Raman lines observed in the PH_3 – HBr System. (2.3.2.3).

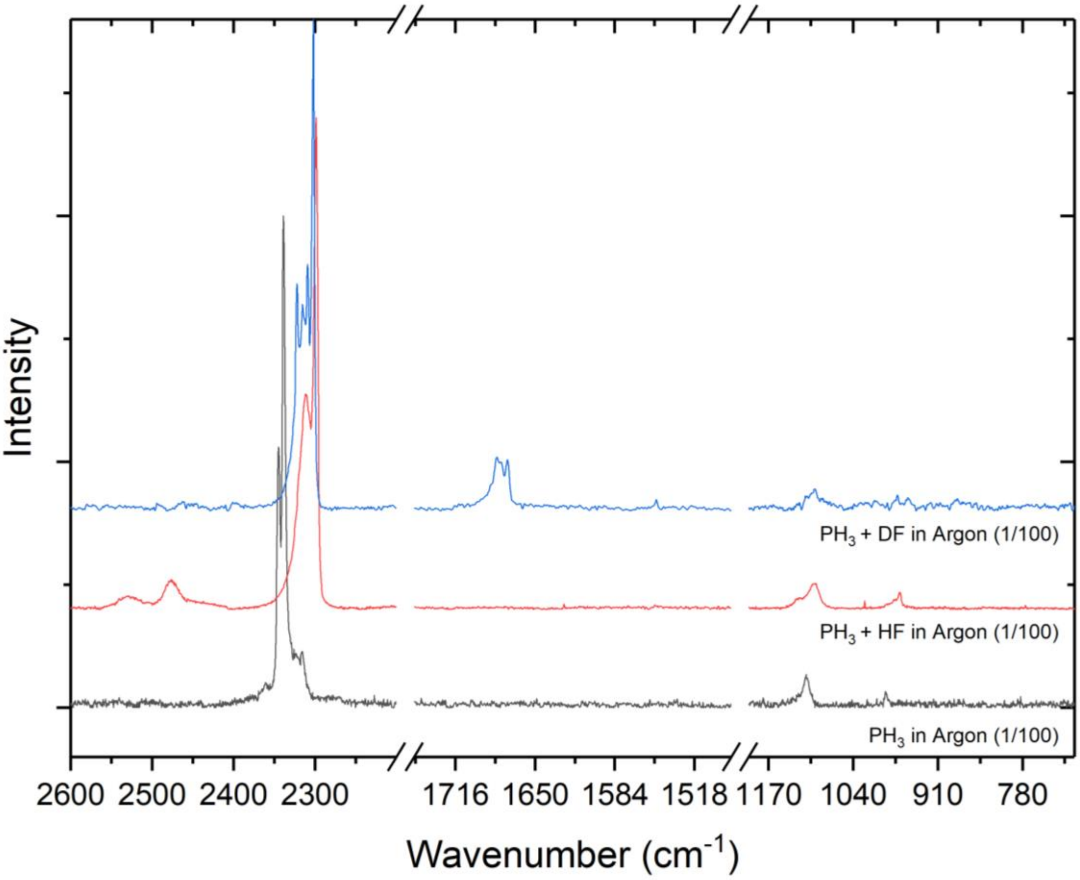

FIG. 13: Raman matrix spectra of PH3 co-condensed with and without HF and DF in argon at 10 K (experimental conditions: 100 µm layer, laser wavelength 532 nm, laser power 1000mW, Raman intensity is normalized).

The P-H valence modes of PH_2^+ (2315 cm^{-1} and 2300 cm^{-1}), which have been identified in the system PH_3 – HBr, are present in all Raman spectra, but are found to be slightly red-shifted. In the experiments with deuterium fluoride, two additional Raman lines at 2315 cm^{-1} and

2300 cm^{-1} are observed very close to Raman lines assigned to PH_2^+. Hence, at least one additional P-H species muss be present. Furthermore, two Raman lines at 1683 and 1673 cm^{-1} are observed. Wavenumbers in this region are typical for P-D stretching vibrations. Therefore, it must be presumed that two further H-P-D species are found. According to quantum chemical calculations (TABLE 9), the P-H stretching mode of PHD^+ is blue-shifted to the asymmetric valence mode of PH_2^+. Consequently, the Raman line at 2322 cm^{-1} is assigned to the P-H stretching mode of PHD^+ and the Raman line at 1673 cm^{-1} is allocated to the corresponding P-D valence mode. The remaining Raman lines at 2309 and 1673 cm^{-1} are assigned to the P-H and P-D valence modes of PHD, based on the relative differences of vibrational frequencies obtained by the calculations. One P-H stretching vibration of PH_2 was observed by *Abraham* in 1992 by Raman spectroscopy at high temperatures and deconvolution studies at 2310±2 cm^{-1}, which supports the present assignment. [89] In the Raman spectrum of the experiments of PH_3 and HF further Raman lines are detected at 2529, 2476 and 1122 cm^{-1}. These lines are assigned to the ν_{as} (P-H), ν_s (P-H) and δ_{as} (H-P-H) of the PH_4^+ moiety, respectively. The values are consistent with experiments reported by *Minkwitz* and *Kornath* in 1992. [86] In summary, the reaction of PH_3 with HF or DF yields PH_2^+, PH_4^+, PHD and PHD^+.

TABLE 13: Summary of the vibrational frequencies of the system PH_3 – HF/DF in argon. Vibrational frequencies calculated on the CCSD/aug-cc-pvtz level of theory.

PH_3			PH_2^+		PH_4^+			
Ra exp	calc.	Lit.[a]	exp.	calc	Ra exp.	Calc.	Lit. (SbF_6^-)	Assig.
2346	2365	2328	2315	2363	2529	2376	2528[b]	ν_{as} (PH)
2341	2352	2323	2300	2350	2476	2325	2473[b]	ν_s (PH)
1111	1104	1118	-	-	1122	1053	1128[b]	δ_{as} (PH_2)
990	963	992	1105	1102	-	919	991[b]	δ_s (PH_2)

[a] several Raman studies [89-91]

[b] SbF_6^- salt described by *Minkwitz* in 1992 [86]

TABLE 14: Summary of the vibrational frequencies of the system PH_3 – HF/DF in argon. Vibrational frequencies calculated on the CCSD/aug-cc-pvtz level of theory.

PHD^+		PHD			
Ra exp.	Calc.	Ra exp.	Calc	PH_2 Lit.	Assig.
2322	2349	2309	2338	2310±2 [a]	ν (PH)
1673	1687	1673	1679	-	ν (PD)
-	958	-	945	-	δ (PHD)

[a] *Abraham* in 1992 by Raman spectroscopy at high temperatures [89]

2.3.3 CONCLUSION ON THE SYSTEM PH_3 – HX (X = F, Br)

PH_3 and HBr have been co-condensed in order to study the reaction behaviour and the reaction products was identified as PH_4^+ Br^-. If PH_3 and HBr are condensed as a diluted noble gas mixture PH_3 and PH_2^+ are identified by Raman spectroscopy inside the so formed argon matrix. The Raman spectra of co-condensation experiments comprising a PH_3 and HF or PH_3 and DF mixture with argon show the formation of PH_2, PH_4^+ and PH_2^+ in the argon matrix.

2.4 Raman Matrix Isolation Study on the System SbH_3 – HF

2.4.1 INTRODUCTION

While the formation of NH_3 from its elements is exothermic by -46 kJ/mol, the standard enthalpy ($\mathit{\Delta_f H^0}$) of PH_3 is already +5 kJ/mol. This endothermic behavior increases with the weight of the pnictogen atom. The $\mathit{\Delta_r H^0}$ of SbH_3 is 145 kJ/mol. While PH_3 and AsH_3 are kinetically stable compounds, SbH_3 decomposes slowly at room temperature. [92] The proton affinity of the pentel hydrides decreases with the weight of the pentel from $\Delta_{acid}H_{298K}$ = 203.2 kJ/mol for NH_3 *via* 185.3 kJ/mol for PH_3 and 176.6 kJ/mol for AsH_3 to 175.4 kJ/mol for SbH_3 (calculated at BP86/QZ4P//BP86/TZ2P). [93]

In the experiments comprising the system AsH_3 – HF the formation of AsH_4^+, AsH_2^+ and AsH_2F was observed. In order to investigate weather analogous behavior can be observed the experiments involving the system SbH_3 – HF in argon were conducted.

2.4.2 RESULTS AND DISSCUSSION

2.4.2.1 Theoretical Considerations

For the analysis of the experimental results of the system SbH_3 – HF different reaction products must be considered. Most prominent is the possible observation of the tetrahedral stibinium ion, which may be generated by the protonation of stibine with hydrogen fluoride. The possible observation of a covalent bonded stibinium fluoride is less reasonable, but nevertheless it has been considered. Regardless which of these species is observed, a subsequent degradation step of the stibinium species into SbH_2F or SbH_2^+ in analogy to arsenic has been contemplated. While PH_2F and AsH_2F have already been detected, SbH_2F has not been observed yet. [63, 83-85]

SbH_2^+ and SbH_2F may be formed from SbH_4^+ or SbH_4F. In order to gain a better understanding of this elimination pathway, the decomposition was simulated. Here, the MP2/aug-cc-pvtz level of theory was employed for the optimizations and the energy calculations of the stationary points. The vibrational analysis of the stationary points with the highest energy on the potential energy surface exhibits a single negative frequency and therefore marks a transition state as anticipated. SbH_4^+ exhibits a tetrahedral symmetry and accordingly all hydrogen atoms are equivalent. As a result, it is irrelevant which hydrogen atoms are approaching each other during the elimination process in order to form the stibine-like transition state. However, the reaction is not favored energetically in this direction and the activation barrier of 219 kJ/mol is high. (FIG. 14) Thus, a reaction following this pathway is very unlikely.

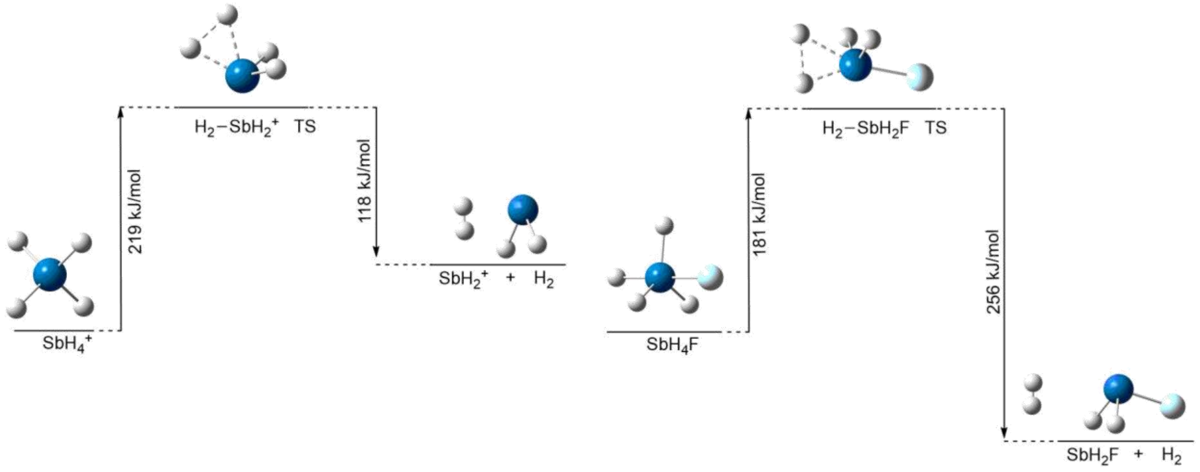

FIG. 14: Possible reaction pathways and transition states (TS) for the hydrogen elimination and the formation of SbH_2^+ and SbH_2F respectively.

The hydrogen elimination from SbH_4F is different from that of SbH_4^+. Altogether, it is possible to either form hydrogen inside the H-Sb-H plane of the bipyramid or by approaching one hydrogen atom in the plane towards the hydrogen on the top of the pyramid. For the first option, the angle separating the two atoms is 120°, whilst for the second one the angle only is 90°. Therefore, a mechanism *via* the axial hydrogen atom can be presumed. As expected, only one true transition state can be detected for the second option. According to the quantum chemical calculations, the reaction is exothermic by 75 kJ/mol in the gas phase. Although the activation barrier of the reaction is 181 kJ/mol, it was taken into consideration for the analysis of the Raman data. All in all, in this study the vibrational frequencies of the following species are considered: SbH_3, SbH_4F, SbH_4^+, SbH_2F and SbH_2^+. The formation of SbH_2^+ or SbH_2F is discussed in Chapter 2.5.3.4 in detail.

2.4.2.2 Calculated Vibrational Frequencies

The quantum chemical calculations are conducted at the MP2/aug-cc-pvtz level of theory and are scaled by a factor of 0.90, which is determined empirically. The deviation of the experimental frequencies of *Shimanouchi* and the calculated data is less than 3%. [87]

The predicted vibrational frequencies of SbH_4^+ are also in good agreement with the experimental data reported by *Kornath* and *Minkwitz* in 1994. [68] The Sb-H valence modes of SbH_2^+ are predicted at lower wavenumber than those of SbH_3 at 1927 and 1925 cm^{-1}. The comparison of SbH_3 and SbH_4^+ shows that the chosen level of theory reflects the experimental data in satisfying agreement. The vibrational frequencies of the antimony hydrogen species are summarized in TABLE 15 and TABLE 16.

TABLE 15: Summarized calculated and literature-known vibrational data of SbH_3, SbH_4^+ and SbH_2^+. Vibrational frequencies calculated on the MP2/MWB48/aug-cc-pvtz level of theory.

	Vibrational Frequencies [cm^{-1}]				
Assignment	SbH_3		SbH_4^+		SbH_2^+
	Calc.	Lit. (gas)	Calc.[d]	Lit. (SbF_6^-)	Calc. [d]
ν_{as} (SbH)	1872	1894 [b]	2042	2061[a]	1927
ν_s (SbH)	1868	1891 [c]	2021	2051[a]	1925
δ_{as} (SbH_2)	808	831 [b]	797	842[a]	
δ_s (SbH_2)	761	782 [b]	710	795[a]	824

[a] SbF_6^- salt described by *Kornath* and *Minkwitz* in 1994 [68]

[b] *Shimanouchi* in 1972 uncertainty 3~6 cm^{-1} [87]

[c] *Shimanouchi* in 1972 uncertainty 1~3 cm^{-1} [87]

[d] scaled with an empirical factor of 0.90

TABLE 16: Summarized calculated and literature-known vibrational data of SbH_4F and SbH_2F. Vibrational frequencies calculated on the MP2/MWB48/aug-cc-pvtz level of theory.

	SbH_4F		SbH_2F	
Assignment	Calc. [a]	Assignment	Calc.[a]	Assignment
ν_{as} (SbH)	1981	ν_{as} (SbH)	1859	ν (SbH)
ν_s (SbH)	1957	ν_s (SbH)	1855	ν (SbD)
ν (SbH)	1766	δ_s (SbH_2)	813	δ (SbHD)
δ (SbH)	900	δ_s (SbHF)	638	δ (SbHF)
δ_{as} (SbH)	817	δ_{as} (SbHF)	604	ν (SbF)
δ_s (SbH)	675	ν (SbF)	536	δ (SbDF)
δ (SbH)	448			
ν (SbF)	388			

[a] scaled with an empirical factor of 0.90

2.4.2.3 Raman Spectra of the System SbH_3 – HF

Raman spectra of the system SbH_3 – HF are depicted in FIG. 15. Due to the endothermic character of stibine, all spectra show vibrational modes of decomposition products. In order to identify, which Raman lines are caused by the decomposition products a matrix was gently evaporated, thus the less volatile decomposition products remain on the cold tip. The corresponding Raman spectrum is given in the FIG. 15. Raman spectra of pure SbH_3 in argon (S/M 1/50) exhibit three Raman lines. The one at 1892 cm^{-1} is assigned to the not resolved Sb-H stretching modes of SbH_3. The corresponding Sb-H deformation modes are observed at 827 and 732 cm^{-1}. The assignments are in good agreement with the data reported by *Shimanouchi* in 1972. [16] Co-condensation of stibine and HF with argon (S/M 1/300) yields four Raman lines in the region typical for Sb-H valence modes. The two lines at 1883 and 1880 cm^{-1} are assigned to the antisymmetric Sb-H and the symmetric Sb-H valence modes of SbH_3, with two corresponding Sb-H bending modes being observed at 824 and 781 cm^{-1}. In accordance with the quantum chemical calculations (2.4.2.2), the two remaining Raman lines at 1919 cm^{-1} and 1913 cm^{-1} are assigned to the antisymmetric and symmetric Sb-H valence modes of SbH_2^+. Here, the corresponding Sb-H deformation mode is observed overlaid with the antisymmetric bending mode of SbH_3 as a shoulder. All discussed vibrational data are listed in TABLE 17.

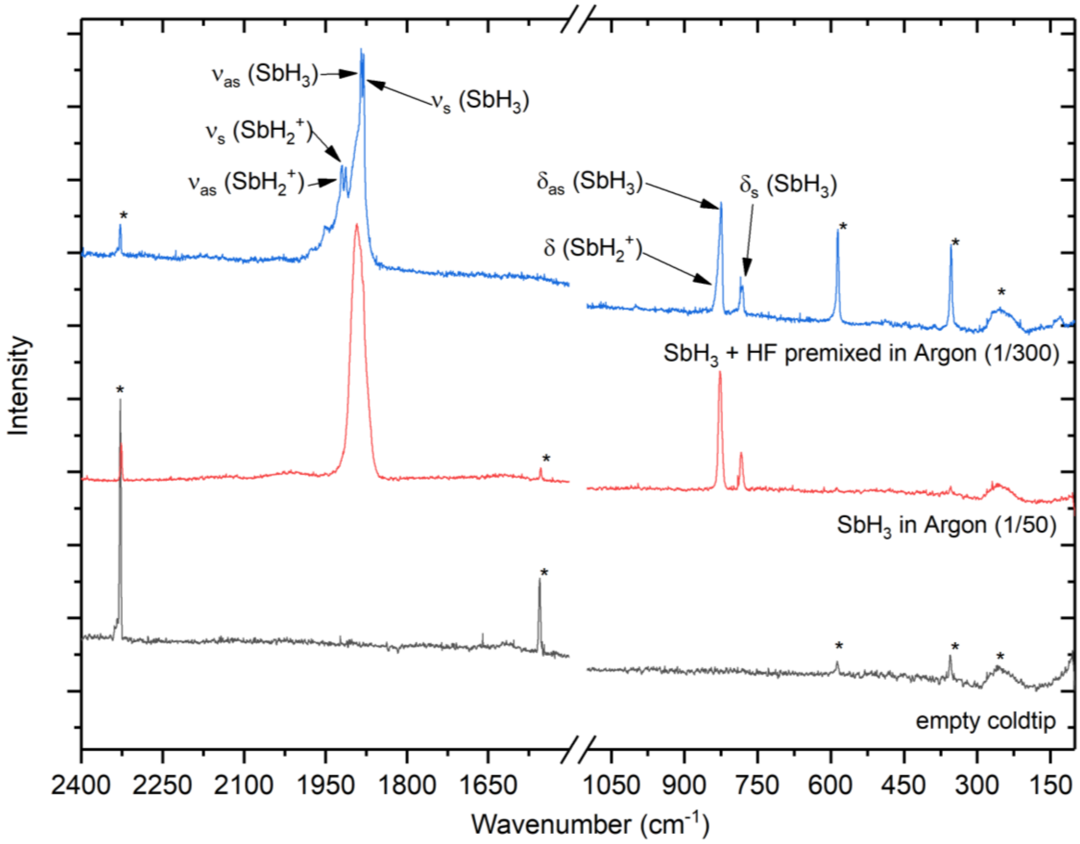

FIG. 15: Raman matrix spectra of SbH_3 co-condensed with and without HF in argon at 10 K (experimental conditions: 100 µm layer, laser wavelength 532 nm, laser power 1000mW, Raman intensity is normalized). * marks residues from decomposition on the cold tip.

TABLE 17: Summary of the vibrational frequencies of the system SbH_3 – HF in argon. Vibrational frequencies calculated on the MP2/MWB48/aug-cc-pvtz level of theory.

SbH_3				SbH_2^+		
Ra (1/50) exp	Ra (1/300) exp	Calc.	Lit.[a]	Exp.	Calc	Assig.
1892 (br)	1883	1872	1894 [b]	1919	1927	ν_{as} (SbH)
	1880	1868	1891 [a]	1913	1925	ν_s (SbH)
827	824	808	831 [b]	-	-	δ_{as} (SbH_2)
783	781	761	782 [b]	833 (sh)	824	δ_s (SbH_2)

[a] *Shimanouchi* in 1972 uncertainty 1~3 cm^{-1} [87]

[b] *Shimanouchi* in 1972 uncertainty 3~6 cm^{-1} [87]

2.4.3 CONCLUSION ON THE SYSTEM SbH_3 – HF

The quantum chemical calculations predict a lower stability for the tetrahedral SbH_4^+ and the trigonal-bipyramidal SbH_4F than for their lighter homologs. This prediction is reflected by the Raman matrix experiments. Under matrix isolation conditions in argon, only SbH_2^+ was observable. Neither SbH_4^+ nor SbH_4F were detected.

2.5 Theoretical comparative studies on the System PnH_3 – HX (Pn = P, As, Sb; X = F, Br)

In order to gain insight into the decomposition mechanisms and the energy minimum structures of the discussed species, extensive quantum chemical studies have been conducted. In the course of the theoretical investigation, the structure, stability and decomposition behavior of the species are discussed.

2.5.3.1 Calculated Structures at an Energy Minimum

The structures of the PnH_2^+, PnH_4^+ and PnH_4F (Pn = P, As, Sb) were calculated at the CCSD/aug-cc-pvtz level of theory. Additionally, MWB48 ECP was employed for the calculation for Pn being Sb. The optimized minimum structures are depicted in FIG. 16 and FIG. 17. The bond lengths and the bond angles are summarized in TABLE 18 and TABLE 19.

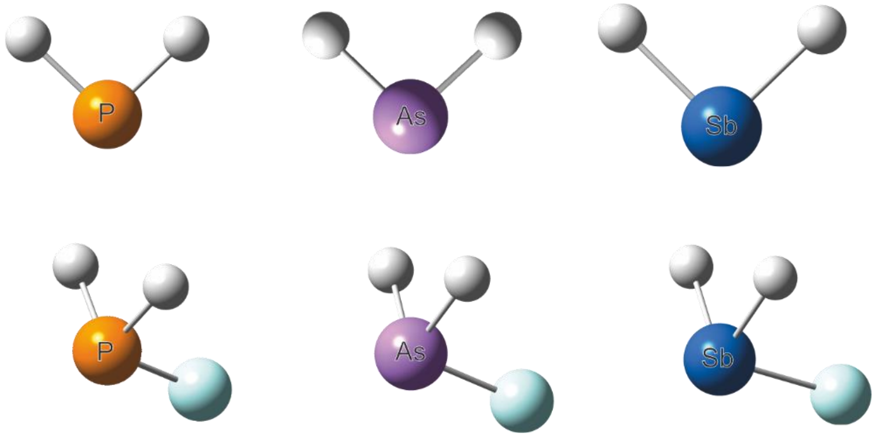

FIG. 16: Depicted molecular structures of the PnH_2^+ and PnH_2F (Pn = P, As, Sb) species calculated at the CCSD/aug-cc-pvtz level of theory. For the calculations of the species comprising antimony, the MWB48 ECP was employed. Structure parameters are summarized in TABLE 18.

TABLE 18: Structure parameters of PnH_2^+ and PnH_2F (Pn = P, As, Sb) species calculated at the CCSD/aug-cc-pvtz level of theory. For the calculations of the species comprising antimony, the MWB48 ECP was employed.

	PH_2^+	AsH_2^+	SbH_2^+	PH_2F	AsH_2F	SbH_2F
r (Pn-H)	1.42 Å	1.51 Å	1.67 Å	1.42 Å	1.51 Å	1.71 Å
r (Pn-F)b	-	-	-	1.62 Å	1.74 Å	1.93 Å
α (H-Pn-H)	92.7°	91.75°	90.98°	92.37°	91.59°	91.5°
β (H-Pn-F)	-	-	-	97.61°	95.37°	94.18°

The Pn-H bond is elongated if the Pn atom gets heavier and the H-Pn-H angle is reduced in the same manner. This is expected, as the Pn atom radius increases with its weight and the steric repulsion of the hydrogen and fluoride atoms is reduced. In comparison to the corresponding starting materials, PnH_3, *r* (Pn-H) of PnH_2^+ and PnH_2F is slightly shortened. A comparable shortening is observed if α (H-Pn-H) of PnH_2^+ and PnH_2F is compared to the corresponding H-Pn-H angle in PnH_3. [94-96] In the case of PnH_2^+ this predicted behavior is expected, because it has less hydrogen atoms than PnH_3 and therefore steric repulsion is less problematic. The P-F bond length in PH_2F is slightly longer than in PH_2F and is about the same length as P-F_{axial} in PH_2F_3. The P-F_{plane} bond in PH_2F_3 is longer than the P-F in PH_2F. [97] This differences are reasonable, because of the different binding situation in the trigonal bipyramidal PH_2F_3 molecule.

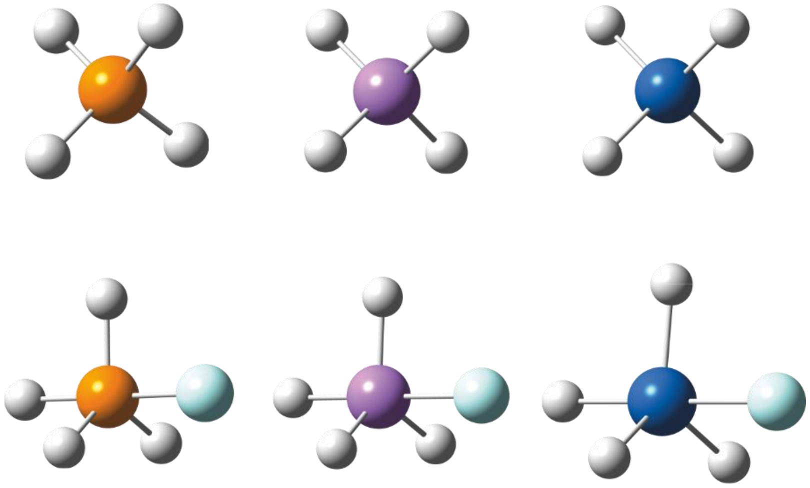

FIG. 17: Depicted molecular structures of the PnH_4^+ and PnH_4F (Pn = P, As, Sb) species calculated at the CCSD/aug-cc-pvtz level of theory. For the calculations of the species comprising antimony, the MWB48 ECP was employed. Structure parameters are summarized in TABLE 19.

TABLE 19: Structure parameters of PnH_4^+ and PnH_4F (Pn = P, As, Sb) species calculated at the CCSD/aug-cc-pvtz level of theory. For the calculations of the species comprising antimony, the MWB48 ECP was employed.

	PH_4^+	AsH_4^+	SbH_4^+	PH_4F	AsH_4F	SbH_4F
r (Pn-H_{eq})	1.40 Å	1.48 Å	1.66 Å	1.40 Å	1.48 Å	1.67 Å
r (Pn-H_{ax})	-	-	-	1.69 Å	1.85 Å	2.00 Å
r (Pn-F)	-	-	-	1.44 Å	1.54 Å	1.73 Å
α (H_{eq}-Pn-H_{eq})	109.47°	109.47°	109.47°	119.88°	119.42°	119.28°
β (H_{eq}-Pn-H_{ax})	-	-	-	87.98°	85.59°	85.29°
γ (H_{eq}-Pn-F)	-	-	-	92.02°	94.41°	94.70°

As observed before, the Pn-H bond is elongated and the H-Pn-H angle is reduced if the Pn atom gets heavier. This is expected, as the atom radius of Pn increases with its weight and the steric repulsion of the hydrogen and fluoride atoms is lowered. The PnH_4^+ cations and PnH_4F species show a shortened Pn-H bond compared to their corresponding starting material, due to the change of the hybridization and the therefore added s-orbital proportion to the bonding Pn-H hybrid orbitals. The H-Pn-H angle on the other hand is widened compared to PnH_3. [94-96] PH_4F exhibits a shorter P-F bond than PHF_4 or PH_2F_3 although it has the same binding character. [97]

2.5.3.2 Calculated Structures at an Energy Maximum (Transitions State)

Six transition states, which can be of interest for the decomposition of PnH_4^+ and PnH_4F into H_2 and PnH_2^+ (Pn = P, As, Sb) were optimized to a maximum on their potential energy surface employing the Berny algorithm and the Gaussian 09 program package. The chosen level of theory is a *Hartree Fock* calculation with a *Møller-Plesset* expansion truncated at second order and *Dunning's* correlation consistent triple-zeta basis sets aug-cc-pvtz. The frequency analysis of all optimized gas phase structures shows one imaginary frequency. This proves them as true transition states. The vector of this frequency is always consistent with the process of a hydrogen elimination. The structures of the transition states are depicted in FIG. 18. Bond lengths and bond angles are listed in TABLE 20.

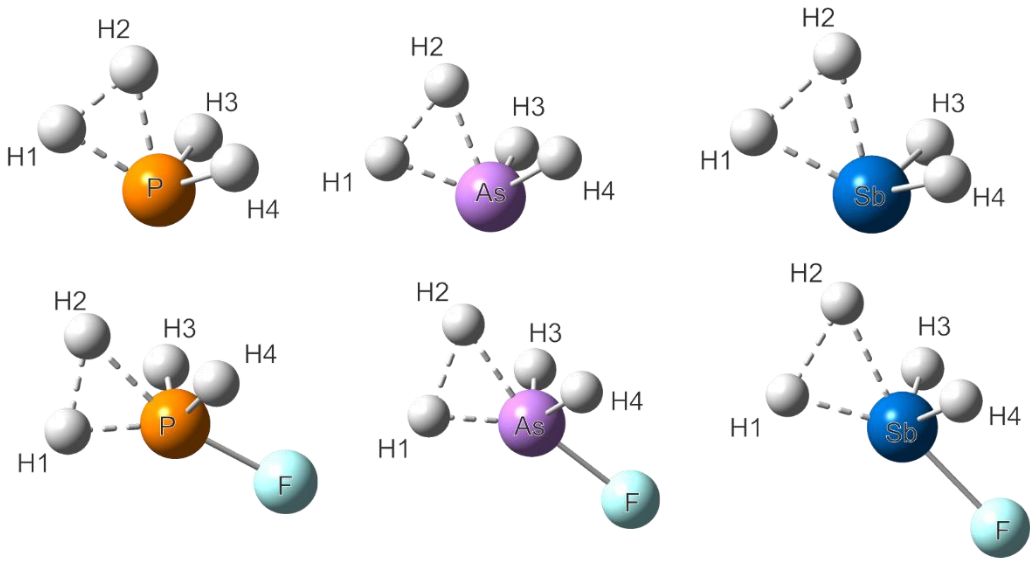

FIG. 18: Depicted molecular structures of the PnH_4^+-transition states and PnH_4F-transition states (Pn = P, As, Sb) species calculated at the MP2/aug-cc-pvtz level of theory. For the calculations of the species comprising antimony, the MWB48 ECP was employed. Structure parameters are summarized in TABLE 20.

TABLE 20: Structure parameters of PnH_4^+-transition states and PnH_4F-transition states (Pn = P, As, Sb) species calculated at the MP2/aug-cc-pvtz level of theory. For the calculations of the species comprising antimony, the MWB48 ECP was employed.

	PH_4^+-TS	AsH_4^+-TS	SbH_4^+-TS	PH_4F-TS	AsH_4F-TS	SbH_4F-TS
r (Pn-H1)	1.46 Å	1.52 Å	1.69 Å	1.43 Å	1.51 Å	1.69 Å
r (Pn-H2)	1.54 Å	1.62 Å	1.82 Å	1.65 Å	1.74 Å	1.95 Å
r (H1-H2)	1.15 Å	1.27 Å	1.42 Å	1.25 Å	1.38 Å	1.48 Å
r (Pn-H3/4)	1.41 Å	1.48 Å	1.66 Å	1.39 Å	1.47 Å	1.65 Å
r (Pn-F)	-	-	-	1.67 Å	1.83 Å	2.00 Å
α (H2-Pn-H3/4)	78.17°	78.92°	82.84°	78.08°	79.74°	80.38°
β (H1-Pn-H3/4)	104.68°	106.35°	108.82°	149.57°	147.59°	150.45°
γ (H1-Pn-H2)	44.89°	47.73°	47.45°	47.13°	49.48°	47.36°
Δ (H3-Pn-H4)	106.13°	108.07°	111.02°	123.25°	122.61°	122.29°
E (H2-Pn-H3/4)	-	-	-	99.97°	102.89°	102.71°

2.5.3.3 Single Point Energies of the Calculated Structures

The energies of the calculated structures were analyzed in order to gain better understanding of the experimental results discussed in previous Chapters. The single point energies of the structures were determined by calculation with the program set Gaussian 09. [62] These calculations were conducted after the optimization of the minimum structures and transition states at the MP2/aug-cc-pvtz level of theory and the CCSD/aug-cc-pvtz level of theory. The raw data is summarized in TABLE 21. The single point energies of PnH_4^+, PnH_4F, PnH_2^+ and PnH_2F are referenced to PnH_3 in kJ/mol (Pn = P, As, Sb). In general, the single point energies are consistent, irrespective whether they are calculated on the CCSD or MP2 level of theory, solely exhibiting minor differences.

TABLE 21: Differences of the single point energies of the PnH_2^+, PnH_2F , PnH_3, PnH_4^+ as well PnH_4F species and PnH_3 (Pn = P, As, Sb) and their transition states calculated at the MP2/aug-cc-pvtz and CCSD/aug-cc-pvtz level of theory in kJ/mol. The ECP MWB46 was employed for the calculation of species containing antimony. All energies are scaled to the single point energy of PnH_3.

	ΔE_{sp} at MP2/aug-cc-pvtz		ΔE_{sp} at CCSD/aug-cc-pvtz	
Species	Minimum	TS	Minimum	TS
PH_3	0	-	0	-
PH_4^+	-799	-573	-811	-578
PH_4F	-260857	-260696	-263406	-263236
PH_2^+	+2584	-	2607	-
PH_2F	-257828	-	-260338	-
AsH_3	0	-	0	-
AsH_4^+	-781	-573	-794	-577
AsH_4F	-260795	-260638	-263346	-263180
AsH_2^+	2524	-	2549	-
AsH_2F	-257822	-	-260331	-
SbH_3	0	-	0	-
SbH_4^+	-795	-578	-811	-591
SbH_4F	-260831	-260651	-263385	-263201
SbH_2^+	2400	-	2433	-
SbH_2F	-257867	-	-260369	-

By subtraction of the single point energy of the pnictogen hydride PnH_3 from the corresponding pnictogen hydrogen species, the calculated energies can be scaled to a comparable level. The single point energy differences of PnH_3 and PnH_4^+, PnH_4^+-TS or PnH_2^+ show a linear correlation, indicating that the energy difference between PH_3 and PH_4^+, for example, is comparable to the difference between AsH_3 and AsH_4^+. This is found for MP2 as well as for the CCSD calculations. The linear correlation is also found for the energetic difference between PnH_3 and the corresponding PnH_4F, PnH_4F-TS and PnH_2^+ species. CCSD and MP2 generate slightly different single point energies in the case of PnH_4F, PnH_4F-TS and PnH_2F. In FIG. 19 and FIG. 20 the single point energies of the pnictogen species are plotted.

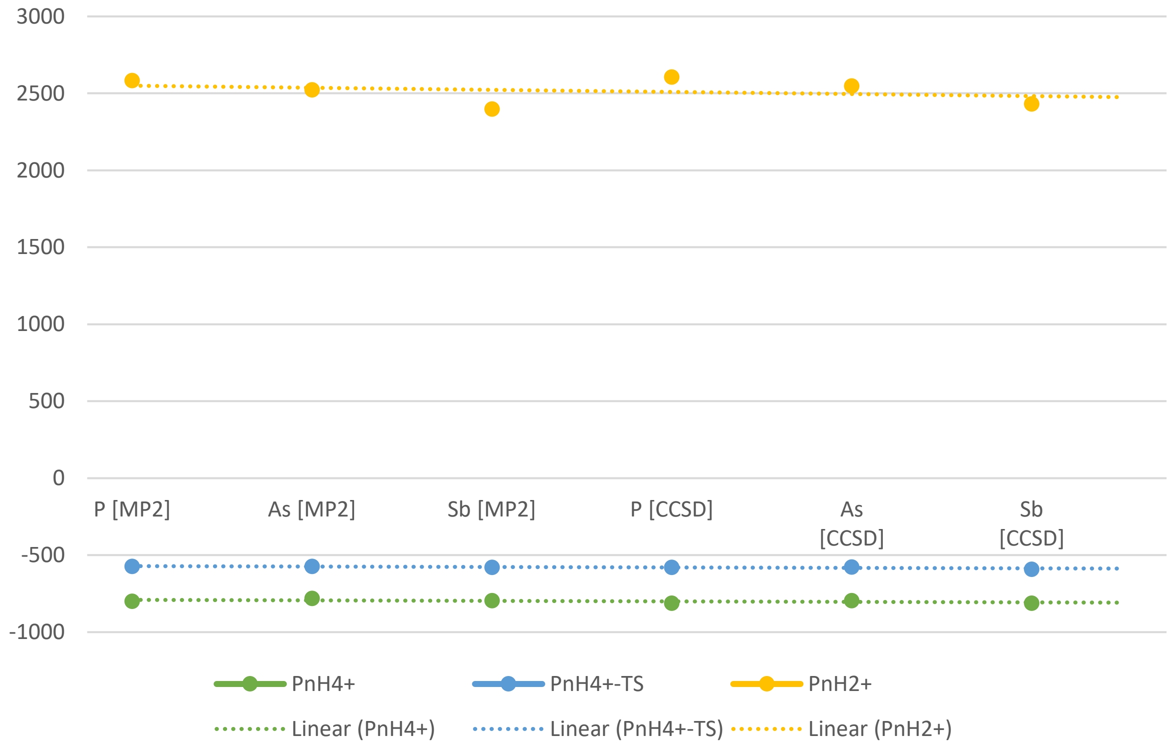

FIG. 19: Plotted energy differences ΔE_{sp} of the species PnH_4^+, PnH_4^+-TS and PnH_2^+. Single point energy values calculated on the MP2/aug-cc-pvtz and CCSD/aug-cc-pvtz level of theory. The ECP MWB46 was employed for the calculation of species containing antimony.

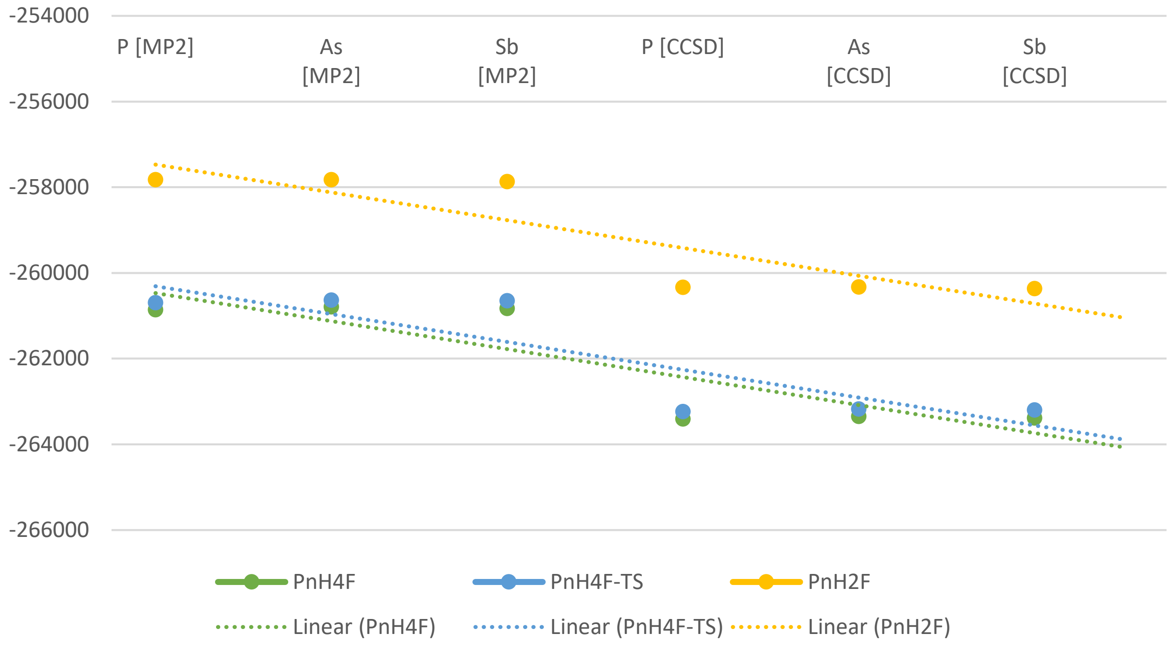

FIG. 20: Plotted energy differences ΔE_{sp} of the species PnH_4F, PnH_4F-TS and PnH_2F. Single point energy values calculated on the MP2/aug-cc-pvtz and CCSD/aug-cc-pvtz level of theory. The ECP MWB46 was employed for the calculation of species containing antimony.

2.5.3.4 Decomposition of PnH_4^+ to PnH_2^+ and Hydrogen

The Raman experiments indicate a high instability of the tetrahedral PnH_4^+ cation (Pn = P, As, Sb), which can only be observed by direct co-condensation at high noble gas dilutions for Pn = P and As. At the MP2/aug-cc-pvtz level of theory, PH_4^+, AsH_4^+ and SbH_4^+ are predicted to be 221, 173 and 101 kJ/mol more stable than $PH_2^+ + H_2$, $AsH_2^+ + H_2$ or $SbH_2^+ + H_2$ respectively. This theoretical observation stands in contrast to the experimental observations, which have been discussed in previous Chapters. In the experimental studies, PnH_4^+ structures (Pn = P, As) proved to be only isolable at high dilutions and in most experiments only PnH_2^+ was observed. Therefore, if PnH_4^+ is more stable than PnH_2^+ and H_2, the question arises why it is so difficult to stabilize and observe the PnH_4^+ species. The influence of the anion cation interaction and the hybridization barriers on the stability of PnH_4^+ is discussed in the following chapters. An overview of the decomposition energies is given in TABLE 22 and FIG. 21.

TABLE 22: Energy differences of the considered hydrogen eliminations calculated at the MP2/aug-cc-pvtz and CCSD/aug-cc-pvtz level of theory in kJ/mol. The ECP MWB46 was employed for the calculation of molecules containing antimony or iodine.

Species		MP2/aug-cc-pvtz	
1	**2**	ΔE_{sp} [**1**-(**2**+H_2)] in kJ/mol	ΔE_{sp} [**1**-TS] in kJ/mol
PH_4^+	PH_2^+	221	226
AsH_4^+	AsH_2^+	173	208
SbH_4^+	SbH_2^+	101	218
PH_4F	PH_2F	-5	163
AsH_4F	AsH_2F	-64	158
SbH_4F	SbH_2F	-75	181
PH_4Cl	PH_2Cl	-34	-
PH_4Br	PH_2Br	-40	-
PH_4I	PH_2I	-66	-
AsH_4Cl	AsH_2Cl	-82	-
AsH_4Br	AsH_2Br	-89	-
AsH_4I	AsH_2I	-120	-

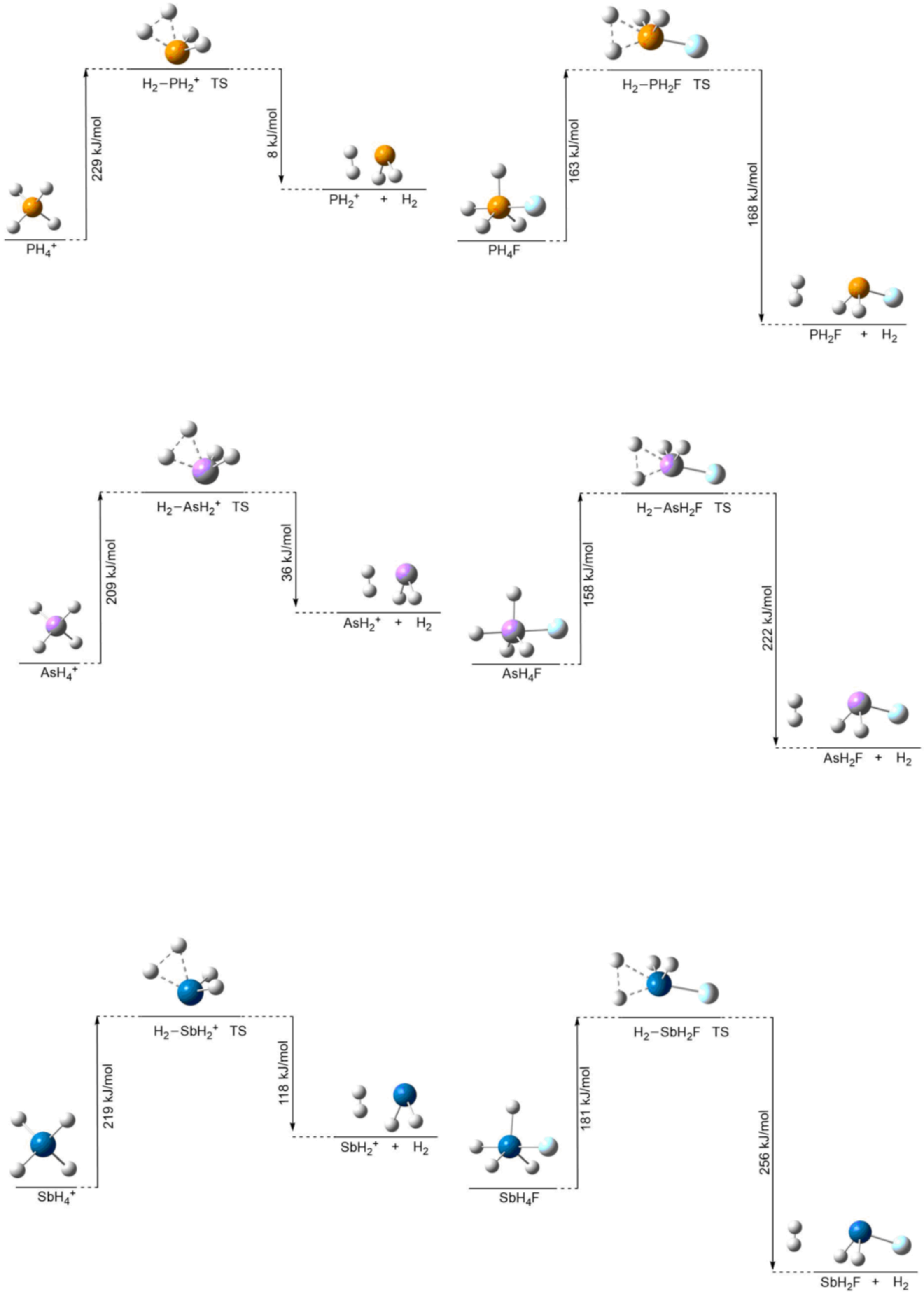

FIG. 21: Investigated ways of PnH_4^+ and $PnH_4^+F^-$ hydrogen eliminations calculated at the MP2/aug-cc-pvtz level of theory. The ECP MWB46 was employed for the calculation of species containing antimony.

2.5.3.5 Pn-F Distance and the Stability of the PnH_4^+ Moiety

In a thought experiment regarding the reactions of the system PnH_3 – HF two extreme points on the energy hypersurface from which the decomposition can start, can be taken into consideration. The first starting point is the PnH_4^+ structure which is not influenced by its counterion at all. The second start is a hypothetical covalently bound PnH_4F, which exhibits the strongest possible Pn-F interaction, a covalent Pn-F bond. Between these two extremes for the Pn-F interactions, various Pn-F interactions of different strength must be considered. As a start, the focus is directed on the two options. In the following these options are discussed with respect to arsine as an example. The energies of the discussed moieties are listed in TABLE 22. An overview of the reaction of AsH_3 – HF as an example is given in FIG. 22.

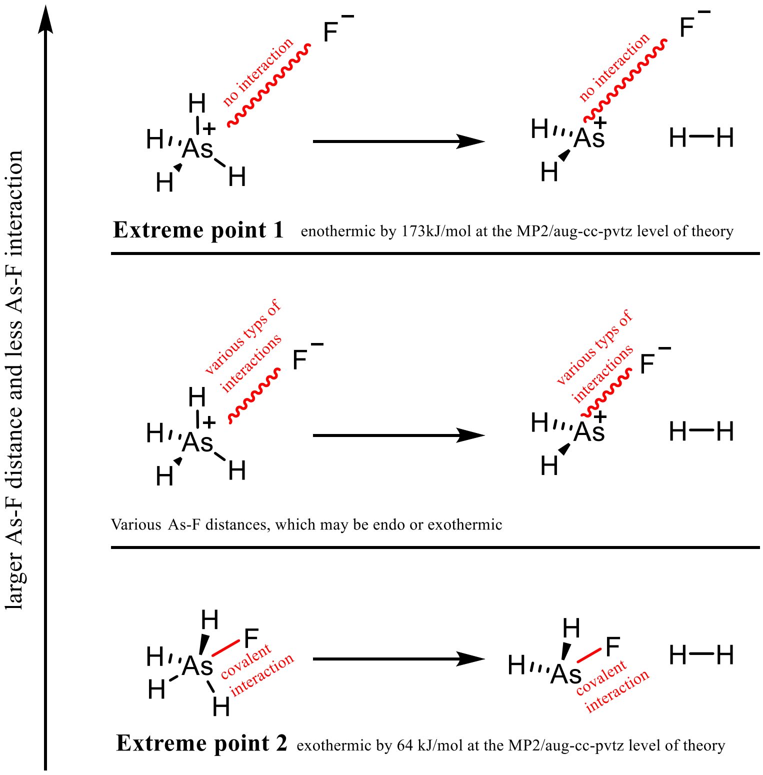

FIG. 22: Illustration of possible reaction pathways at different P-F distances for the hydrogen elimination of the system PH_3 – HF.

Hydrogen elimination option one, comprising the "naked" tetrahedron AsH_4^+ in the gas phase, is always endothermic by more than 150 kJ/mol. As result, a decomposition process without any ion pair interactions between AsH_4^+ and F^- is very unlikely. This applies for the case of AsH_4^+, whose decomposition to hydrogen and AsH_2^+ consumes 173 kJ/mol. In contrast, for the decomposition *via* option two, the covalently bound AsH_4F is energetically disfavored by 64 kJ/mol in the gas phase. A hydrogen elimination process of PH_4F and SbH_4F is also favored energetically. As result, it must be concluded that the interaction of the arsonium cation and the fluoride anion is responsible for the hydrogen elimination behavior. In a real matrix isolation environment, several interaction possibilities of varying strength, depending on the Pn – F distance must exist between the two extreme starting points. Here, the question is how long this Pn – F distance can be, while maintaining the influence on the stability of the PnH_4 moiety.

In order to investigate this influence, AsH_4F was modelled at its energetic minimum structure at the CCSD/aug-cc-pvtz level of theory with the program *Gaussian09*. [62] In a subsequent step, the As-F bond was elongated 400 times by 0.05 Å and the resulting geometry was optimized at the B3LYP/6-31g level of theory. The energy profile of the simulation is depicted in FIG. 23 and FIG. 24.

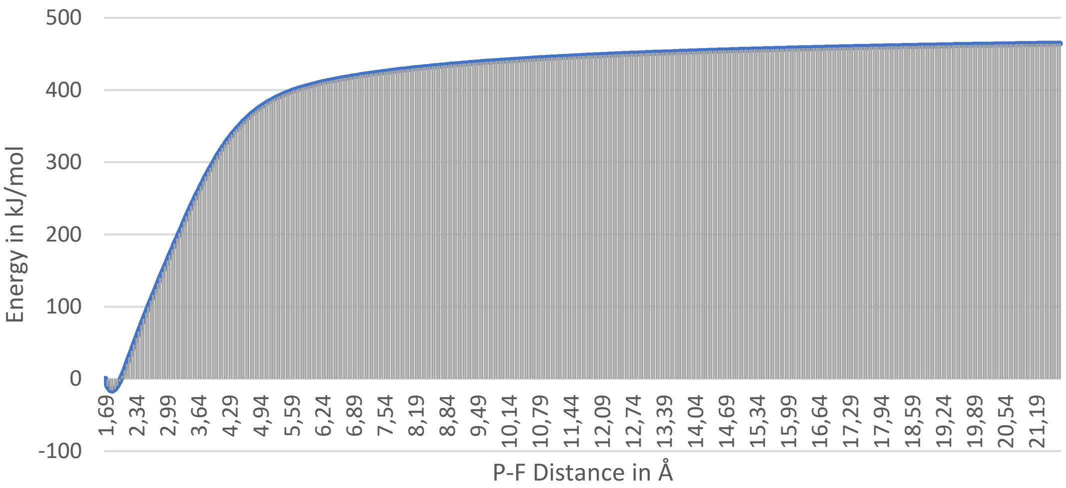

FIG. 23: Single point energies of $AsH_4^+F^-$ at different As-F distances at the B3LYP/6-31g level of theory.

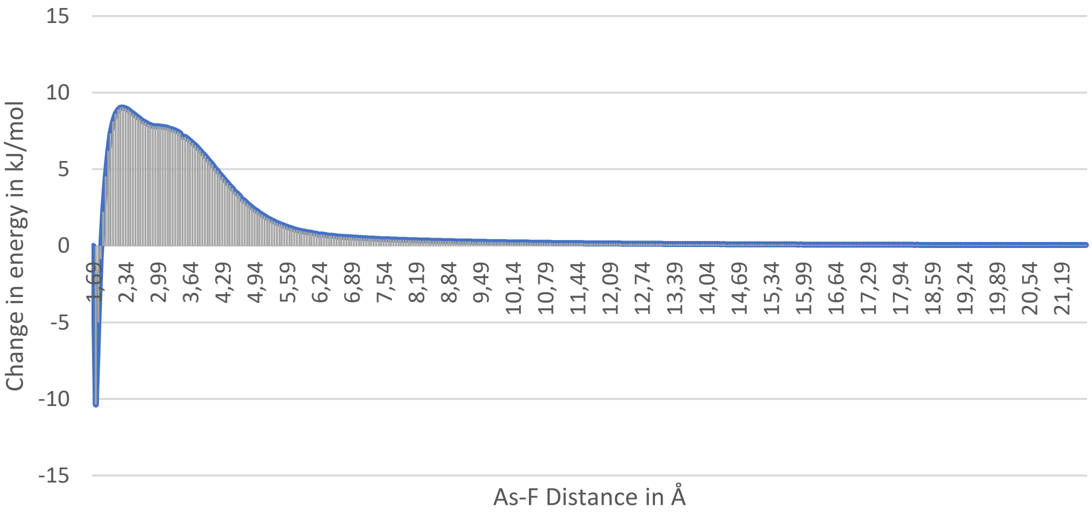

FIG. 24: Energy change of AsH_4F at different As-F distances at the B3LYP/6-31g level of theory.

The graph of the energy profile shows that the stability of AsH_4F decreases with the length of the As-F bond, due to the increasing charge separation. Here, the more interesting aspect is the degree of the influence at larger distances. Interestingly, the first step of the optimization is exothermic, which is an artefact of the low level of theory and the high quality of the starting structure for the experiment. Further discussion is provided in the reevaluation of the experiment at the M06/aug-cc-pvtz level of theory.

At an As-F distance of 5.80 Å, an elongation of 0.05 Å still accounts for a change of 1 kJ/mol. The van der Waals radius of arsenic and fluorine is 1.85 Å and 1.47 Å respectively, adding up to 3.32 Å. [98] This means that the van der Waals radii of As and F fit approximately 1.8 times in the distance of 5.80 Å. The van der Waals radius of argon is 1.88 Å. [98] Thus about 0.7 argon atoms fit between the counterparts of the ion pair. This way the hydrogen atoms are not taken into consideration, which is reasonable, because in the simulation the hydrogen atoms are pushed to the side by the fluoride atom. From the true-to-scale drawing (FIG: 25), we must conclude, that approximately one matrix layer of argon atom fits between the As and the F atom. Thus, the fluoride anion can lower the stability of the AsH_4^+ tetrahedron even if arsenic and fluoride are separated by one layer of argon atoms.

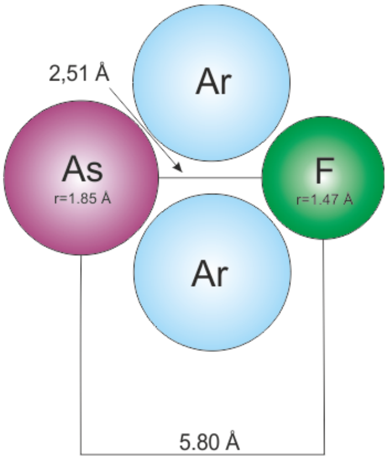

FIG: 25. 2D-Projection of the arsonium cation (hydrogens are neglected) and the fluoride anion inside an argon matrix

For a better consideration of the diffuse interactions, which are crucial for the energy quantification, the theoretical experiment was reevaluated at the M06/aug-cc-pvtz level of theory. The resulting single point energies are depicted in FIG. 26 and FIG. 27. Due to the resource demanding method, only 120 points on the energy hypersurface of $AsH_4^+F^-$ were simulated. The general trend of the experiment coincides with the experiment above.

In general, a destabilization of the system due to an elongation of the As-F interaction is observed. Owing to the higher quality of the quantum chemical method, none of the elongation steps is exothermic. The calculations at the M06/aug-cc-pvtz level of theory show that at an As-F distance of 5.8 Å a further extension of 0.05 Å causes an energy change of 1.7 kJ/mol. This difference of 58 % between the calculations at the B3LPY/6-31g and the M06/aug-cc-pvtz level of theory demonstrates the influence of the diffuse interactions, which are crucial for the discussion of the bonding situation in this case. At an As-F distance of approximately 2.0 to 3.7 Å, each further elongation of 0.05 Å in the As-F distance accounts for an energy shift of more than 6 kJ/mol. Thus, the As-F and therefore the Pn-F distance must have a severe impact on the stability of the PnH_4^+ F^- ion pair.

FIG. 26: Single point energies of AsH_4^+ F^- at different As-F distances at the M06/aug-cc-pvtz level of theory.

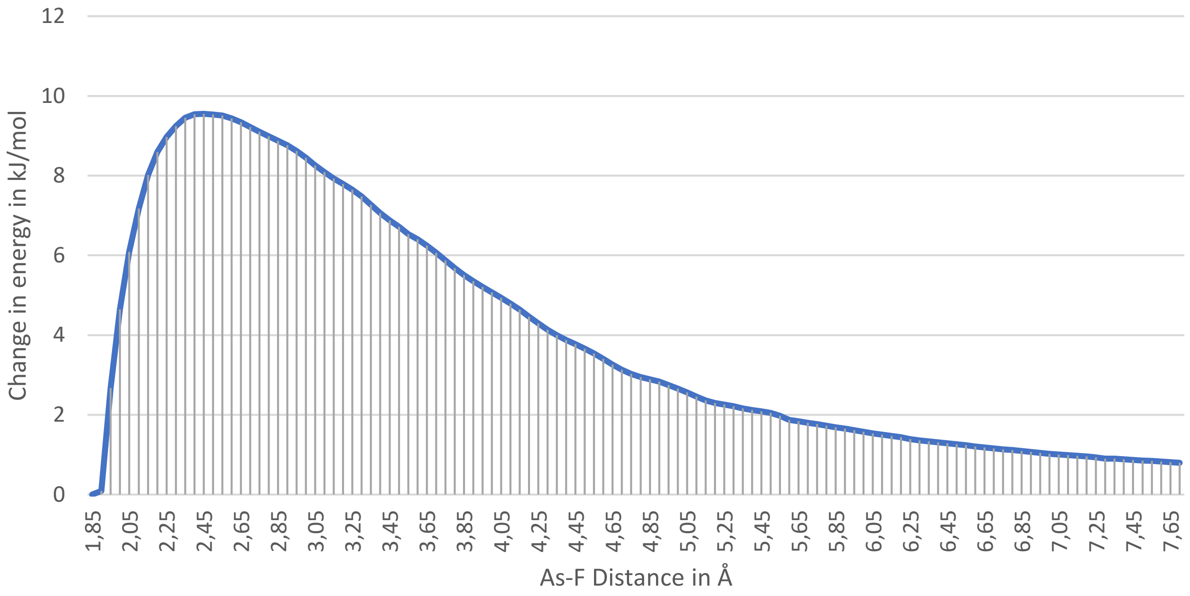

FIG. 27: Energy change of AsH_4F at different As-F distances at the M06/aug-cc-pvtz level of theory.

Consequently, the question arises at which As-F distance the AsH_4^+ moiety becomes a perfect tetrahedron, given that throughout the Raman experiments no $PnH_4^+X^-$ species with a symmetry lower than T_d was observed. If the above discussed data set, containing the 120 single point minimum structures is analyzed, a perfect tetrahedral H-As-H angle of 109.5° is found at an As-F distance of 3.25 Å. This distance is similar to the sum of the van der Waals radii of As and F (3.32 Å). At an As-F distance of 2.85 Å the H-As-H angle is already widened to 107.9°. Some exemplary key structures are depicted in FIG. 28

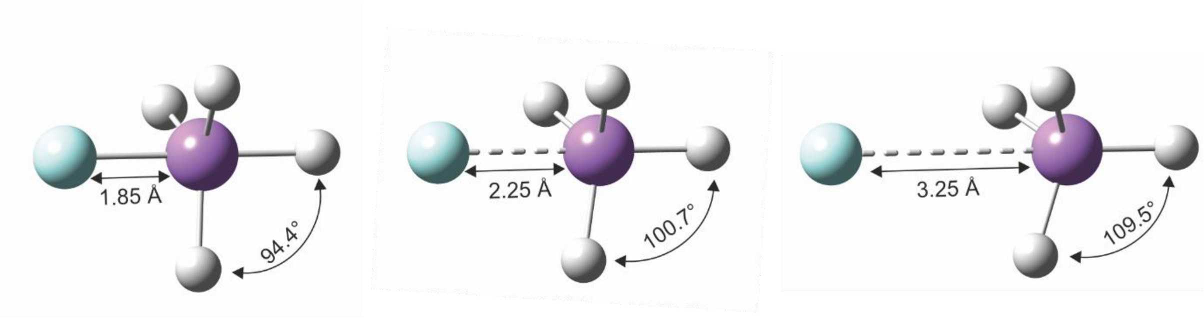

FIG. 28: Minimum structures of AsH_4^+ and F^- at different As-F interactions examples for the influence of fluoride on the PnH_4^+ geometry at the M06/aug-cc-pvtz level of theory.

As already discussed, at an As-F distance of 3.25 Å and larger, the $AsH_4^+ F^-$ species is a ideal tetrahedron and only two valence As-H modes can be detected by Raman spectroscopy. In the matrix isolation experiments discussed earlier, tetrahedral PnH_4^+ (Pn = P, As) was only observable at high dilutions, whilst PnH_2^+ was observed under all examined experimental conditions. Taking the simulation results into consideration, it makes sense that PnH_4^+ is only stable at high dilutions. The higher the dilution, the greater is the probability that the distance between Pn and F is large enough to minimize the effect of the fluoride on the PnH_4^+ moiety. Consequently, the PnH_4^+ species is less destabilized and can be detected in the matrix isolation experiments by Raman spectroscopy. Thus, in general, in experiments comprising pure solid $PnH_4^+X^-$ species (Pn = P, As, Sb; X = Cl, Br, I, AsF_6^-, SbF_6^-), lattice stabilization effects must overcompensate destabilizing effects, which are dominant under matrix isolation conditions. [35, 40, 86, 99] Pure solid $PH_4^+ I^-$ is, for instance, known as a stable compound. [40]

Not only the distance of the halogen ion to the pnictogen center influences the stability. A variation of the halogen anion shows a crucial impact on the stability of the PnH_4X (Pn = P, As / X = F, Cl, Br, I) species. Single point energies of the optimized minimum structures are summarized in TABLE 22. A general trend can be identified for reactions in the gas phase: The heavier and larger the halogen ion, the more energy is released when the $PnH_2^+ X^-$ species (X = F, Br) is formed. In pure solid samples this is again compensated by lattice effects.

2.5.3.6 Hybridization Effects and the Stability of PnH_4^+

The amount of energy needed during the elimination process decreases with the weight of the pnictogen atom. Thus, the PnH_4^+ (Pn = P, As, Sb) cation is more stable if the pnictogen atom is lighter. This effect is explained by the hybridization effect. In his review from 1984 *Kutzelnigg* lists three different reasons for isovalent hybridization. The first reason is that hybrid orbitals cause a better overlap and ensure a stronger bonding to the bonding partner. The second reason for hybridization is that the addition of p-character to the s-orbital sterically moves it away from Pn-H bonds. As a result of this hybridization, the *Pauli* repulsion is minimized. The third reason is present if the hybridization leads to an enlargement of the valence angle, which causes a reduction of the *Pauli* repulsion as well.

Irrespective of the reason for hybridization, the s-orbital must be energetically promoted to the p-orbitals in order to form the hybrid orbital. Consequently, at first glance the amount of energy needed for the hybridization depends on the energy difference between the s- and the p-orbitals, which must be overcome. Therefore, the energy needed for the hybridization may be considered as a hybridization barrier. The composition of this barrier is discussed later. In the pnictogen group the trend to form hybrid orbitals declines with the increase of the pnictogen atom’s weight, because the energy difference between the 3s and 3p orbitals is smaller than between the 4s and 4p or 5s and 5p orbitals. As a result, this hybridization barrier increases with the atomic number of the pnictogen atom. Whilst sp^3-hybridization is inevitable for the formation of PnH_4^+ and PnH_4F, it becomes obsolete with the elimination of hydrogen and the hybridization fades. During this dehybridization process, depicted in FIG. 29, an amount of energy, which is proportional to the size of the hybridization barrier, is released.

- Protonation forces sp^3-hybridization
- Hybridization barrier energy has to be overcome

- Hydrogen elemination destroys hybridization
- Hybridization barrie energy is released

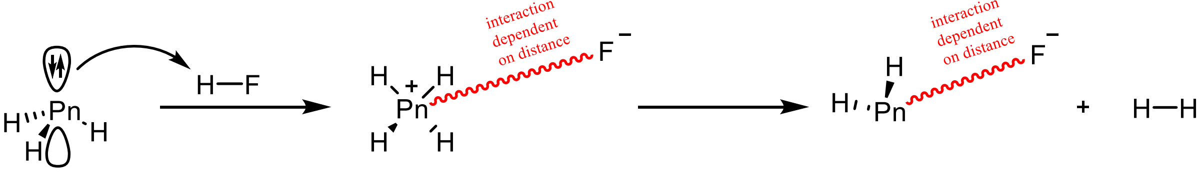

no sp-hybridization
H-Pn-H angle ~ 90°

Pn = P, As, Sb

sp^3-hybridization
H-Pn-H angle > 105°

no sp-hybridization
H-Pn-H angle ~ 90°

FIG. 29: Illustration of the hybridization and dehybridization during the generation of $PnH_2^+ F^-$.

Due to the reasons discussed later in this chapter, depending on the pnictogen atom’s weight, more energy is generated during the dehybridization of SbH_4^+ or SbH_4F than for its phosphorus containing analogs. After the hydrogen elimination, PnH_2^+ or PnH_2F are no longer sp^3-hybridized and the gained energy increases with the pnictogen’s weight in the investigated moiety. Therefore, SbH_4^+ is more likely to decompose than AsH_4^+ or PH_4^+. This explanation is consistent with the Raman experiments, in which AsH_4^+ and PH_4^+ were observed, whilst SbH_4^+ was not.

In order to quantify the hybridization barrier, the unhybridized s- and p-orbitals were simulated at the CCSD/aug-cc-pvtz level of theory for NH_4^+, PH_4^+, AsH_4^+ and SbH_4^+. In this theoretical experiment the exact quantitative comparison is only possible between the first three cations, because for the calculation of SbH_4^+ the ECP potential MWB48 was employed. The results are depicted in FIG. 30. As not expected, the energy difference between the s- and the p-orbitals decreases with the weight of the pnictogen atom. The values are consistent with the Atomic Energy Levels summarized by *Moore* in 1949. [100] According to the simulations, heavier pnictogen hydrides are expected to form hybrid orbitals more easily, which is however not the case in experimental chemistry. Consequently, the energies of the s- and p-AOs cannot solely be responsible for the behavior observed in the matrix experiments.

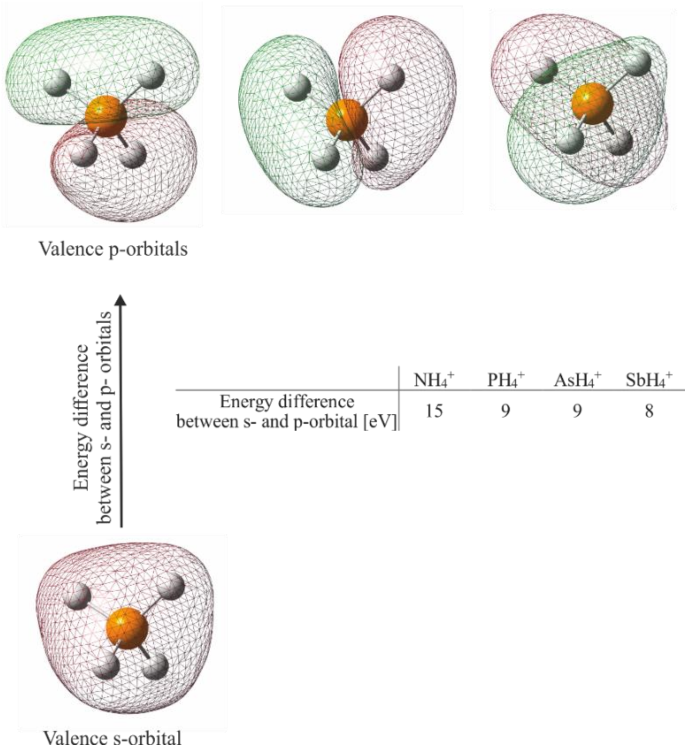

	NH_4^+	PH_4^+	AsH_4^+	SbH_4^+
Energy difference between s- and p-orbital [eV]	15	9	9	8

FIG. 30: Energy difference between the valence s-orbital and the valence p-orbitals of NH_4^+, PH_4^+, AsH_4^+ and SbH_4^+. Energies calculated on the CCSD/aug-cc-pvtz level of theory. The ECP MWB46 was employed for the calculation of species containing antimony.

Not only the energetic difference between s- and p-AOs is relevant for the chemical behavior, but the localization of the orbitals is also important. If the distance of the valence electrons in s- and p-orbitals r_s and r_p from the atom core is considered, it can be observed that the heavier the pnictogen atom, the larger becomes the difference between r_s and r_p orbitals. Quantum chemical calculations by *Desclaux* at a relativistic level of theory also show this increase. [101] *Kutzelnigg* summarizes this effect in his review to a great extent and states that the r_s and r_p only differ by 10% in the second period. This difference rises via 20-33% in the third period to 24-40% in the fourth and fifth period. [101] After all, this localization difference of the electrons in the s- and p-orbitals has a larger impact on the hybridization barrier of the PnH_4^+ moiety than the calculated energetic difference between the valence s- and p-orbitals. Thus, the trend to dehybridize becomes stronger with the weight of the pnictogen atom Pn and more energy is generated with the formation of $PnH_2^+F^–$.

In order to understand the elimination process, not only the thermochemistry of the starting material and product is of interest, but the energy to overcome the transition state also has to be taken into consideration. All found transitions states are exothermic compared to the PnH_4^+ or PnH_4F species. The discussed PnH_4F (Pn = P, As, Sb) transition states are less stable than those of PnH_4^+ The activation barrier of the decomposition of PH_4F is higher than that of AsH_4F. Due to the employment of the ECP potential for the calculation of the stibonium salts, a comparison with the phosphonium and the arsonium salt is not possible. Nevertheless, the activation barrier seems to be higher, the lighter the pnictogen atom is. For our calculations of NH_4F, no reasonable decomposition path was found. Therefore, we conclude that the activation barrier of the hydrogen elimination of SbH_4F is lower than that of PnH_4F (Pn = N, P, As). This theoretical result is also backed up by the fact that high amounts of antimony and arsenic were found on the cold tip surface of the matrix isolation apparatus.

There are several possible ways to overcome this activation barrier. Inside the reservoir cylinder or matrix isolation apparatus collisions or catalytic interactions with the walls are reasonable possibilities. The low pressure of only 500 mbar inside the reservoir cylinder is likely to favor the hydrogen elimination, too. The same is true for the low pressure of 10^{-6} bar inside the matrix isolation apparatus. During the travel from the reservoir to the cold tip, collisions with the tube walls of the matrix isolation apparatus and of course with the cold tip itself are inevitable. The energy of the laser light (532nm, 225 kJ/mol) used for the Raman spectroscopy also is high enough to decompose the onium species. Finally, intermolecular decomposition reactions comprising two or more onium species cannot be excluded.

2.6 Conclusion on Pnictogen Hydrides and Hydrogen Halides under Extra-Terrestrial Conditions

Pnictogen hydrides react with hydrogen fluoride or hydrogen bromide to PnH_4^+ cations (Pn = P, As, Sb) under matrix isolation conditions. Whether these cations are stable or not depends on the distance between the pnictogen central atom and the formed anion. At high dilutions (S/M>1/100), the tetrahedral PH_4^+ and AsH_4^+ species were observed, whilst SbH_4^+ was not observed under the chosen conditions. The energetic destabilization of SbH_4^+ is caused by the hybridization, which is inevitable in order to form the tetrahedron, and the very different s- and p-orbital distances to the atom core, which make a hybridization unfavorable.

Irrespective of the S/M ratio the degradation products PnH_2^+ (Pn = P, As, Sb) are observed in each experiment. The amount of hydrogen elimination products depends on the distance between the pnictogen cation and the halogen anion. This distance seems to increase with the S/M ratio. Quantum chemical simulations indicate that even if one matrix layer of atoms is located between the cation and the anion, the change of the Pn – X (Pn = P, As, Sb; X = F) distance has an impact on the energy of the PnH_4^+ species and can result in a destabilization of the cation. This influence cannot be observed in the Raman experiments as the T_d symmetry already is formed at an As-F distance of 3.25 Å according to quantum chemical simulations. At this distance, a change of 0.05 Å still accounts for a destabilization of approximately 7 kJ/mol. At closer distances, a C_{3v}-like symmetry for the $PnH_4^+ F^-$ ion pairs are expected. This symmetry degradation of a tetrahedron, which is accompanied by the splitting of the two Pn-H stretching modes into three Pn-H valence modes, was not observed. As a result, we must conclude that under the chosen conditions, the $PnH_4 F^-$ ion pairs exhibit a Pn-F distance of at least 3.25 Å in the matrix. The interaction of PnH_2^+ and F^- was investigated in the case of the AsH_2^+ F^- ion pair experimentally. Depending on the S/M ratio, AsH_2^+ F^- ion pairs as well as AsH_2F were observed.

In the isothermal layer (160 K) of the Jovian atmosphere (90-290 km) [102], the existence of such a PnH_4^+ species may be possible on a very fast time scale, but according to the experimental data, decomposition processes by hydrogen elimination occur. The same must be assumed for the 0.5 - 2 bar pressure range of Saturn's atmosphere, which exhibits a temperature range of 100 – 160 K. At a pressure of 0.1 bar temperatures are significantly lower. Jupiter's temperature is 112 K and Saturn's temperature is 84 K. [36] At these temperatures we assume a higher probability for the formation of PnH_4^+ species.

3 Investigation on the Dimerization of Arsanyl in noble Gas Matrices (Prepared Manuscript)

Florian Zischka[1] and Andreas J. Kornath,[1a]

[1] *Inorganic Chemistry, Department of Chemistry, Ludwig-Maximilians-University Munich, Butenandtstr. 5-13-(D) in 81377 Munich, Germany*

Abstract: AsH_2 was generated from arsine (AsH_3) by thermolysis and characterized by Matrix Isolation Raman spectroscopy at 10 K in a solid argon matrix. The structure obtained from quantum chemical calculations at the CCSD/aug-cc-pvtz level of theory is discussed with respect to MO theoretical calculations and a comparison to the arsanyl cation is given. In subsequent dimerization studies As_2H_4 was observed Raman spectra at 10 K. The spectroscopic assignment is supported by quantum chemical calculations at the CCSD/aug-cc-pvtz level of theory. The calculated the molecular structure of As_2H_4 a the CCSD/aug-cc-pvtz level of theory shows an As-As bond length 2.449 Å and C_{2h} symmetry.

3.1 INTRODUCTION

Although arsine has been known for a long time, it still is a key example for an endothermic molecule, which slowly degrades into its elements at room temperature. Its instability is already a topic in chemistry undergraduate education, due to its analytical use in the *Marsh test*. [70] Nowadays, arsine is of great importance in the semiconductor industry as a precursor for the synthesis of gallium arsenide. [103-106] Several mechanisms for the production of GaAs involve the dissociation of AsH_3 into AsH_2, AsH and elementary arsenic. Therefore, the study of its dissociation products provides precious insights in the formation of GaAs. AsH_2 can be generated from AsH_3 by 193.3 nm irradiation and detected by HRTOF mass spectroscopy. [107]

The electronic spectrum of AsH_2 was studied by *Dixon* in 1967 for the first time and a first insight in the molecular structure of the ground and excited state was derived from the rotational constants. [108] In 1986, the photolysis at 193.0 nm, detected by emission spectroscopy, was reported for the first time. [109] Microwave spectroscopy was conducted by *Saito*, providing a complete set of molecular constants and an estimated equilibrium structure for AsH_2 and AsD_2. [110, 111] In the most recent years, further studies employing laser induced fluorescence spectroscopy and cavity ring-down spectroscopy have been reported. [112, 113] All these studies propose geometries and even provide limited information about the vibrational data, which were mainly deduced from rotational constants. [112, 113] According to these studies the ν_s (AsH) and δ (H-As-H) are derived to occur at 2096 cm^{-1} and 981 cm^{-1} respectively. The ν_{as} (AsH) has not yet been detected or deduced from experiments. In summary, some vibrational modes have been derived from different spectroscopic experiments, but not detected directly by vibrational spectroscopy.

Even less information is available regarding its dimer As_2H_4, although its existence was already supposed by decomposition experiments in 1947 carried out by *Nast*. [114] Using modern analytic techniques, the hydrazine analogous molecule has so far only been reported by mass spectroscopy in silent discharge experiments. [115] In terms of reaction, the dissociation of AsH_3 to AsH_2 is not limited to photolytic conditions. Pyrolysis at atmospheric and low pressures also yields AsH_2. [116-118] This prompted us to investigate, if As_2H_4 could be generated by the dimerization of AsH_2 generated from AsH_3 by thermolysis.

3.2 Experiment, Apparatus and Materials

The matrix isolation apparatus consists of a standard high vacuum pumping system and a gas mixing unit. In order to perform the condensation of the gas mixtures, the cryostat (ARS 202B) is cooled by a closed-cycle helium refrigerator to 10 K. The cold tip attached to the cryostat consists of a copper block, which is coated with silver. Argon (99.9996%) and nitrogen (99.996%) (Messer Griesheim) were dried over P_4O_{10}. Xenon (99.99%) was used without purification. AsH_3 was synthesized from Zn_3As_2 and diluted sulfuric acid according to the literature. [44] For the thermolysis, a thermolysis cell comprising a tantalum filament was used. The apparatus for the Multichannel Raman Matrix Isolation Spectroscopy is described in detail elsewhere. [43]

The layers containing As_2H_4 and AsH_2 were prepared by passing AsH_3 from a reservoir vessel over a tantalum filament heated to elevated temperatures. The pressure decay in the reservoir vessel can by tracked by a pressure sensor. The thermolysis vapor was mixed with the noble gas stream in front of the cold tip and condensed together with the inert gas flow of approximately 4 mmol (100 cm^3 at standard temperature and pressure) at a flow rate of 3 mmol/h (75 cm^3/h). The substrate to matrix ratio (S/M-ratio) was calculated with respect to the pressure changes and the known container volumes. A drawing of the apparatus is shown in the supporting information in FIG S. 5. After 1-2 h a white homogenous layer has formed. Annealing cycles showed no influence on the Raman spectra up to the evaporation temperature of the host material. If needed, a layer of nitrogen was added for the calibration of the Raman spectrometer. The Raman spectra were detected with a CCD Raman spectrometer (Jobin-Yvon T64000). A frequency doubled Nd: YAG DPSS laser (Cobolt 05-01 Series Samba; 532 nm) was used as a light source with an angle of 55°. After evaporation of the matrix, arsenic remains as a metallic residue on the cold tip, due to a partial decomposition of AsH_3 and AsH_2.

3.3 RESULTS AND DISCUSSION

3.3.1 Raman Spectroscopy

A comprehensive overview of the obtained Raman spectra is shown in FIG. 32. The observed frequencies and the quantum chemically calculated frequencies are listed in . According to the quantum chemical calculations, AsH_3 exhibits C_{3v} symmetry. Therefore, the four fundamental vibrations are all Raman active. At a S/M ratio of 1/100 in argon, the antisymmetric As-H valence vibration of AsH_3 is recorded at 2152 cm^{-1} and the symmetric As-H valence vibration at 2142 cm^{-1}. According to the quantum chemical calculations, the ν_{as} and ν_s are expected at 2171 cm^{-1} and 2146 cm^{-1} respectively and are hence slightly overestimated by the calculations. The δ_{as} (H-As-H) of arsine is observed at 1003 cm^{-1} and the δ_s (H-As-H) is observed at 915 cm^{-1}. Both experimental values are slightly underestimated by our quantum chemical calculations, which predict the δ_{as} (H-As-H) at 990 cm^{-1} and the δ_s (H-As-H) at 892 cm^{-1}. In experiments performed at lower dilutions, the Raman lines are slightly red-shifted, due to higher substrate to substrate interactions. In samples containing a larger amount of the arsenic species, the red-shifted As-H valence vibrations of AsH_3 **(2)** are detected at 2130 and 2116 cm^{-1}. These values are in good agreement with the frequencies derived from literature. [87]

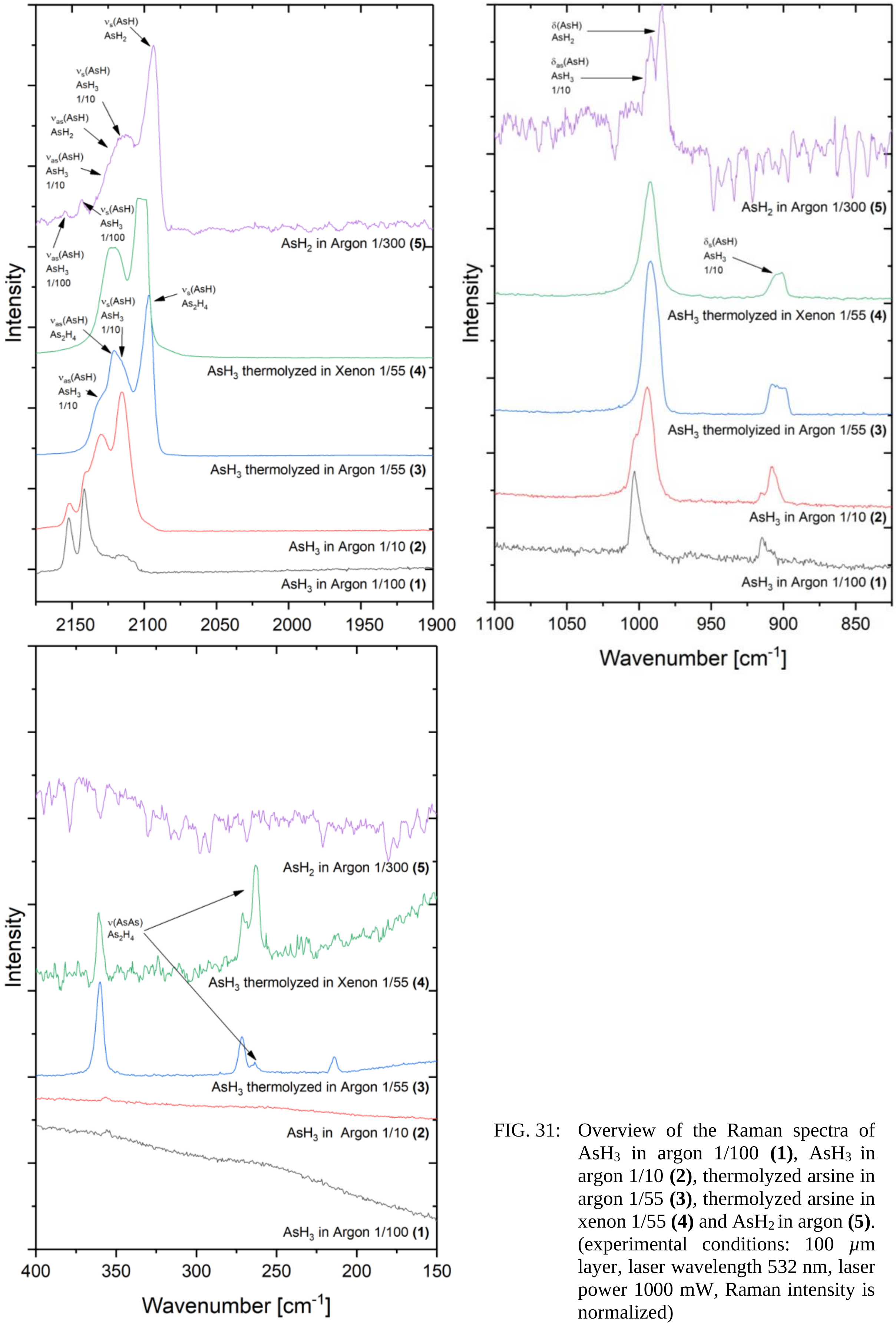

FIG. 31: Overview of the Raman spectra of AsH_3 in argon 1/100 **(1)**, AsH_3 in argon 1/10 **(2)**, thermolyzed arsine in argon 1/55 **(3)**, thermolyzed arsine in xenon 1/55 **(4)** and AsH_2 in argon **(5)**. (experimental conditions: 100 µm layer, laser wavelength 532 nm, laser power 1000 mW, Raman intensity is normalized)

According to quantum chemical calculations, AsH_2 exhibits C_{2v} symmetry and three Raman active vibrations. The antisymmetric and symmetric AsH stretching vibrations of AsH_2 are shifted by 50 cm^{-1} towards lower wavenumbers compared to AsH_3. This shift is in accordance with the quantum chemical calculations, which only slightly overestimate the ν_s. In the present study, the antisymmetric As-H stretching vibration is observed at slightly higher wavenumbers at 2117 cm^{-1}. In spectrum **(5)**, the ν_s (As-H) of the AsH_2 radical is recorded at 2094 cm^{-1}, which is in good agreement with the value extracted from LIF spectroscopy by *Clouthier* and *He* in 2007. [112] The quantum chemical calculations overestimate the ν_s by 33 cm^{-1}. The identification of the H-As-H bending modes of all the AsH species superimposing with the H-As-H bending modes of AsH_3 is difficult. In experiment **(5)**, the resolution is high enough to distinguish the δ_{as} (H-As-H) of AsH_3 (1/10) **(2)** from the δ (H-As-H) of AsH_2 at 983 cm^{-1}. The value of this vibrational mode is in good agreement with v=981 cm^{-1} derived from absorption spectroscopy by *Chen* in 2009. [113]

According to quantum chemical calculations, As_2H_4 exhibits C_{2h} symmetry. Consequently, ten fundamental vibrations are expected, but only four exhibit a satisfyingly strong Raman activity. The As-H stretching modes of As_2H_4 (ν_{as} = 2123 cm^{-1}, ν_s = 2099 cm^{-1}) are recorded in the same range as the As-H stretching modes of AsH_2. The resulting superposition constitutes a challenge identifying AsH_2, since the existence of AsH_2 in the experiments **(3)** and **(4)** cannot be excluded. This superposition is illustrated in FIG. 32 in spectrum **(3)**, with the As-H stretching modes of AsH_3 being observed as shoulders of the As-H stretching modes of As_2H_4 and AsH_2 at 2130 cm^{-1} and 2116 cm^{-1}. From the discussion of the As-H stretching modes we may conclude that experiments **(3)** to **(5)** contain a mixture of at least AsH_3 and AsH_2. The H -As-H bending modes of As_2H_4 cannot be detected, due to their low Raman intensity and the superposition with the bending modes of AsH_3. Due to the comparable As-H vibrations of AsH_2 and As_2H_4, the most meaningful vibration for the identification of the dimer is the As-As stretching mode. The quantum chemical calculations predict this vibration at 253 cm^{-1}. Experimentally, it is observed as a well resolved Raman line at 266 cm^{-1} in the spectra **(3)** and **(4)**. This value is comparable to the As-As valence mode observed in liquid *trans* and *gauche* $As_2(CH_3)_4$, which was identified by *Durig* at 272 cm^{-1} and 254 cm^{-1} respectively. [119] At this point it should be stated that the Raman spectrum contains As_4 as a decomposition product, but the line at 266 cm^{-1} does not belong to a As_4 vibration. The ν_s of As_4 is observed at 362 cm^{-1}. The other As-As modes of the As_4 tetrahedron are recorded at 274 cm^{-1} and 216 cm^{-1}. These values are in satisfying agreement with values reported by the literature at the low dilutions, which are needed to observe the dimerization of AsH_2. [120]

TABLE 23: Experimental, literature and calculated frequencies of AsH_3, AsH_2 and As_2H_4. Vibrational frequencies were calculated at the CCSD/aug-cc-pvtz level of theory and are given in cm^{-1}. Raman intensities are calculated at the MP2/aug-cc-pvtz level of theory and are listed in Å^4/u. (Fractions are S/M Ratio; Numbers in brackets are Raman intensities)

AsH_3 Ra 1/100	AsH_3 Ra 1/10	AsH_3 Lit. [b]	AsH_3 Calc. [a]	AsH_2 Ra	AsH_2 Lit.[c]	AsH_2 Calc. [a]	As_2H_4 Ra	As_2H_4 Calc.[a]	Assignment.
2152 (67)	2130 (70)	2123	2171 (36)	2117 (50)	-	2146 (48)	2123 (70)	2143 (50)	ν_{as} (AsH)
2142 (100)	2116 (18)	2116	2146 (100)	2094 (100)	2096	2129 (100)	2099 (100)	2131 (100)	ν_s (AsH)
1003 (19)	1001 (18)	1003	990 (2)	-	-	-	-	-	δ_{as} (HAsH)
-	-	-	-	983 (15)	981	975 (2)	-	-	δ (HAsH)
915 (6)	914 (6)	906	892 (1)	-	-	-	-	963 (3)	δ_s (HAsH)
-	-	-	-	-	-	-	266 (5)	253 (5)	ν (AsAs)

[a] Optimization and vibrational frequencies were calculated at the CCSD/aug-cc-pvtz level of theory. Raman Intensities are calculated at the MP2/aug-cc-pvtz level of theory.

[b] Gas phase IR values. [87]

[c] Lit. [112, 113]

3.3.2 Theoretical Calculations

All calculations regarding the optimization vibrational analysis were performed at the Coupled Cluster Singles and Doubles (CCSD) post Hartree Fock coupled cluster method and Dunning's correlation consistent basis set aug-cc-pvtz. [45-49, 56-61] Raman intensities were calculated at the second order *Møller Plesset* perturbation theory MP2/aug-cc-pvtz. [50-55] The calculated values listed in TABLE 24 are compared with the experimental frequencies of the condensed species.

AsH_2 possess a calculated H-As-H angle of 91.26° and an As-H bond length of 1.513 Å. Compared to values derived from experiments by *Dixon*, *Saito*, *Clouthier* and *Chen*, the H-As-H angle is slightly overestimated and the As-H bond is underestimated. [108, 111-113] In summary, the calculated structural parameters are in reasonable agreement with the reported data. The calculated geometric parameters of AsH_2 are compared to the experimental values derived from various studies and listed in TABLE 24.

TABLE 24: Geometry of AsH_2 calculated at the CCSD/aug-cc-pvtz level of theory and geometry parameters from the literature.

	Calc.	*Dixon* [108]	*Saito* [111]	*Clouthier* [112]	*Chen* [113]
$\theta_{\text{H-As-H}}$	91.26°	90.44°	90.79°	90.75°	90.77°
$r_{\text{As-H}}$	1.513 Å	1.518 Å	1.516 Å	1.518 Å	1.525 Å

The structure of AsH_2 is very similar to that of AsH_2^+described in Chapter 2.2.3. A comparison of the calculated parameters is given in TABLE 25 and depicted in FIG. 32. The two species AsH_2 and AsH_2^+ merely differ in their number of electrons. The arsanyl cation may be considered as the oxidation product of the arsanyl radical. Comparing the geometric parameters, the close relationship is undeniable. The bond lengths are essentially unchanged by the oxidation of the arsanyl radical. The H-As-H angle is widened in the AsH_2^+ cation compared to the AsH_2 radical only slightly.

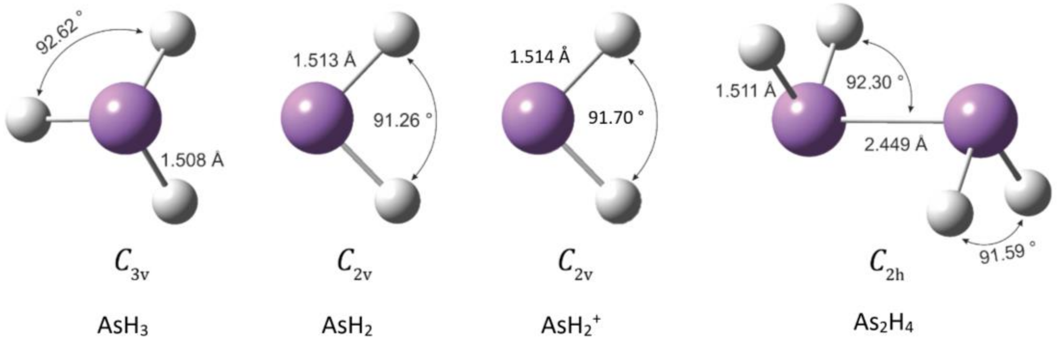

FIG. 32. Optimized structures of AsH_3, AsH_2, AsH_2^+ and As_2H_4 calculated at the CCSD/aug-cc-pvtz level of theory.

TABLE 25: Physical parameters of AsH_2, AsH_2^+ and As_2H_4. Geometric parameters and energy calculated at the CCSD/aug -cc-pvtz level of theory and geometry parameters from the literature.

	$\theta_{\text{H-As-H}}$[a]	$r_{\text{As-H}}$[a]	ν_{as} [cm^{-1}] [b]	ν_s [cm^{-1}] [b]	Energy [kJ/mol] [a,c]
AsH_2^+	91.70°	1.514 Å	2184	2173	0
AsH_2	91.26°	1.513 Å	2117	2094	−904
As_2H_4	92.30°	1.511 Å	2123	2099	−1009

[a] Calculated at the CCSD/aug-cc-pvtz level of theory.
[b] Experimental values.
[c] The energy of AsH_2^+ is used as an origin and considered as zero. The zero-point energy of As_2H_4 is divided by two in order to give a comparable value.

The comparison of the molecular orbitals, which are shown in FIG. 33, provides a deeper understanding of the similarity between AsH_2 and AsH_2^+. In AsH_2^+ the LUMO is positioned orthogonal to the H-As-H plane and the HOMO-LUMO-gap of 17.14 eV is high. Naturally, the HOMO p-orbital, which contains the unpaired electron of arsanyl is orthogonal to the H-As--H plane. Therefore, no overlap with the LUMO, which is in the H-As-H plane can be observed and no elongation of the As-H bonds is predicted. Forming As_2H_4 and pairing the electrons is exothermic by −211 kJ/mol, according to quantum chemical calculations. (TABLE 25)

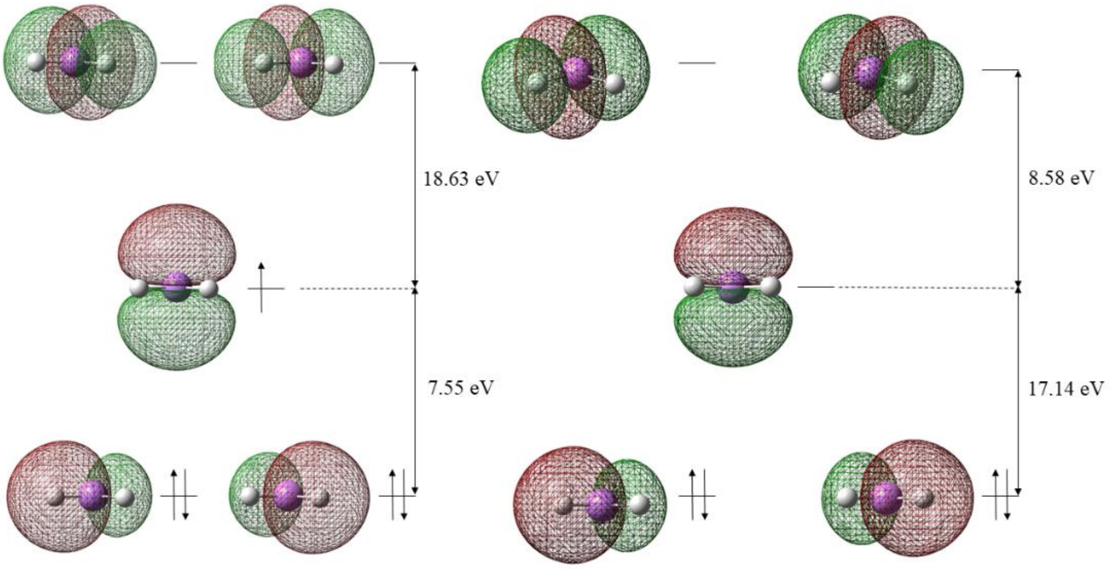

FIG. 33. MO-diagram of AsH_2 (left) and AsH_2^+ (right) calculated at the CCSD/aug-cc-pvtz level of theory.

If two of the occupied LUMOs of AsH_2 come together, As_2H_4 is formed. The As-H valence modes of As_2H_4 are observed at 2123 cm^{-1} and 2099 cm^{-1} in the matrix isolation experiments. The quantum chemical calculations slightly overestimate the experimental values and predict the As-H valence modes at 2143 cm^{-1} and 2131 cm^{-1}. The ν (As-As) is observed at 266 cm^{-1} and calculated at 253 cm^{-1}. Altogether, the experimental and calculated values are in reasonable agreement. According to the quantum chemical calculations, As_2H_4 exhibits an almost unchanged As-H bond compared to AsH_2 with 1.511 Å. Moreover, the H-As-H angle is slightly widened to 91.50° in comparison to AsH_2. The H-As-As angle is 92.30° and the As-As bond length is 2.449 Å, which is longer than the As-As bond of $As_2(Me)_4$ (2.433(2) Å). [121] An overview of the structural parameters is given in TABLE 25 and depicted in FIG. 32.

3.4 CONCULSION

Arsine was passed over a heated filament and thermolyzed. The thermolysis products were diluted with a noble gas, condensed on a cold tip and investigated by Raman spectroscopy. The analysis of the Raman spectra shows, depending on the S/M ratio, the formation of AsH_2 and As_2H_4. Characteristic for the As_2H_4 is the As-As vibration at 266 cm^{-1}. According to quantum chemical calculations, the As-As bond has a length of 2.449 Å. The arsanyl radical has a H-As-H angle of 91.26° and a As-H bond length of 1.513 Å, which is almost identical to the molecular structure of the AsH_2^+ cation.

SUPORTING INFORMATION (Chapter 3)

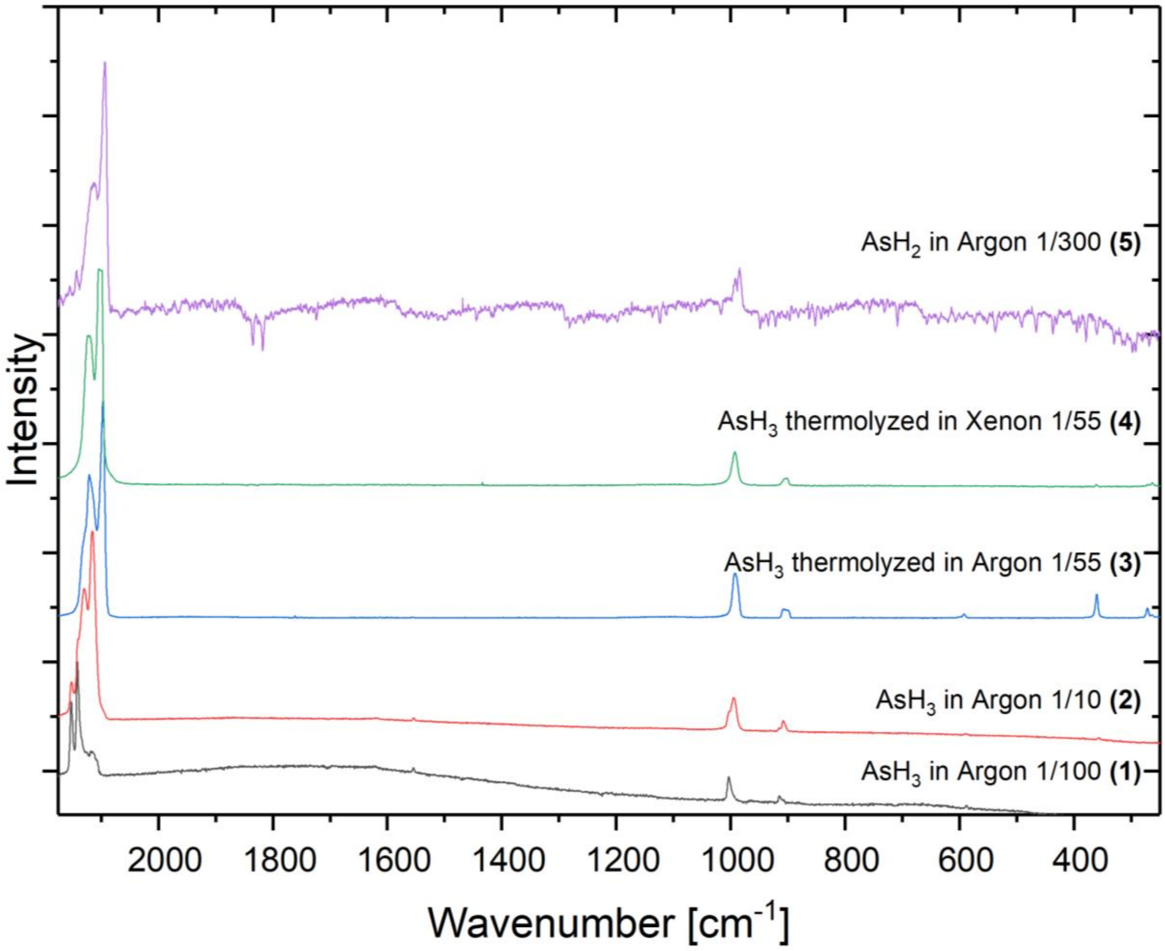

FIG S. 4: Overview of the experiments of thermalized AsH_3 in argon and xenon. (experimental conditions: 100 μm layer, laser wavelength 532 nm, laser power 1000 mW, Raman intensity is normalized)

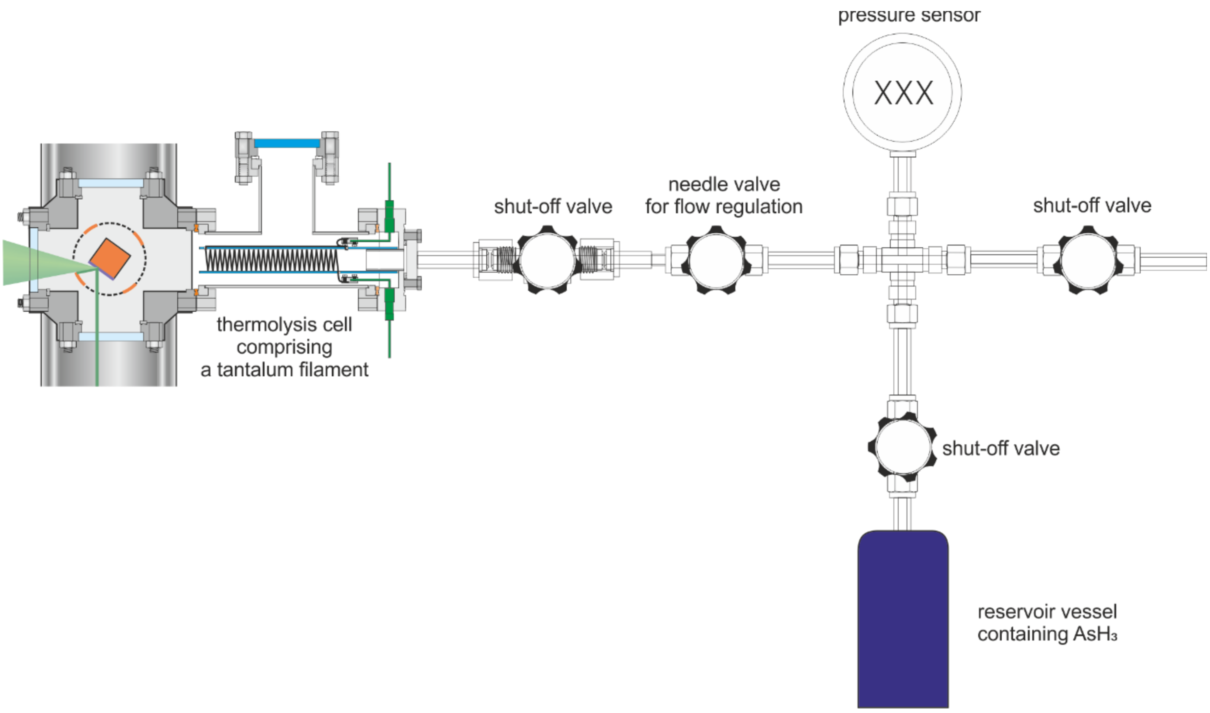

FIG S. 5: Apparatus for thermolysis of AsH_3.

Cartesian coordinates of AsH_2 optimized at the CCSD/aug-cc-pvtz level of theory.

0.0000	0.0000	0.0605	As
0.0000	1.0816	-0.9976	H
0.0000	-1.0816	-0.9976	H

Cartesian coordinates of As_2H_4 optimized at the CCSD/aug-cc-pvtz level of theory.

0.0000	1.2247	-0.0000	As
1.0516	1.2853	1.0839	H
1.0525	1.2854	-1.0831	H
0.0000	-1.2247	-0.0000	As
-1.0516	-1.2853	1.0839	H
-1.0525	-1.2854	-1.0831	H

TABLE S 5: Experimental, literature and calculated frequencies of AsH_3, AsH_2, As_2H_4 and As_4. (Fractions are S/M Ratio; Numbers in brackets are Raman intensities)

AsH_3 Ra 1/100	AsH_3 Ra 1/10	AsH_3 Lit. [87] [b]	AsH_3 Calc. [a]	AsH_2 Ra	AsH_2 Lit.[112, 113]	AsH_2 Calc. [a]	As_2H_4 Ra	As_2H_4 Calc. [a]	As_4 Ra	As_4 Lit. [120]	As_4 Calc. [a]	Assignment
2152 (67)	2130 (70)	2123	2171 (36)	2117 (50)	-	2146 (48)	2123 (70)	2143 (50)	-	-	-	ν_{as} (AsH)
2142 (100)	2116 (18)	2116	2146 (100)	2094 (100)	2096	2129 (100)	2099 (100)	2131 (100)	-	-	-	ν_{s} (AsH)
1003 (19)	1001 (18)	1003	990 (2)	-	-	-	-	-	-	-	-	δ_{as} (AsH)
-	-	-	-	983 (15)	981	975 (2)	-	-	-	-	-	δ (AsH)
915 (6)	914 (6)	906	892 (1)	-	-	-	-	963 (3)		-	-	δ_{s} (HAsH)
-	-	-	-	-	-	-	-	725 (1)	-	-	-	δ_{s} (HAsAs)
-	-	-	-	-	-	-	266 (5)	253 (5)	-	-	-	ν (AsAs)
-	-	-	-	-	-	-	-	-	362 (100)	356	-	ν_{s} (AsAs)
-	-	-	-	-	-	-	-	-	274 (50)	266	-	ν_{as} (AsAs)
-	-	-	-	-	-	-			216 (27)	208	-	ν (AsAs)

[a] Optimization and vibrational frequencies were calculated at the CCSD/aug-cc-pvtz level of theory. Raman intensities are calculated at the MP2/aug-cc-pvtz level of theory.

[b] Gas phase IR values

4 Spectroscopic Studies of Di- and Tetra-Phosphorus in Adamantane Matrices – an approach to room temperature stable matrices. (Prepared Manuscript)

Florian Zischka[1], Alexander Kaufmann[2], Lukas Flierl[1], Michael Feller[1], Thomas Bräuniger[1] and Andreas Kornath*[1]

[1] *Inorganic Chemistry, Department of Chemistry, Ludwig-Maximilians-University Munich, Butenandtstr. 5-13-(D) in 81377 Munich, Germany*

[2] *F-Select GmbH, Semmelweisstrasse 5 (D) in 82152 Planegg Germany*

Abstract: White phosphorus and mixtures of P_4 and P_2 are deposited in adamantane by condensation in a specially developed high vacuum apparatus. The samples are characterized by ^{31}P MAS NMR spectroscopy and Raman spectroscopy. NMR experiments at low temperatures provide information about the mobility of P_4 inside the host. The experimental NMR shifts are in good agreement with quantum chemical calculations at various levels of theory depending on the calculated model size. Furthermore, Raman spectra at low temperatures were measured. The vibrational modes of P_4 and P_2 in an adamantane matrix display a line splitting, which is discussed in combination with the results of the NMR experiments.

4.1 INTRODUCTION

In his book Historia inventionis Phosphori (1710) *Gottfried Wilhelm Leibniz* used the Latin phrase "*ignis quidem tectus*", meaning hidden fire to emphasize the high flammability of white phosphorus. [122] The origin of this behavior is the strong P-O bond of the oxidation products (330 to 650 kJ mol^{-1}) as well as the weak P-P bonds of white phosphorus (bond dissociation energy, BDE_{p-p} = 200 kJ mol^{-1}) resulting in the well-known high flammability. Its lighter homolog nitrogen exhibits a BDE of 945 kJ/mol. [123] The flammability is not the only difference between phosphorus and its lighter homolog. Dinitrogen exists as a very stable N_2 molecule, whereas the very unstable analogous phosphorus species P_2 is only producible by breaking the P_4 bonds at high temperatures. Vice versa, the N_4 molecule seems to be existent but very unstable. [124, 125]

Even more than 300 years after its discovery the use of white phosphorus remains a great challenge in synthesis applications. The less stable diphosphorus still is not isolable at room temperature. Until now it has only been isolated by matrix isolation at 15 K. [126] Strategies to trap P_4 in host frameworks, in order to minimize the inherent synthetic risks, are of great interest. Different techniques aiming for this goal have been investigated extensively.

One of the recent examples is the encapsulation of P_4 in $[(ZnI_2)_3(TPT)_2]_n$ (TPT=2,4,6-tris(4-pyridyl)-1.3.5-triazine) *via* gas phase diffusion by *Kawano*, using a metal organic framework (MOF) as the host material. [127] The air and light stable storage of white phosphorus was also achieved by *Wu et al.* employing an Anion-Coordination-Based Tetrahedral Cage. [128] A self-assembling capsule was used by *Nitschke* in 2009, which allows P_4 to be obtained by replacing it with benzene and dissolving it into the organic solvent. [129] In 2018 *Scheer et al.* were able to store white phosphorus in a porous material made from activated carbon. Its use as a reagent was verified by synthesizing several compounds containing phosphorus for the first time. [130]

In all these studies ^{31}P MAS NMR spectroscopy is the key analytic method in order to verify whether the storage material was loaded with white phosphorus and if the tetrahedral structure is still intact. All the ^{31}P NMR signals observed in these studies show a remarkably sharp signal for solid state compounds. The most prominent study showing this effect is the synthesis of $(P_4)_2C_{60}$ in 1994. In this study, the half-line band width ($\omega_{1/2}$) only is 55 Hz. [131, 132] Until now an enormous effort has been made to synthesize and characterize phosphorus storage compounds for subsequent syntheses, but only little research concerning the interactions of white phosphorus with its carrier material has been reported. This prompted us to examine the interactions of phosphorus in adamantane matrices.

4.2 RESULTS AND DISCUSSION

4.2.1 Preparation of the MAS NMR Samples

The samples of P_4 in adamantane were prepared using a specially designed gram scale co-condensation apparatus. A schematic drawing of the apparatus is presented in FIG. 34. It consists of a cylindrical, rotatable copper cold tip (2) (diameter 40 mm) mounted to the recipient with a custom-built ultra-high vacuum rotational feedthrough (1) (manufactured by *Ferrotec*), which ensures leak ratios below 10^{-6} mbarLs^{-1} throughout rotation.

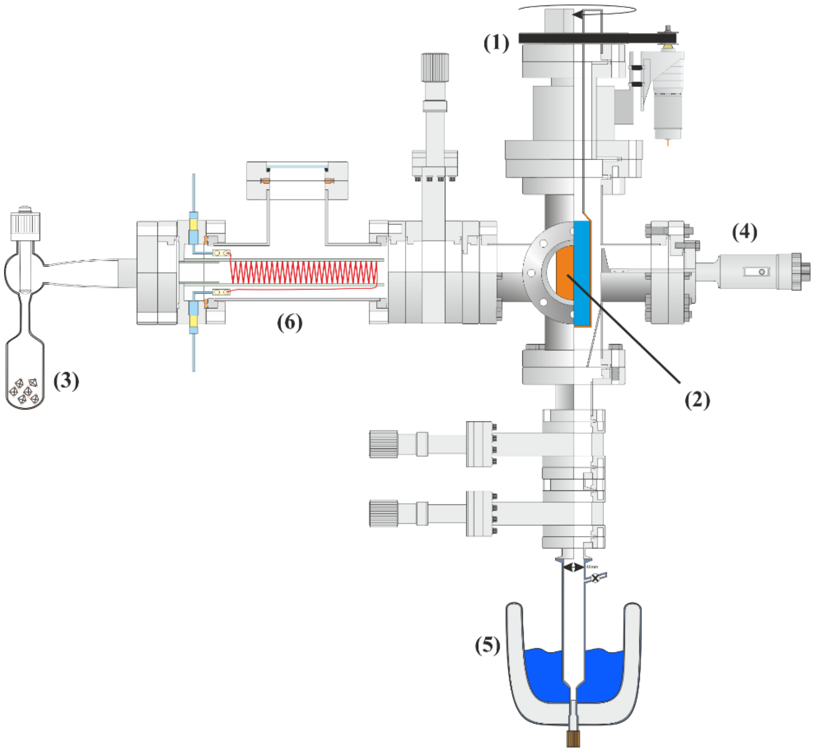

FIG. 34: Gram scale co-condensation apparatus equipped with the transfer tool (5).

In a typical experiment, the recipient is evacuated by a turbomolecular pump and heated up to 120°C overnight for desorption. After cooling down to room temperature, the cold tip (2) is rotated with 5 rpm by a drive belt of an external motor and then cooled with liquid nitrogen. The recipient is equipped with two orifices directed to the cold tip, which allow an independent supply with adamantane vapor (3) and the guest species respectively. The vapor pressure of adamantane at room temperature ($\approx 10^{-3}$ mbar) is sufficient for gas flow rates up to 2 $\mathrm{mmolh^{-1}}$ (272 $\mathrm{mgh^{-1}}$), which are controlled by a calibrated valve. A thin layer of adamantane (≈ 1 µm) is initially condensed to prevent reactions of the guest molecules with the copper of the cold tip. Then vapor of solid white phosphorus is co-condensed at different condensation rates in order to form different dilutions with a constant adamantane gas flow of 0.5 $\mathrm{mmolh^{-1}}$. After 7-8 h of deposition, a matrix layer of approximately 500 µm thickness and a total amount of up to 1 g is formed. The matrix layer is scratched from the cold tip with a linear manipulator comprising a PTFE tip (4) and collected in a Schlenk vessel connected to the recipient. Afterwards, the matrix samples are transferred into a 4 mm solid state NMR rotor inside a glove box. For the diffusion control experiments, a specially designed transfer tool (5), which enables cooling to 195 K under inert gas atmosphere and a subsequent cooled transfer into a precooled MAS NMR spectrometer, was used. Detailed description is provided in the Supporting Information. The layers of matrix-isolated P_4/P_2 were prepared in the same manner, with the phosphorus gas being passed over a tantalum filament (6) heated up to approximately 1200°C.

4.2.2 Raman Matrix Spectroscopy

The apparatus for multichannel Raman matrix isolation spectroscopy and the general procedure are described elsewhere. [43] White phosphorus (Merck, 99.6%) was purified by sublimation. Adamantane (ABCR, 99.8%) was mixed with P_4O_{10} for removing any residue moisture and then purified by vacuum sublimation. The layers of matrix-isolated P_4 were prepared by co-condensation of vapor of white phosphorus cooled down to –30 °C and adamantane vapor generated by sublimation at +20 °C. Both components were mixed in front of the cold surface (77 K) of the cryostat. The evaporation conditions of P_4 for a dilution ratio of 1:1000 were elaborated by comparison of P_4 lines with the ν ($^{14}N^{15}N$) line in nitrogen matrices, as previously described, [126] and the flow rate of adamantane vapor was adjusted to these conditions. The resultant matrix layer had a thickness of up to 100 µm. For the Raman measurement, the matrix was cooled to 15 K. The following annealing procedures were carried out by heating the layer to 77 K, 150 K and 293 K, respectively over a period of 10 min. Subsequently, the temperature of the matrix was again reduced to 15 K for the measurement. The layers of matrix-isolated P_4/P_2 were prepared in the same manner, with the phosphorus vapor being passed through a tantalum filament heated to ≈ 1200°C. The reproduced Raman spectra are recorded with a resolution of 0.6 cm^{-1} and an accuracy of ±0.3 cm^{-1} compared to the excitation line of the Ar^+-laser at 514.5 nm.

4.2.3 MAS NMR Spectroscopy at Room Temperature

The solid state ^{31}P MAS (10 kHz) NMR spectrum of P_4 in the adamantane matrix (FIG. 35) reveals two singlets at -540.9 ppm ($\omega_{1/2}$ = 21.6 Hz) **(1)** and at -461.5 ppm ($\omega_{1/2'}$= 79.4 Hz) **(2)**. In the following chapters these signals will be referred to as signal **(1)** and signal **(2)**. Signal **(1)** is identified as a P_4 tetrahedron isolated in adamantane. Signal **(2)** is identified as an agglomeration of white phosphorus. No oxidation products were detected. Signal **(2)** is only observed at low dilutions. Considering the detected chemical shifts and narrow half-line band widths, the P_4 tetrahedra seem to be intact in both cases.

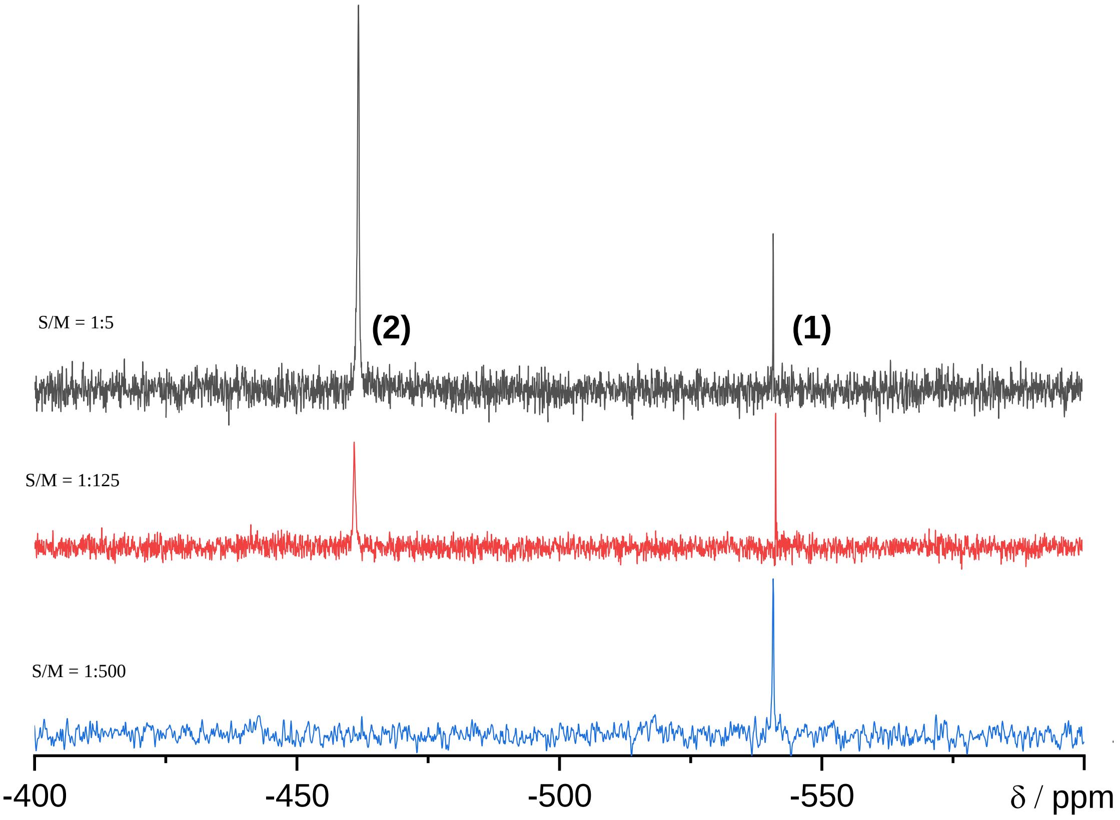

FIG. 35: ^{31}P MAS (10 kHz) NMR spectra of P_4 in the adamantane framework at room temperature at different dilutions, showing signals **(1)** for the isolated trapping site on the right and **(2)** for the agglomerated trapping site on the left.

Signal **(1)** is shifted upfield compared to white phosphorus as a solid (–462 ppm), a liquid (–460 ppm) or dissolved in benzene (–522 ppm). [133-136] Other P_4 molecules encapsulated in porous materials or cages resonate between approximately –490 and –528 ppm. [127, 129, 130, 132, 137, 138] Compared to gaseous P_4 (–551.5 ppm), signal **(1)** is shifted downfield by 10.6 ppm. However, to our knowledge, it shows the highest similarity of all other P_4 species to the gas phase value. [139] (see TABLE 26) As a result, it can be concluded that the interactions of white phosphorus **(1)** with the environment are weaker than in other known compounds or composites.

TABLE 26: Summary of ^{31}P NMR shifts of phosphorus.

Phosphorus Allotropes	δ ^{31}P [ppm] exp.
P_4 isolated in adamantane (1)[a]	–540.9
P_4 (g)[139]	–551.5
P_4 aggregated in adamantane (2)[a]	–461.9
P_4 (l)[139]	–460.0
P_4 (solution in $(CD_3)_2CO$)[140]	–527
P_4 in $[P_{6\,6\,6\,1\,4}][NTf_2]$ [141]	–520.6
Solid Red Phosphorus [142-144]	65-50
Red Phosphorus in $[P_{6\,6\,6\,1\,4}][NTf_2]$ [141]	–454.3
Hittorf`s Phosphorus [145]	–84.5 - 171.3
Black Phosphorus [146]	22.2

[a] Values derived from this study.

This hypothesis is supported by the very narrow half-line width (22 Hz) of **(1)** at a MAS frequency of 10 kHz, indicating a higher grade of rotational freedom of the P_4 tetrahedron inside the adamantane matrix than it would be expected in a solid sample. The compound most suitable for comparison to our knowledge is $(P_4)_2C_{60}$ resonating at -490 ppm with a half-line band width of 55 Hz, which still is twice as broad. [132]

Without MAS, the $\omega_{1/2}$ of signal **2** is 537 Hz. The half-line band width of comparable compounds like the one recently published by *Scheer* show a $\omega_{1/2}$ of 1582 Hz. [130] Therefore a very high degree of rotational freedom is expected for the P_4 molecule isolated in adamantane. At dilutions lower than S/M 1/500, signal **(2)** assigned to not aggregated phosphorus is detected. It gains intensity with the amount of phosphorus deposited on the cold tip. Signal **(2)** cannot be excited by cross polarization (FIG. 36), which proves the absence of hydrogen atoms associated with adamantane molecules located close to the phosphorus atoms, as no dipolar coupling exists. We propose that the chemical environment may be compared to liquid white phosphorus, observed at a chemical shift of –460 ppm, which indicates a similar shielding. [136] Dissolved phosphorus tetrahedra are shifted upfield. This shift differs from the peak representing the aggregated species **(2)** by 1.5 ppm. [139] The difference of the peak between the isolated species **(1)** and gaseous phosphorus is 10.6 ppm, which can be explained by the fact that the isolated species is enclosed by adamantane, whereas the aggregated species is mostly surrounded by other phosphorus atoms.

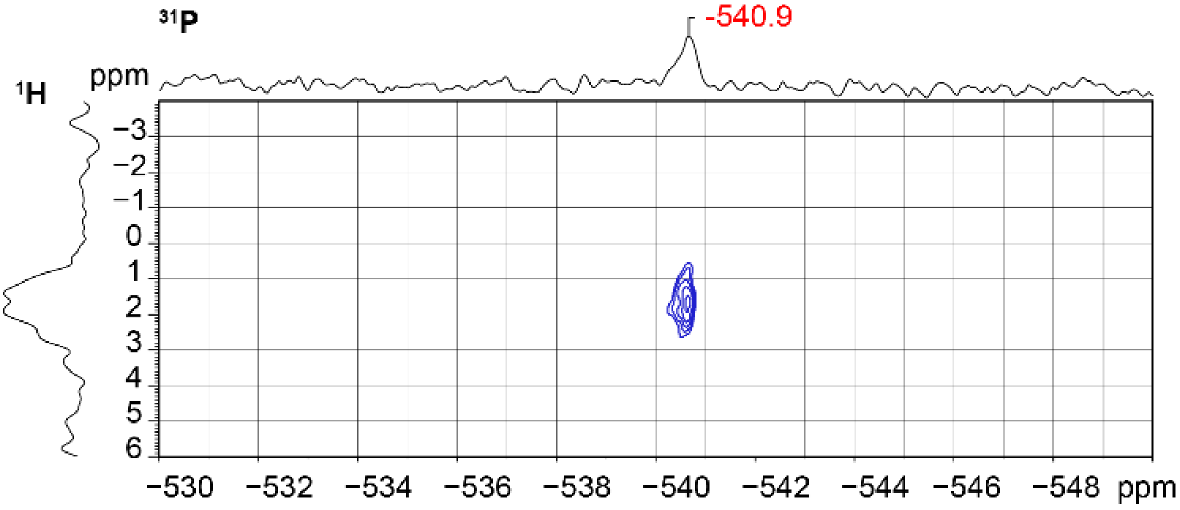

FIG. 36: ^{31}P cross polarization (CP) NMR spectrum of white phosphorus in adamantane at 10 kHz. The signal at −461.5 is no longer observable and the signal at −540.9 is excited by the ^1H channel.

4.2.4 MAS NMR Spectroscopy at Low Temperature

As mentioned previously, the half-line band width of the signals is notably small for a solid state NMR experiment. The signal of the aggregation **(2)** exhibits a half-line width of 79 Hz, which already is very narrow. However, the signal of the isolated molecule (22 Hz) is more than three times sharper. This indicates that only very weak interactions are existent. Due to the observed high isotropy, it cannot be excluded that the phosphorus molecules spin around their own axes and boost their isotropy. In order to investigate the root cause for the narrow signals, the experiment with a S/M ratio of 1/125 was performed at different temperatures starting at room temperature and decreasing it to 180 K.

Comparing the $\omega_{1/2}$ of the signals in the spectra (FIG. 37) at different temperatures, a strong rise of $\omega_{1/2}$ for the signal of the aggregated phosphorus at 200 K is observed, resulting in a splitting into three signals. Thus, the signal of the aggregated phosphorus **(2)** consists of at least three distinguishable chemical environments. Considering this spontaneous rise of the line width, the phase transition of adamantane at 208 K must be responsible for this behavior. [147-149] At temperatures higher than 208 K, adamantane crystallizes in its α-modification and is able to spin at its own lattice site. [150] Therefore, the environment of the species encapsulated in the adamantane bulk is dynamic and the anisotropy of the signals is lowered. Consequently, only with the dynamics of the host, all the phosphorus species forming the signal are chemically equivalent. The phase transition of α-phosphorus to β-phosphorus at 196 K, which is associated with the freeze of the rotation of the phosphorus atom around its lattice site, is rather unlikely to be responsible for the observed signal broadening as it already occurs at significantly higher temperatures. [151] In contrast to a solid P_4 (−405±10 ppm) [152], only short range order and no long range order seems to be existent. This is comparable to the situation of frozen liquid P_4 (−460 ppm). [139]

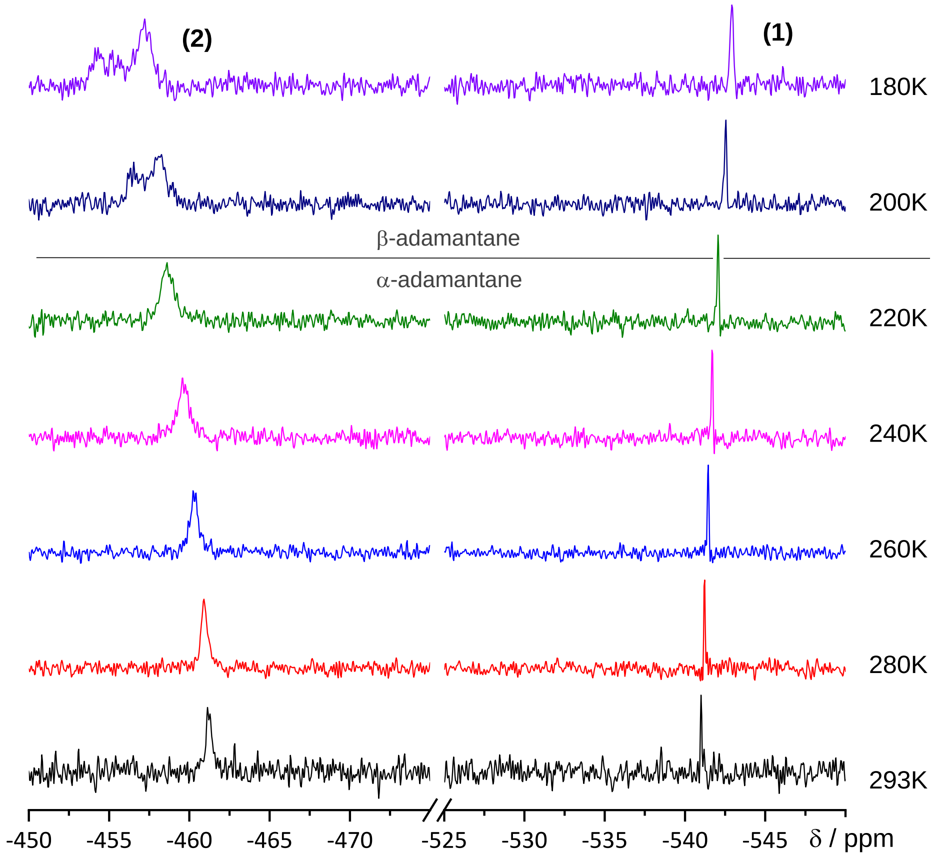

FIG. 37: ^{31}P NMR spectra of white phosphorus in adamantane at different temperatures and 4 kHz. The signal at −461.5 ppm is caused by an aggregation of P_4 molecules in the adamantane environment and the signal at −540.9 ppm is caused by its isolated equivalent

The signal of the isolated phosphorus molecule **(1)** is less affected by temperature. Therefore, it can be concluded that all isolated P_4 tetrahedra must be trapped in a chemically equivalent trapping site. Consequently, no influence of the phosphorus phase transition can be recognized either. The half-line width increases from 22 Hz at 293 K to 51 Hz at 180 K. The half-line width of the other signal raises from 79 Hz at 293 K to 171 Hz at 220 K. Due to the minor changes to signal **(1)**, it seems reasonable to assume that it was not possible to freeze the self-rotation of the isolated phosphorus tetrahedra. Thus, there is only a negligible influence of the dynamic environment and adamantane phase transition on the isolated phosphorus tetrahedron. The half-line widths ($\omega_{1/2}$) are summarized in TABLE 27. Furthermore, the shift of the peaks is temperature dependent. The agglomeration is shifted downfield, whilst the signal of isolated P_4 shifts upfield.

TABLE 27: Half-line width of $\omega_{1/2}$ (1) and $\omega_{1/2}$ (2) in Hz and chemical shift in ppm at different temperatures and a MAS speed of 4 kHz.

Temperature [K]	$\omega_{1/2}$ (1)	Chem. Shift **(1)**	$\omega_{1/2}$ (2)	Chem. Shift **(2)**
293	21.6	−461.1	79.4	−541.0
280	21.5	−460.9	99.9	−541.2
260	23.3	−460.2	107.2	−541.5
240	24.7	−459.5	135.9	−541.7
220	26	−458.6	170.8	−542.1
200	30.2	−458.3	367.8	−542.6
180	50.6	−455.2	354.4	−542.9

4.2.5 Diffusion of P_4 inside the Matrix

In order to investigate if the interactions between phosphorus and adamantane are weak enough to allow diffusion of P_4 through the matrix material, experiments to monitor such a movement were conducted. P_4 in solid adamantane was prepared, employing a persistent cooling chain and the sample was inserted in a precooled NMR spectrometer. In order to pack a precooled NMR rotor and transport the sample to the precooled NMR spectrometer a novel transport packing vessel was designed, enabling a consistent temperature of –78°C in the sample. This vessel is further described in the Supporting Information. Inside the spectrometer, the temperature of the sample was then raised from 220 K to room temperature.

If the transfer of a matrix with the S/M dilution of 1/125 from the matrix apparatus into the NMR rotor is performed under controlled conditions, as described above, at 220 K only the isolated species **(1)** and no agglomerated phosphorus **(2)** is detected. This contrasts with the observations made at room temperature, where signal **(2)** can be detected at comparable dilutions. The probability of isolation at single site isolation at a M/S ratio of 100 is only 88.6 %. [4] In the present experiment, the isolation of P_4 at 220 K is almost quantitative. This is a remarkable difference, because of the chemical shift and the narrow signal, the P_4 tetrahedra are intact and trapped in chemically equivalent trapping sites.

At 220 K the adamantane matrix must be rigid enough to prevent the diffusion of isolated P_4 molecules until a temperature of 260 K is reached.(FIG. 38) At 260 K the P_4 molecules leave their chemically equivalent trapping sites, diffuse through the host material and form an agglomeration **(2)**, again observed at about –460 ppm. This observation is not dependent on the phase transition of adamantane, which was described above. Above a temperature of 260 K, the host-guest interactions are already too weak to keep at least some of the tetrahedra in their trapping site.

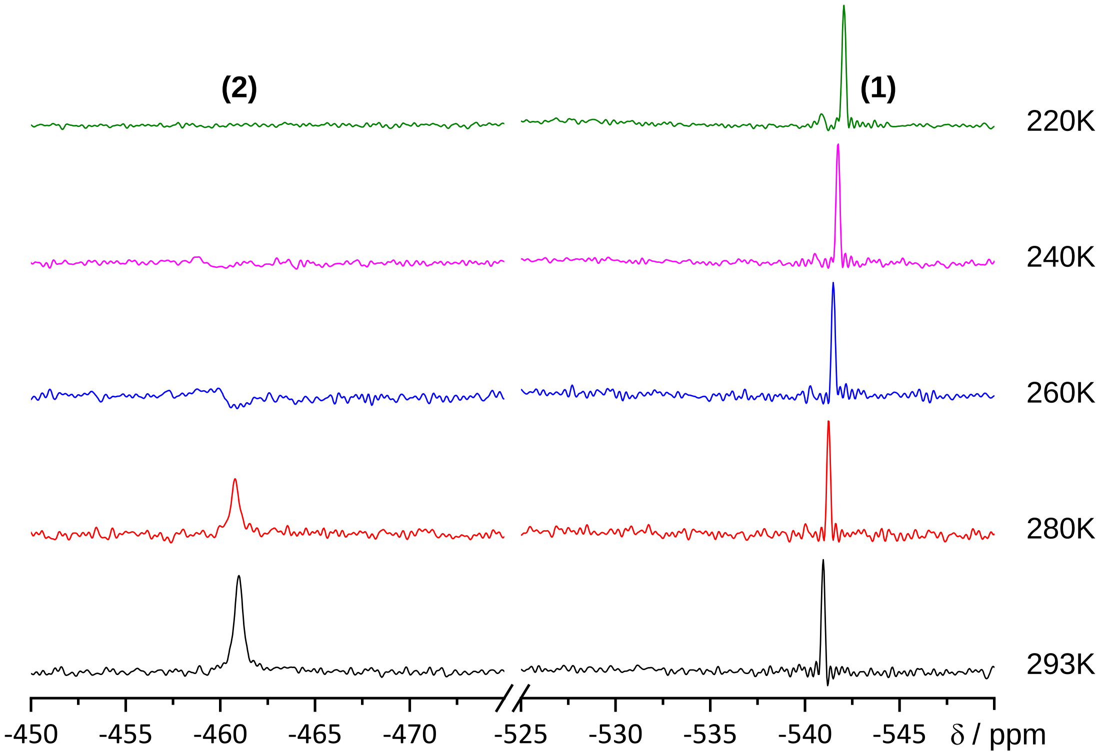

FIG. 38: NMR spectra of white phosphorus in adamantane at different temperatures and 4 kHz. The signal at −461.5 ppm is caused by an aggregation P_4 molecules and the signal at –540.9 ppm is caused by its isolated equivalent.

4.2.6 Raman Matrix Spectroscopy of P_4 and P_2 inside Adamantane Matrices

In previous matrix isolation studies P_4 and even P_2 were trapped in noble gas matrices. [126] In order to estimate if the unstable diphosphorus can be trapped with the gram scale apparatus, we decided to reinvestigate Raman matrix isolation experiments employing adamantane as matrix material. The experimental conditions were kept as similar as possible to those of the NMR experiment.

A mixture of P_4 and P_2 was generated by passing P_4 over a tantalum filament heated to 1200 °C. For the Raman experiments the isolation of P_4 and a mixture of P_2 and P_4 in adamantane is carried out at 77 K in order to form a mixture of P_4 and P_2. For the subsequent Raman measurements, the cold tip was cooled to 15 K. Measurements over 77 K showed an evaporation of the matrix by the laser.

The isolation of P_4/P_2 in the adamantane host at 77K was successful. P_2 and P_4 are the only species that are observed in the adamantane matrix. Although P_2 and P_4 were trapped as a mixture in the adamantane matrix, the Raman spectra are in good agreement with the literature. [126] The Raman spectrum of adamantane is not influenced by embedded guest molecules. All vibrational frequencies are summarized in TABLE 28. The Raman matrix spectra at different temperatures are shown in FIG. 39 together with a spectrum of adamantane.

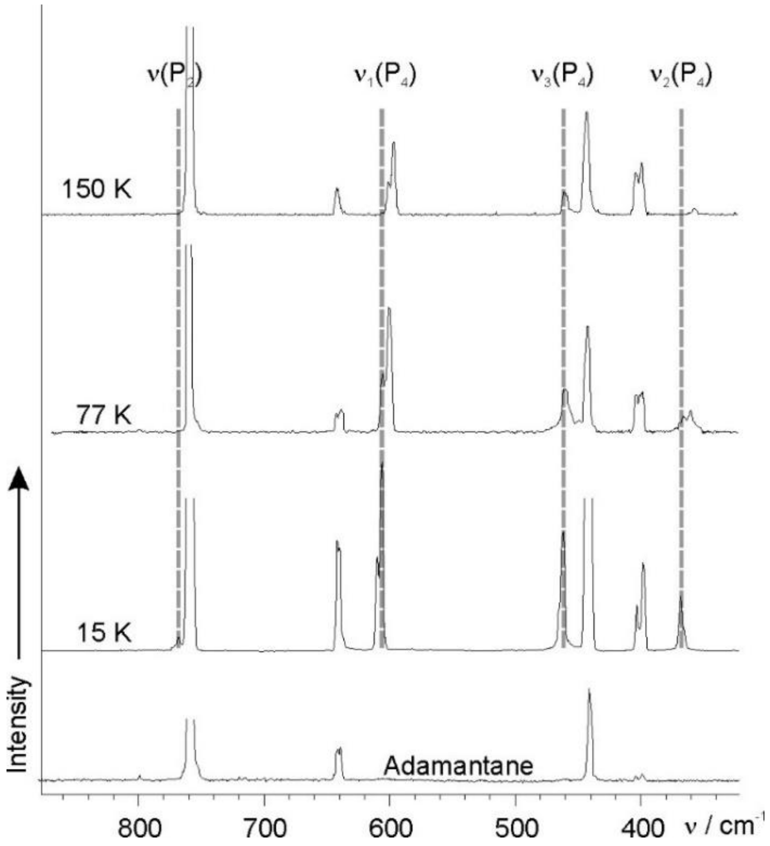

FIG. 39: Matrix isolation Raman spectra of P_4/P_2 trapped in adamantane at different temperatures.

TABLE 28: Raman frequencies (cm^{-1}) and relative intensities (in brackets) of P_4 isolated in argon, xenon [126] and adamantane matrices. Raman intensities are listed in $Å^4/u$.

Assignment		In Ar at [126]		In Xe at [126]		In adamantane at			
		15 K		15 K		15 K		77 K	150 K
$\nu_1(P_4)$	*A1*	613.6	(100)	611.4 617.1	(100)	606.4 609.7	(100)	600.0 604.5	597.5 601.0
$\nu_2(P_4)$	*E*	371.8	(44)	369.9 371.5	(46)	366.6 368.7	(42)	359.5 364.4	358.3
$\nu_3(P_4)$	*F2*	467.3	(109)	465.6 469.6	(109)	462.4 464.8	(88)	461.2	457.6
ν (P_2)		773.6		770.9 774.6		767.5		-	-

If the measurement is carried out at 77 K, annealing cycles towards higher temperatures are possible. Above 250 K, a pressure increase in the apparatus is observed, caused by the slow sublimation of the adamantane host. Due to the isolation vacuum in the matrix apparatus, the P_4/P_2 in the adamantane solid is only stable for a short time at room temperature. This effect can be reduced by venting the apparatus with inert gas and adamantane vapor. The annealing cycles do not lead to the formation of other molecules beside P_4, but the P-P valence mode of P_2 is already not detectable at 77 K. Annealing at 150 K for several hours amplifies the splitting of the Raman line, but still no additional species are formed.

The NMR experiments presented earlier indicate the presence of agglomerations and isolations of P_4 inside the adamantane. These agglomerations are likely to form by the diffusion of P_4 through the matrix and the subsequent agglomeration process. Therefore, we conclude that the splitting is caused by the morphological differences of an isolated white phosphorus tetrahedron and an agglomeration of P_4 molecules. Long annealing cycles (10 h) in the vented apparatus at 300 K lead to a massive loss of signal intensity, due to sublimation of the matrix or the reaction of the diphosphorus to a less Raman active phosphorus species. Therefore, P_2 either again forms P_4 or a product, which is not detectable by Raman spectroscopy.

4.2.7 NMR Spectroscopy of the P_2/P_4 Mixture in Adamantane

In order to investigate which species are formed from P_2, the condensation of a P_2/P_4 mixture was generated analogously to the Raman experiments and investigated with ^{31}P NMR spectroscopy. (FIG. 40).

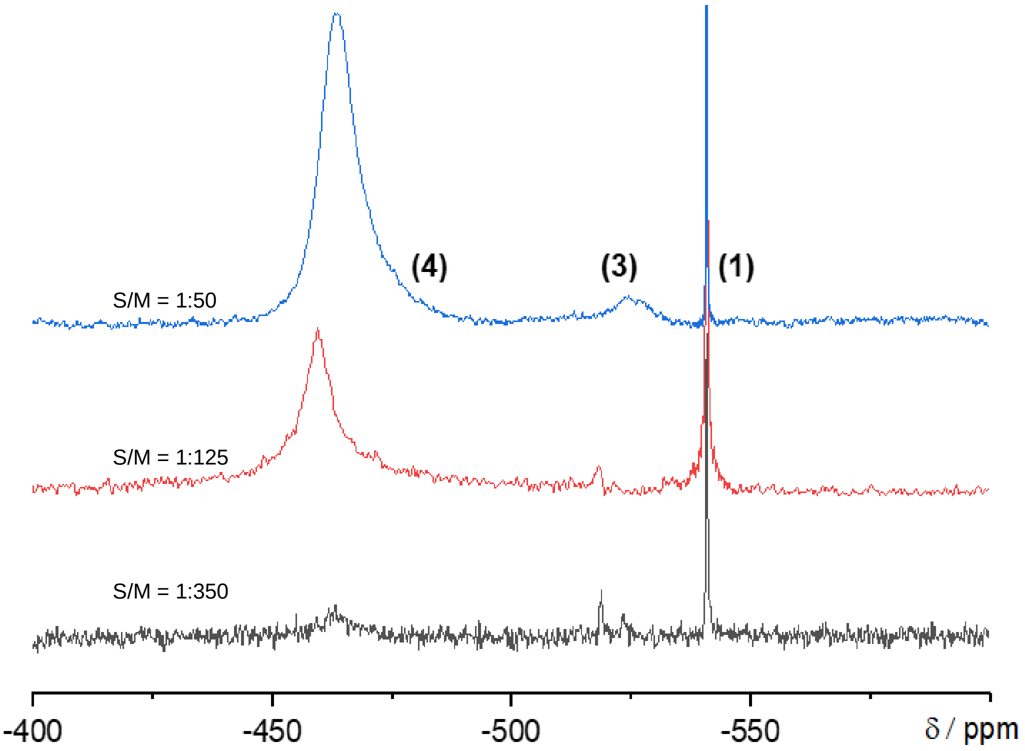

FIG. 40: NMR spectra of thermolyzed white phosphorus in adamantane at different S/M ratios and 4 kHz. The signal **(4)** is caused by red phosphorus and the signal at –540.9 ppm is caused by isolated P_4.

Some of the P_4 tetrahedra seem to remain intact and are assigned to signal **(1)**. Agglomerated phosphorus **(2)** is not detectable. Thus, only isolated white phosphorus molecules are persistent under these conditions or signal **(2)** is super positioned with signal **(4)**. Thermolyzed non-isolated P_4 exhibits signals **(3)** and **(4)**. At high dilutions, a discrete signal

(3) at –518 ppm is observed. It loses sharpness and shifts downfield at lower dilutions. The chemical shift is a strong indication for the intact tetrahedral geometry of the represented molecules. A possible explanation for the observation of the signal is the formation of a white phosphorus metal complex by reaction of P_4 with the most volatile impurity of the tantalum filament. The filament contains up to 50 ppm of nickel, being the most volatile of all listed residue metals. The $Ag(P_4)_2^+$ cation, for example, is known to exhibit a ^{31}P MAS NMR signal at −511 ppm. [153, 154] Quantum chemical calculations find a true minimum for a tetrahedral $Ni(P_4)_2$ complex with a calculated chemical shift of –501 ppm. Further explanations are given in the Supporting Information. Another possibility is the formation of not completely aggregated parts of red phosphorus. The higher isotropy at higher dilutions, which is an indication for smaller and thus more mobile species, supports this hypothesis. Moving to lower dilutions, the signal broadens and a new broad signal **(4)** gains intensity at –461 ppm. This signal is in good agreement with that of red phosphorus diluted in the ionic liquid $[P_{6\,6\,6\,1\,4}][NTf_2]$ at –454.3 ppm. This is also supported by the observed reddish color of the sample at room temperature. [141] Solid red phosphorus or black phosphorus are not detectable in the ^{31}P NMR spectrum at their known chemical shifts of 50 or 22 ppm respectively. [142-144, 146]

Comparable to the experiments concerning P_4 trapped in adamantane, the agglomerated phosphorus **(2)** and **(4)** are recorded in a state comparable to a frozen liquid. As the generation of red phosphorus must be a consequence of the formation of diphosphorus and its reaction with white phosphorus, we assume that the decline of the Raman signal of P_2 in our experiment is due to the formation of red phosphorus. As a result, we can conclude that P_2 shows even fewer interactions with adamantane as P_4 and is able to diffuse through the matrix material in order to form amorphous red phosphorus.

4.2.8 NMR Spectroscopy of P_2

Repetitions of the experiments comprising the P_4/P_2 mixture with considerably higher concentrations of phosphorus vapor exhibit a signal at 729 ppm in the ^{31}P spectrum. NMR signals of red phosphorus, phosphorus oxides at around 0 ppm and a broad signal (31 ppm) of solid black phosphorus are detected (FIG. 41). [146] The NMR measurements were conducted at room temperature. This new downfield signal at 729 ppm is in satisfying agreement with the calculated chemical shift of diphosphorus (703 ppm). Information concerning the calculation is given in the theoretical section below.

The signal of P_2 exhibits a half-line band width of 55 Hz, which is twice as broad as the signal of isolated white phosphorus. Therefore, P_2 seems to be less rotationally free than P_4 in adamantane, either because of its linear shape or the large amount of red phosphorus and phosphorus oxides in the matrix. Given the fact that the signal could not be detected at lower dilutions, we assume that P_2 can only be stabilized by red phosphorus or phosphorus oxides. The various phosphorus compounds interact much stronger with each other than with the adamantane matrix. Therefore, we can state that in the present case, P_2 is not isolated by adamantane in a classical matrix isolation way. Nevertheless, the half-line band width still is remarkably narrow for a solid sample, meaning P_2 still can spin around its own axis at an enormous speed. It remains an unsettled question, if diphosphorus can be isolated in a classic manner in a less interacting environment such as adamantane at room temperature and further experiments will have to be conducted in order to identify a matrix host that is able to form the required interactions for isolating P_2 at room temperature.

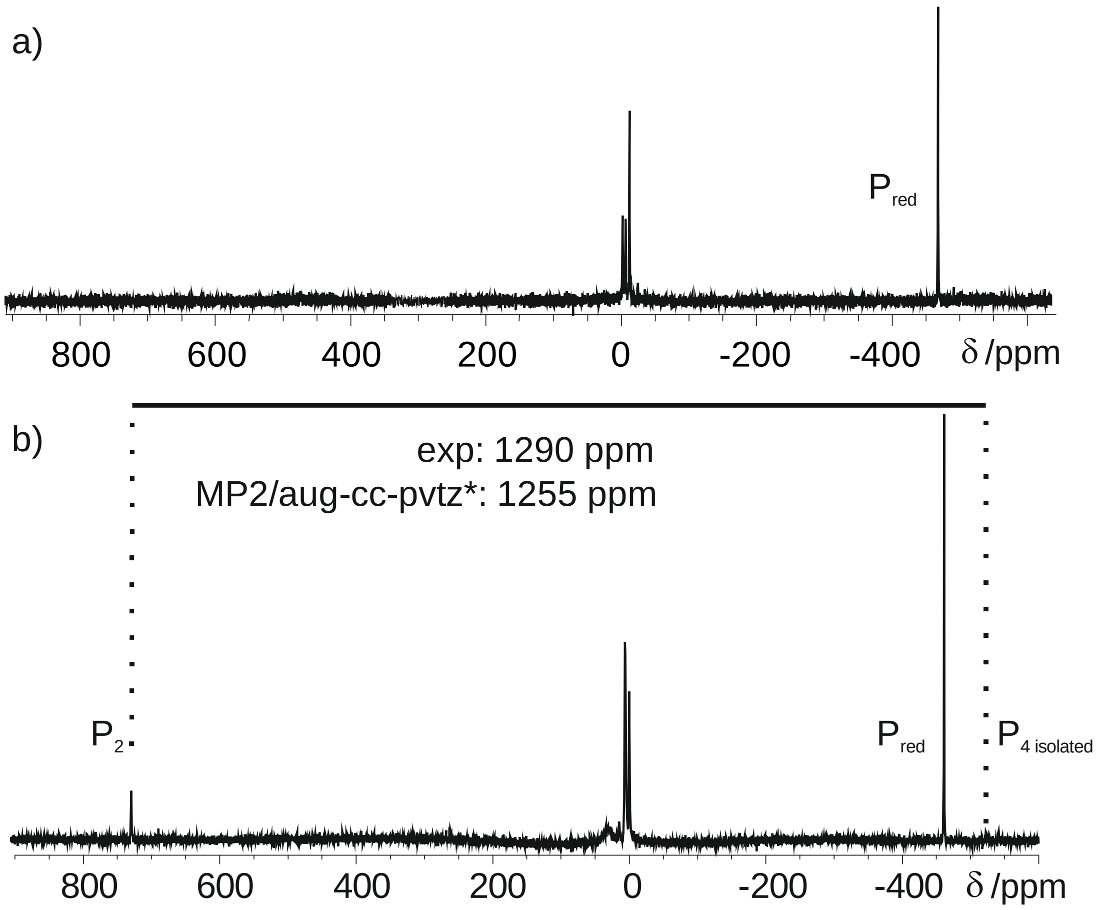

FIG. 41: (a) ^{31}P MAS NMR spectrum of red phosphorus in adamantane at low dilutions. (b) ^{31}P MAS NMR spectrum of red phosphorus and diphosphorus in an adamantane - red phosphorus mixture at 4 kHz. All spectra are recorded at room temperature.

4.2.9 Theoretical Calculations

All theoretical calculations were conducted with the program package GAUSSIAN 09, Revision B.01. [62] Considering the different sizes of models calculated in this work, varying models of theory were employed. The used methods are specified in the subchapters. The absolute shielding of the herein presented molecules were scaled with respect to the experimental chemical shift of gaseous white phosphorus, as it was determined by *Heckman* in 1972. [139]

4.2.9.1 Chemical Shift of Tetraphosphorus in the Gas Phase

In order to calculate the chemical shift of P_4, optimizations at the CCSD/aug-cc-pvtz level of theory were conducted. [45-49, 56-61] The calculation of the chemical shift was carried out under consideration of the second order *Møller Plesset* perturbation theory (MP2) and the basis set aug-cc-pvtz. [50-55]

The variety of ^{31}P NMR shifts is very large and it is dependent on several conditions. A prominent example is the unique upfield shift of the phosphorus tetrahedron. [155] Even very small changes of the geometry are responsible for a large change of the chemical shift. Another example is the difference between gaseous and liquid white phosphorus of 90 ppm, which is quite large, given that the intramolecular changes are obviously rather small. [139] Even higher differences are to be expected when changing the bonding situation. Known compounds containing a P-P double bond exhibit a severe shift downfield in the ^{31}P NMR experiment compared to compounds containing a P-P single bond. 1,2-bis-(2,3,5-tri-*tert*-butylphenyl) diphosphene is found at an isotopic shift of 494 ppm in ^{31}P MAS NMR experiments. [156] Free diphosphorus contains a triple bond. Therefore, its NMR signal must be even more shifted downfield. This is supported by recent theoretical investigations. [157, 158]

4.2.9.2 Chemical Shift of Diphosphorus in the Gas Phase

According to our own calculations, the magnetic shielding of P_2 is –345 ppm. After scaling it to the shielding of gaseous P_4, this accounts for an experimental shielding of 703 ppm. The experimental and the calculated values differ by 26 ppm, which equals a deviation of 2 %. Taking these facts into consideration, it can be stated that the experimental and the calculated values are in satisfying agreement.

4.2.9.3 Chemical Shift of isolated White Phosphorus

For the calculations of P_4 isolated in an adamantane matrix, a model containing one P_4 tetrahedron and eight adamantane molecules was created.(FIG. 42) After optimization on the M06/cc-pvdz level of theory, a true minimum was found. The P-P bond of the white phosphorus molecule in the gas phase is 0.008 Å shorter than in our quantum chemical model of P_4 isolated in adamantane. NMR calculations were conducted on both models, employing the GIAO method, the M06 DFT method and cc-pvdz as a basis set. Scaled to the experimental NMR shift of white phosphorus, the signal of P_4 isolated in adamantane in our quantum chemical model is expected at a chemical shift of –509 ppm. This is in reasonable agreement with the experimental chemical shift of –540 ppm of P_4 in the adamantane matrix. In order to investigate the influence on the shielding contributed by the matrix environment, we calculated the shielding of P_4 in the adamantane model after the removal of the adamantane molecules, thus neglecting the influence of the adamantane matrix. This results in a chemical shift of −541 ppm. As a result, we assume that the influence of the environment on P_4 is overestimated. This is a rather reasonable assumption, considering that our model only has one coordination sphere. Therefore, no further interactions of first-sphere adamantane with the adamantane molecules in the next spheres are considered. As a result, in the calculated model, the interactions between P_4 and adamantane have to be stronger than in the NMR experiment.

The elongation of the P-P single bond, due to the interactions with the environment, is in agreement with experimental data from *Resing*, who determined the P-P bond in solid white phosphorus to be 2.24±0.03 Å long by relaxation NMR experiments. [159]

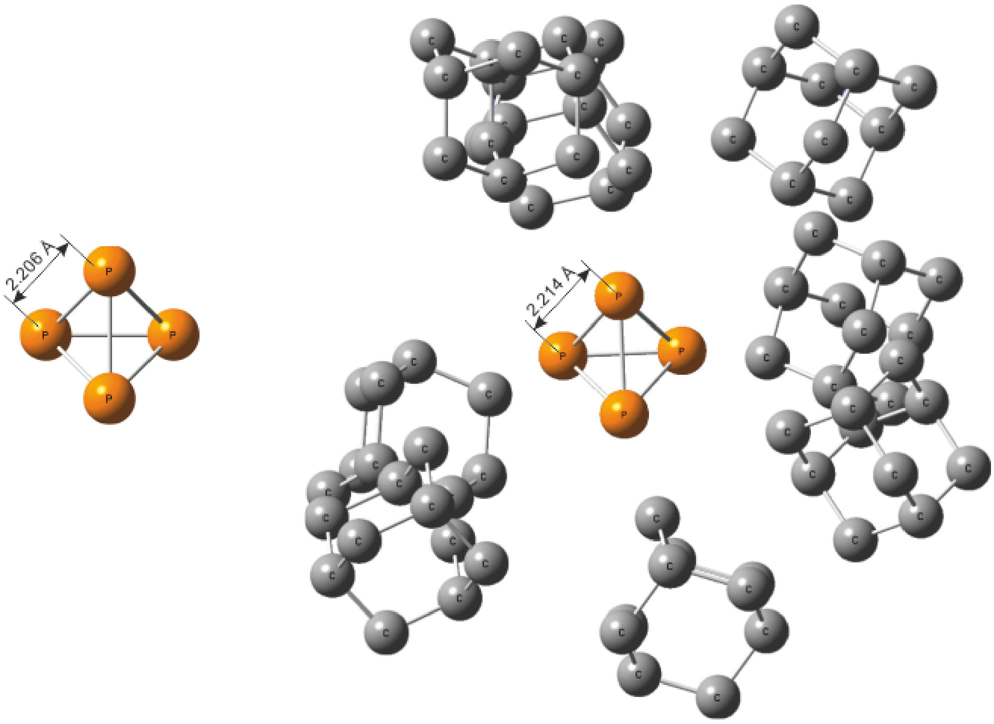

FIG. 42: Calculated structure of P_4 in the gas phase and P_4 isolated in the adamantane matrix.

4.2.9.4 Chemical Shift of agglomerated White Phosphorus inside the Adamantane Matrix

In order to model the chemical shift of liquid white phosphorus, the chemical shift of P_4 was calculated at different distances. Two different geometries are possible for such a dimer: a *gauche* conformation (I) and an *eclipsed* conformation (II). The conformations are depicted in FIG. 43. The *gauche* conformation seems to be more reasonable, as it is expected to exhibit a lower energy. Further information on the determination of the chemical shift is given in the Supporting Information. According to simulations of *Hohl* and *Jones*, the smallest intermolecular distance between two P_4 molecules in liquid phosphorus is 2.75 Å at 500 K. [160] In our calculation, the influence of the temperature is neglected. Calculations of the chemical shift of the described dimer yield a value of –486 ppm at the B3LYP/aug-cc-pvqz level of theory. This is in reasonable agreement with our experimental shift of –461.7 ppm.

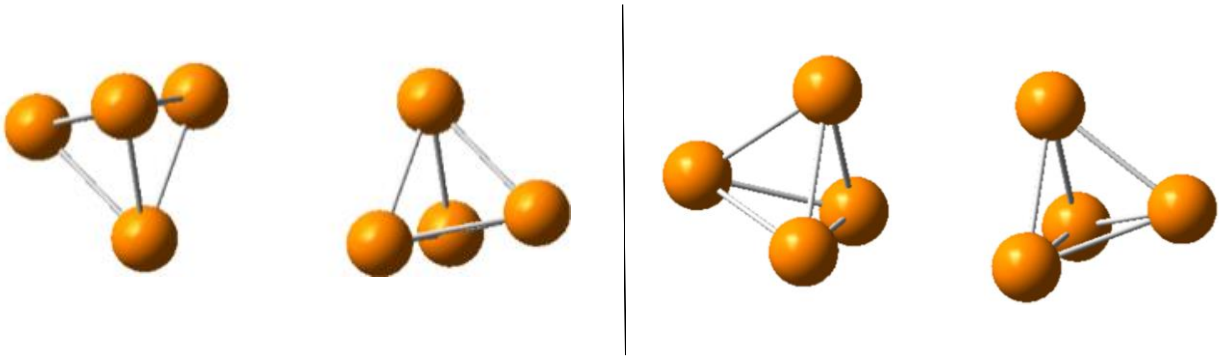

FIG. 43: Calculated ^{31}P NMR shifts of two P_4 tetrahedra in the geometry I and II. Calculations are conducted at the B3LPY/aug-cc-pvqz level of theory.

4.3 CONCLUSION

Employing our herein presented NMR matrix isolation technique, the morphology of a matrix and the interaction with its guest are described for the first time. These results enabled us to identify the reason of the splitting of the Raman spectrum of P_4 and P_2. It originates from agglomerated and isolated P_4 species. In the present study, the dynamics of P_4 in a room temperature stable matrix material was gathered by NMR experiments at low temperatures. They revealed that the mobility of agglomerated P_4 tetrahedra is mainly influenced by the host environment. The rotation of the host has no influence on isolated P_4 and its narrow signals are not affected by the chosen conditions. Above 260 K, the diffusion of white phosphorus in the host material was observed. Therefore, the ability of the host material to form interactions is even more critical than expected for the storage of white phosphorus.

SUPPORTING INFORMATION (Chapter 4)

Preoptimized P_4 tetrahedra were taken and placed at different distances according to geometry (I) and (II).

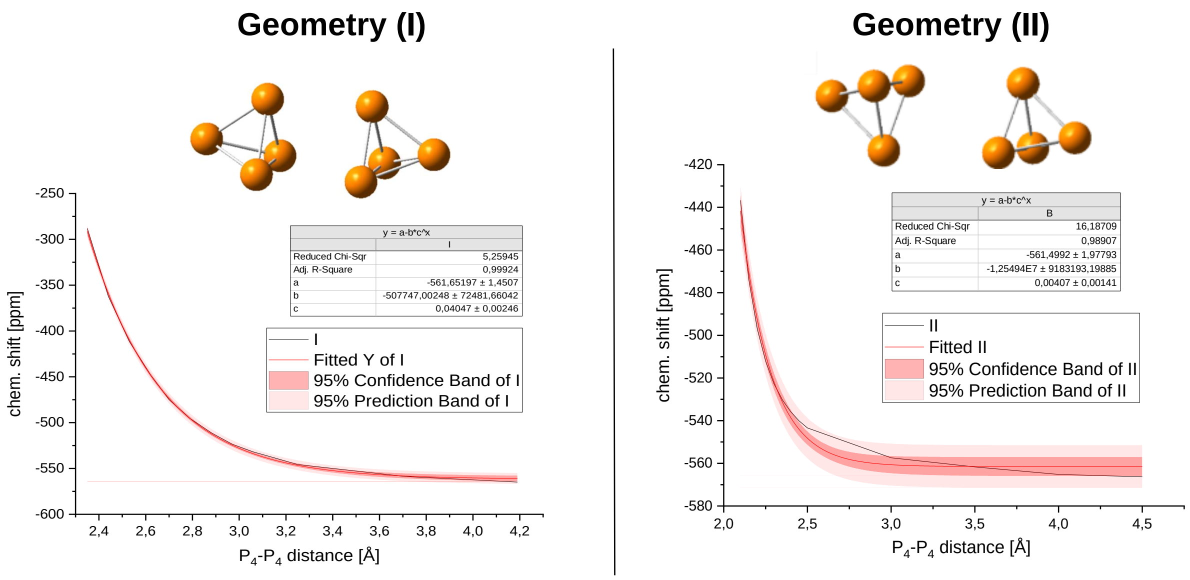

FIG S. 6: Fit of the calculated NMR shift of P_4 subject to the P_4-P_4 distance in the different geometries (**I**) and (**II**).

TABLE S 5: Calculated ^{31}P NMR shifts of two P_4 tetrahedra in the geometry **(I)** and **(II)**. Calculations are conducted at the B3LPY/aug-cc-pvqz level of theory.

Intermolecular Distance [A˚]	^{31}P NMR shift of P_4 in geometry **(I)** [ppm]	Intermolecular Distance [A˚]	^{31}P NMR shift of P_4 in geometry **(II)** [ppm]
2.35	−288.1	2.10	−436.7
2.44	−362.0	2.15	−473.9
2.53	−411.5	2.20	−496.9
2.62	−447.7	2.25	−512.1
2.70	−474.9	2.30	−522.6
2.79	−495.5	2.35	−530.2
2.88	−511.0	2.40	−535.8
2.97	−523.5	2.45	−540.1
3.06	−531.9	2.50	−543.4
3.16	−539.1	3.00	−557.4
3.25	−545.7	3.50	−561.7
3.71	−558.7	4.00	−565.2
4.19	−564.9	4.50	−566.3

The $Ni(P_4)_2$ geometry was optimized employing the M06/aug-cc-pvtz level for phosphorus and M06/MDF10 for nickel. For the NMR calculation, the GIAO method was used. The level of theory was MP2/aug-cc-pvtz for phosphorus and MP2/MDF10 for nickel. The optimized structure is given in FIG S. 7. The structure is a true minimum exhibiting no negative frequencies.

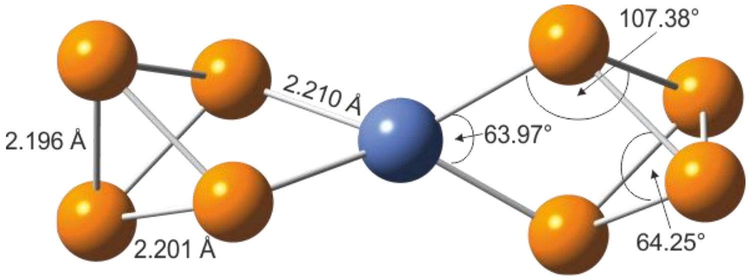

FIG S. 7: Gas phase structure of $Ni(P_4)_2$ calculated at the MP2/MDF10/aug-cc-pvtz level of theory

Cartesian coordinates of $Ni(P_4)_2$

P,	0,	-1.874361816,		0.8986380005,		-0.7499535246
P,	0,	-1.874361816,		-0.8986380005,		0.7499535246
P,	0,	1.874361816,		0.8986380005,		0.7499535246
P,	0,	1.874361816,	-	0.8986380005,		-0.7499535246
P,	0,	-3.3806343536,		0.7033828809,		0.8434036845
P,	0,	-3.3806343536,		-0.7033828809,		-0.8434036845
P,	0,	3.3806343536,	-	0.7033828809,		0.8434036845
P,	0,	3.3806343536,		0.7033828809,	-	0.8434036845
Ni	0,	0,0000000000,		0.7000000000,	-	0.0000000000

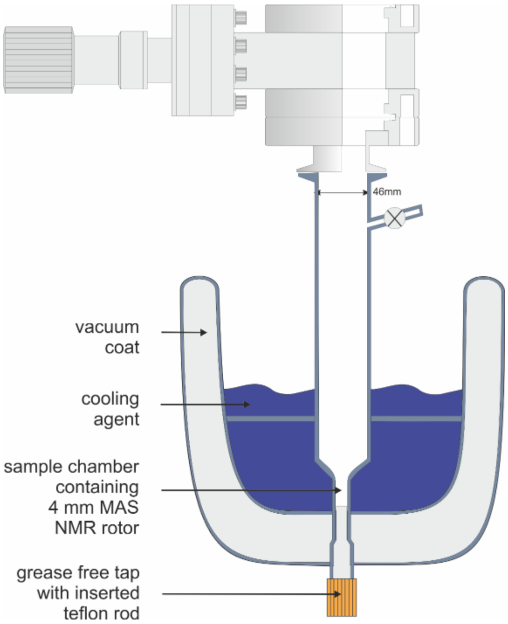

FIG S. 8: Schematic drawing of the solid state NMR handling device. The tap with rod is used to adjust the height of the NMR rotor. Precooled metal rods are used to pack the NMR rotor. The glass device is continuously flushed with argon throughout the process.

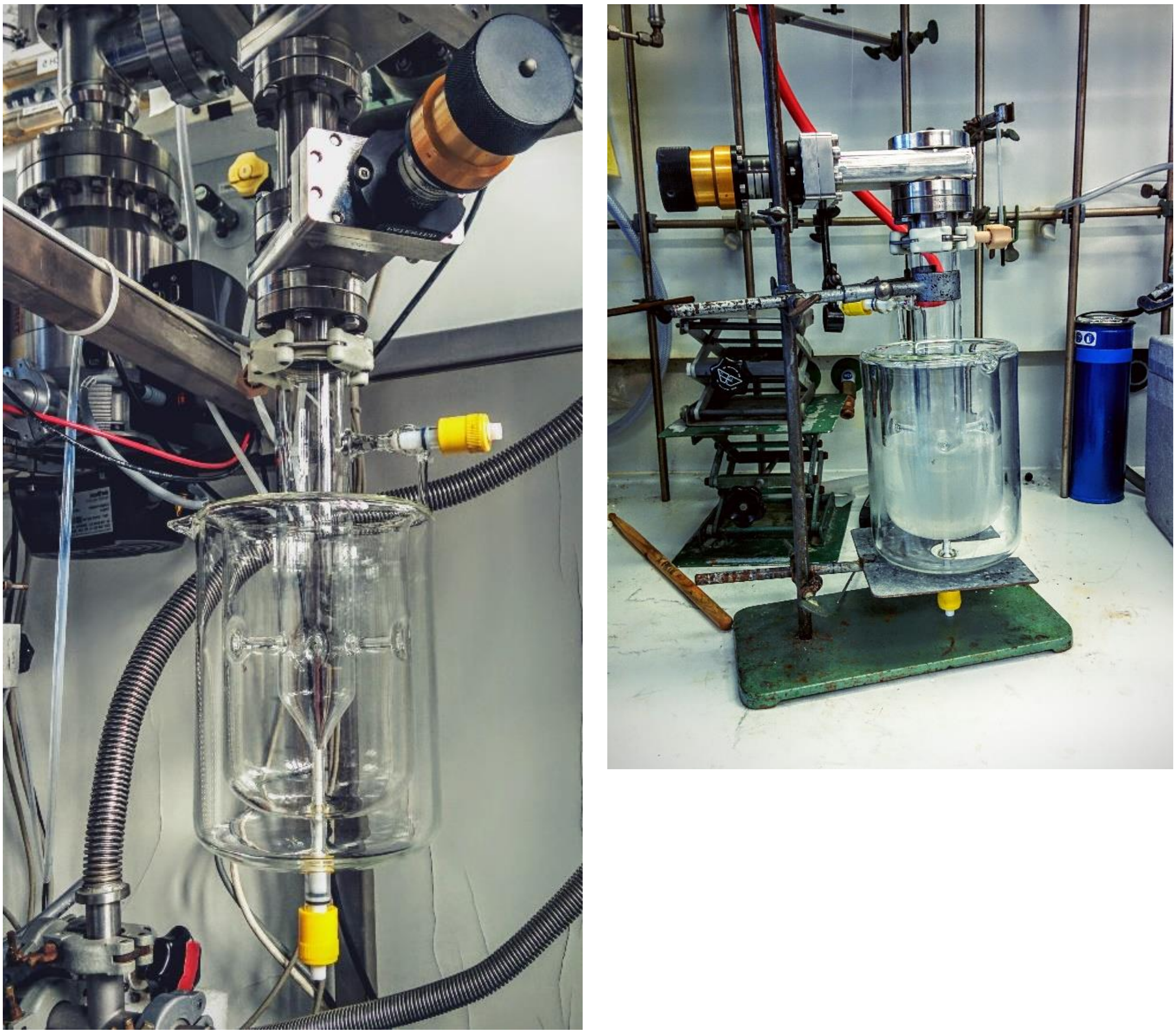

FIG S. 9: Photographs of the solid state NMR handling device. On the left side, it is attached to the co-condensation apparatus. On the right, it is attached to a stainless steel vacuum line and ready for the packing process.

5 Summary

Pnictogen Hydrides and Hydrogen Halides under Extra-Terrestrial Conditions

Mixtures of pentel hydrides and hydrogen halides have been condensed in noble gas matrices on a cold tip. The reaction products were examined with Raman spectroscopy. The formation of PH_4^+, AsH_4^+, PH_2^+, AsH_2^+ and SbH_2^+ cations has been observed. SbH_4^+ was not observed under the chosen conditions. The energetic destabilization of SbH_4^+, which is caused by hybridization effects, has been investigated by theoretical studies. The formation of the PnH_2^+ (Pn = P, As, Sb) is observed in each experiment. Their reaction pathway, which comprises a hydrogen elimination from the XH_4^+ cations (Pn = P, As, Sb) are discussed by theoretical calculations. The interactions between the XH_4^+ cation and its corresponding halide anion are discussed and the importance of the interaction’s strength for the elimination process is emphasized. The interaction of PnH_2^+ and F^- was investigated in the case of the $AsH_2^+ F^-$ ion pair by Raman spectroscopy. Depending on the S/M ratio, $AsH_2^+ F^-$ ion pairs as well as AsH_2F were observed. All together the existence of a PnH_4^+ species may be possible in the isothermal layer (160 K) of the Jovian atmosphere (90-290 km) on a very fast time scale [102], but according to the experimental data, decomposition processes by hydrogen elimination should occur.

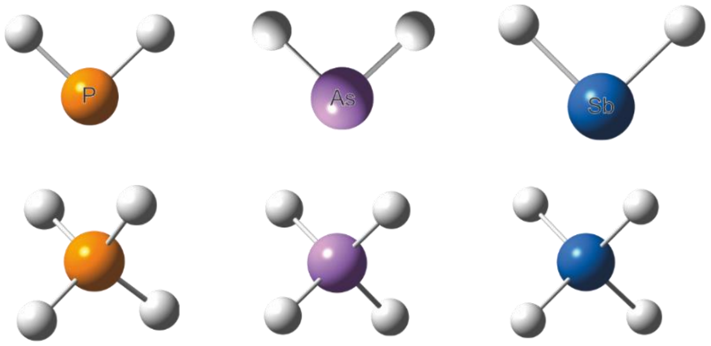

FIG. 44: Depicted molecular structures of the PnH_2^+ and PnH_4^+ (Pn = P, As, Sb) species calculated at the CCSD/aug-cc-pvtz level of theory. For the calculations of the species comprising antimony, the MWB48 ECP was employed.

Investigation on the Dimerization of AsH_2 in Noble Gas Matrices

In the course of this study, arsine was thermolyzed on a tantalum filament and a mixture of AsH_3, AsH_2 was co-condensed with argon on a helium cooled surface. At high dilutions with noble gases, AsH_2 radicals can be trapped in argon matrices and investigated by Raman spectroscopy. If higher amounts of AsH_3 are thermolyzed, the recombination of AsH_2 in the gas phase leads to the formation of As_2H_4, which was proven by Raman spectroscopy. Most prominent is the occurrence of the As-As stretching mode as a Raman line at 266 cm^{-1}. According to quantum chemical calculations, the As-As bond is 2.449 Å long and the molecular structure of the arsanyl radical is almost identical to the structure of the AsH_2^+ cation.

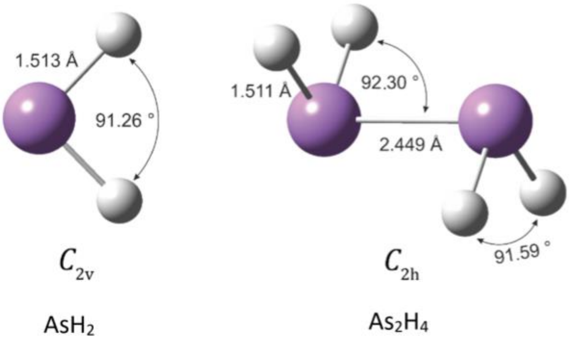

FIG. 45: Optimized structures of AsH_2 and As_2H_4 calculated at the CCSD/aug-cc-pvtz level of theory.

Spectroscopic Studies of Di- and Tetraphosphorus in Adamantane Matrices – an Approach to Room Temperature Stable Matrices.

The development of the presented matrix isolation technique enables the isolation of P_4 and P_2 in the host material adamantane. In the ^{31}P NMR spectra of the room temperature stable matrices the NMR signals of white phosphorus and diphosphorus can be observed. The ^{31}P NMR spectra show a reasonable signal to noise ratio and remarkably narrow ^{31}P NMR signals. All NMR Experiments can be performed on a conventional NMR spectrometer and no special matrix isolation NMR setup is needed. Employing this new matrix isolation technique, the morphology of the matrix and the interaction with its guest are described for the first time. These results enabled the identification of the origin for the splitting of the Raman lines of P_4 and P_2, which is caused by the existence of two P_4 species.

The method has to potential to be applied on every NMR active isotope with a sensitivity comparable to the ^{31}P isotope. In this way proximity information, for example, can be determined by employing cross polarization methods either on the species or the matrix material. Such experiments provide a deeper understanding of the morphology of matrix isolated samples. Even information on the metallic character of the trapped substrate can be accessed by the measurement of the *Knight Shift*, supplying a tool to examine the borderline between clusters and metals.

6 Experimental Part

6.1 USED CHEMICALS

All reactions and experiments in the work were carried out employing stainless steel vacuum lines and SCHLENK technique. The used chemicals are listed in TABLE 29. Nitrogen, dried by passing through a glass tube filled with Orangegel and Sicapent®, and argon 5.0 were used as protective inert gases.

TABLE 29: Chemicals used in the course of this work.

Compound	Purity	Producer
Neon	99.9 %	Messer Griesheim
Argon	99.999 %	Messer Griesheim
Xenon	99.9999 %	Messer Griesheim
Phosphine	-	In-house production
Arsine		In-house production
Stibine		In-house production
Deuterium fluoride	-	In-house production
Hydrogen fluoride	-	Linde
Hydrogen bromide	-	Fluka
Hydrogen iodide	-	In-house production
Adamantane	98.0% (sublimated)	ABCR
White phosphorus	99.9% (double sublimated)	chemPUR

6.2 SYNTHESIS OF PENTEL HYDRIDES

The handling of all PnH_3 (Pn = As, Sb) species was carried out in a stainless steel vacuum line and they were stored in Young cold traps at −196 °C under hydrogen atmosphere. Antimony or arsenic and magnesium powder heated under vacuum in a stoichiometric ratio of one to three were sintered to Mg_3Pn_2 (Pn = As, Sb) in a previously heated and evacuated glass ampoule. The Mg_3Pn_2 powder was gradually added at 0 °C in the hydrogen stream to an excess of aqueous 6 M HCl solution, whereupon the gaseous PnH_3 was condensed after passing through a cold trap (−20 °C) in a Young cold trap (−80 °C). FIG. E. 1 shows the apparatus used for synthesis of SbH_3:

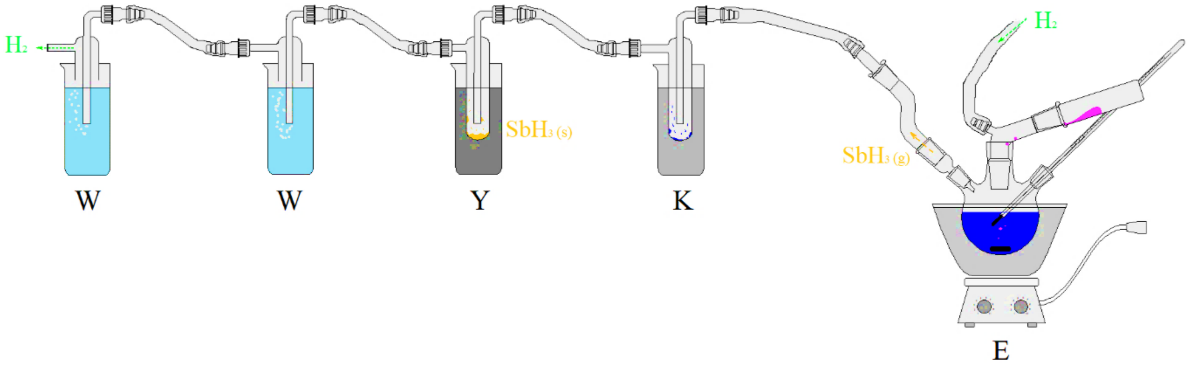

FIG. E. 1: Schematic representation of the apparatus used for the synthesis of SbH_3 with a reaction vessel in an ice water bath at 0 °C (E), a cold trap at −20 °C (K), as well as a Young cold trap at −80 °C (Y) and two wash bottles with aqueous 6 M NaOH solution (W). Color coding: Hydrogen gas in green, Mg_3Sb_2 powder in magenta, aqueous 6 M HCl solution in dark blue and SbH_3 gas or condensate in orange.

6.3 Raman Matrix Isolation Experiments

The deposition experiments are executed in an apparatus consisting of a reservoir steel cylinder, a regulation valve and a pressure sensor (MKS Baratron). This apparatus is connected to the matrix isolation apparatus. [43] Two different types of experiments, **A** and **B,** are performed. In the series of the **A** experiments, the reservoir contains a mixture of PnH_3 and HX (Pn = P, As; X = F, Br, Cl, I), which is formed by co-condensation of PnH_3 (Pn = P, As) and H/DX (X = F, Br, Cl, I) in a stainless steel gas cylinder. The hydrogen halide is used in excess of 1.1 equivalents. In the deposition process, the gas flow from the standard reservoir stainless steel cylinder is mixed with an inert gas flow at defined conditions.

Throughout the experiments **B,** the pure pnictogen hydrides are stored in the reservoir cylinder. In the deposition process, the hydrides are mixed with a hydrogen or deuterium halide, which is already diluted in the noble gas flow. For the storage of phosphine and arsine, a standard stainless steel cylinder was employed as the reservoir cylinder. For the storage of SbH_3, a glass vessel with a greaseless valve was used. In order to minimize the decomposition of stibine, the vessel was cooled to –40 °C by a cryostat. The storage vessel was merely warmed to room temperature for the extraction of stibine. This procedure allowed to use one SbH_3 batch for approximately four days of experiments. The synthesis and handling of PnH_3 (Pn = P, As, Sb) and H/DX (X = F, Br, Cl, I) was accomplished under employment of standard Schlenk technique, using a stainless steel vacuum line.

In order to detect the very small pressure changes, which are needed to achieve the high dilutions of PnH_3 (Pn = P, As, Sb) and H/DX (X = F, Br, Cl, I) mixture in the noble gas, a small container (20 ml) of the apparatus that is connected to a pressure sensor, was used as an expansion vessel. It was refilled every five minutes and the decay of the pressure was measured.

The sum of these pressure differences was used to calculate the S/M ratios. A drawing of the apparatus is shown in the supporting information (FIG S. 2). After approximately 2 h, a white homogenous layer had formed on the cold tip. Annealing cycles showed no influence on the Raman spectra until the matrix evaporation temperature was reached. After evaporation of the matrix, a metallic residue remained on the cold tip. It most likely consists of phosphorus, arsenic or antimony, depending on the used hydride.

6.3.1 RAMAN MATRIX SPECTROSCOPY

The apparatus for recording Raman matrix spectra consists of four units: a pumping station, a gas supply, a cryostat and the Raman spectrometer. (FIG. E. 2) The apparatus is described in detail by *A. Kornath* in the literature. [43] In the following, the focus is put on the improvements made for the experiments. The Raman spectra were detected with a CCD Raman spectrometer (Jobin-Yvon T64000). A frequency doubled Nd: YAG DPSS laser (Cobolt 05-01 Series Samba; 532 nm) was used as a light source with an angle of 55°.

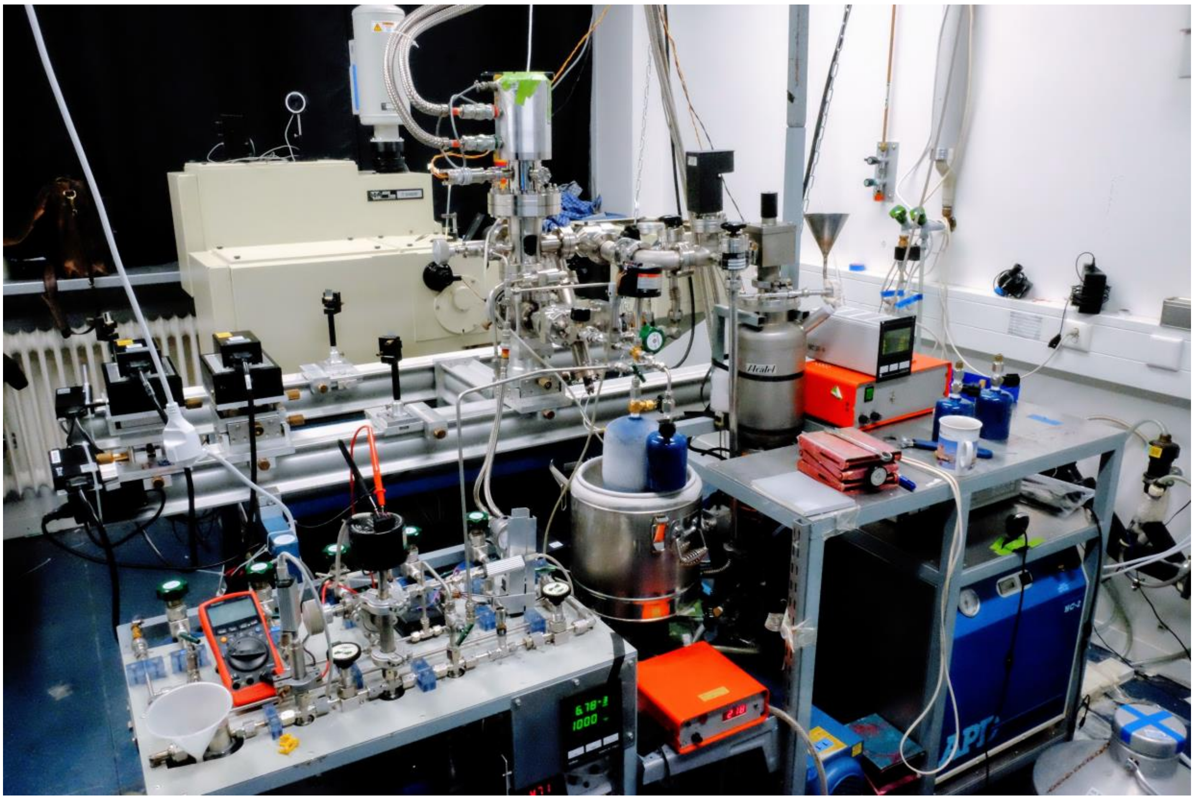

FIG. E. 2: Photography of the Raman matrix isolation apparatus.

6.3.2 Condensation of PH_3 or AsH_3

For the investigation of the reactions comprising PH_3 and AsH_3, a separate supply line was constructed for a supply reservoir, in which the pentel hydride and the desired hydrogen halide were mixed. A continuous inflow and a variable flow rate must be ensured for successful condensation of the matrix to be investigated. In addition, the use of a separate inlet for the gaseous product offers the advantage that the supply lines to the gas supply as well as to the storage vessel for the gas species can be evacuated and regulated independently. A schematic drawing of this supply line is shown in FIG. E. 3 for the condensation of AsH_3 as an example.

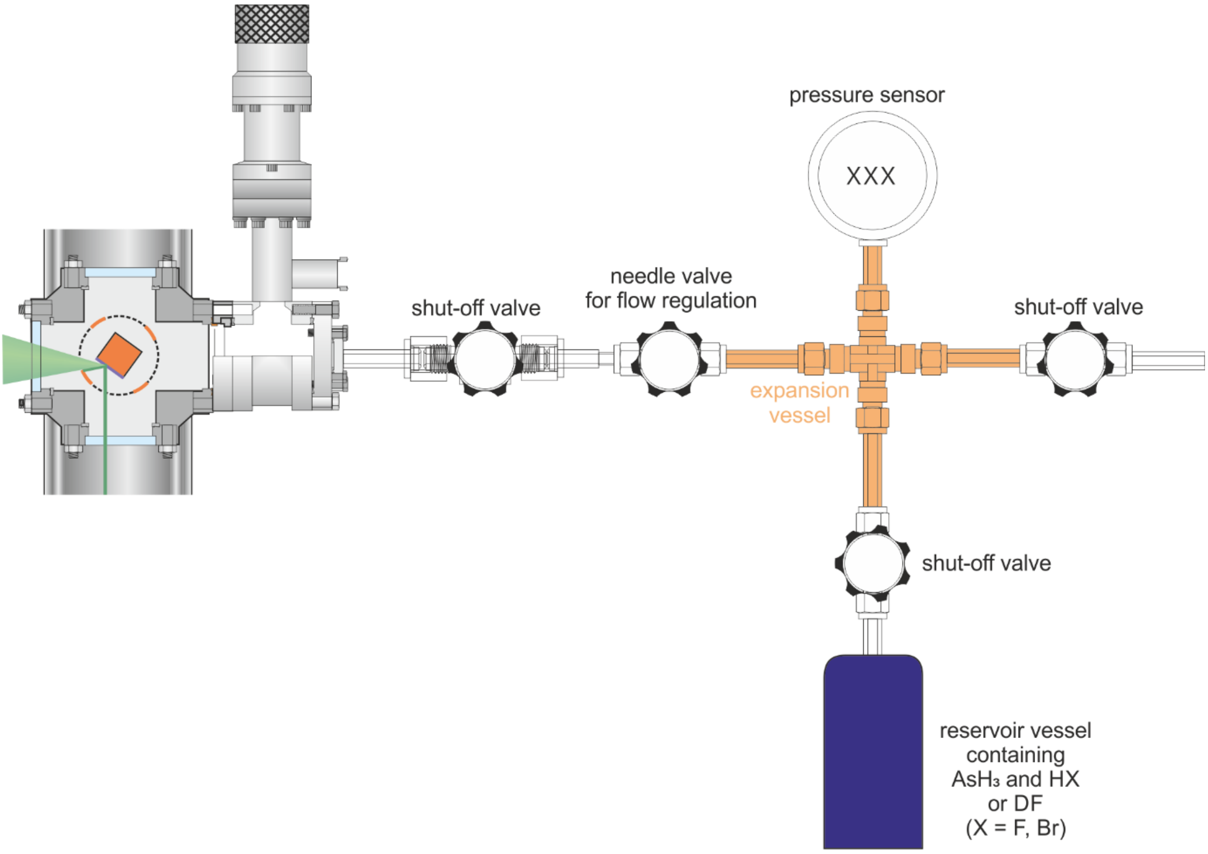

FIG. E. 3: Schematic drawing of the apparatus for the condensation of AsH_3.

The specially designed supply line consists of a shut-off valve followed by a *Swagelok* bellows metering valve (TYPE: SS-4BMG). A crosspiece is then connected to the two valves, to which the reservoir is attached by another shut-off valve, and a *MKS Baratron* manometer (TYPE: HS A-B1000SP) on the opposite side. The remaining connection of the crosspiece is connected to another shut-off valve. This bypass allows the product source to be evacuated separately from the rest of the equipment. The various components are connected *via* 6 mm steel pipes and 6 mm fittings from *Swagelok*.

6.3.3 Condensation of SbH_3

For the experiments with SbH_3, the used apparatus was varied, as the stainless steel reservoir cylinder proved to speed up the decomposition of SbH_3. In order to overcome this problem, a coolable glass vessel was employed for the storage of SbH_3. In the course of the study, this technique enabled us to store and use one batch of SbH_3 for one week of experiments. The apparatus is pictured in FIG. E. 4

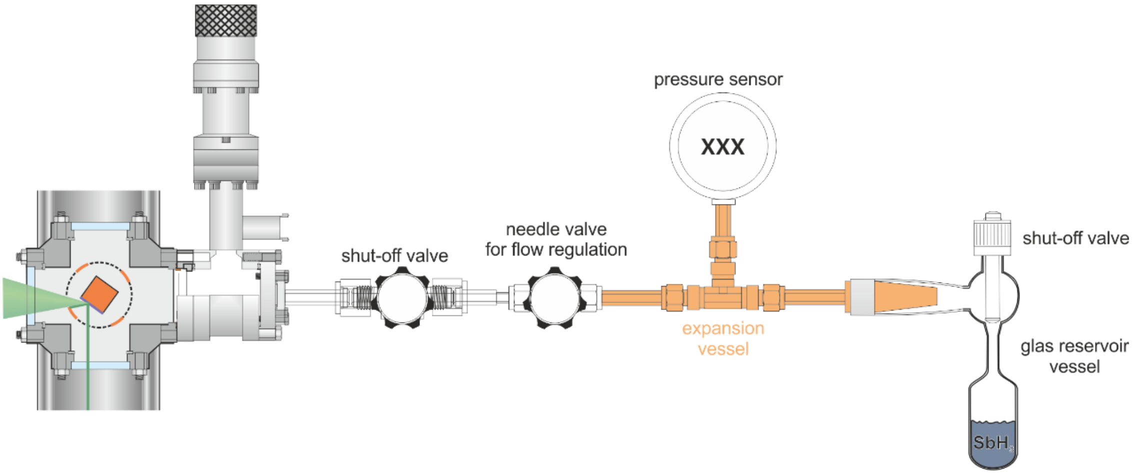

FIG. E. 4: Schematic drawing of the apparatus for the condensation of SbH_3.

6.4 THERMOLYSIS CELL

The thermolysis cell can be attached to the Raman matrix isolation apparatus and the NMR matrix isolation apparatus. It was used for the thermalization of AsH_3 in order to generate As_2H_4 and for the thermalization of P_4 in order to form P_2.

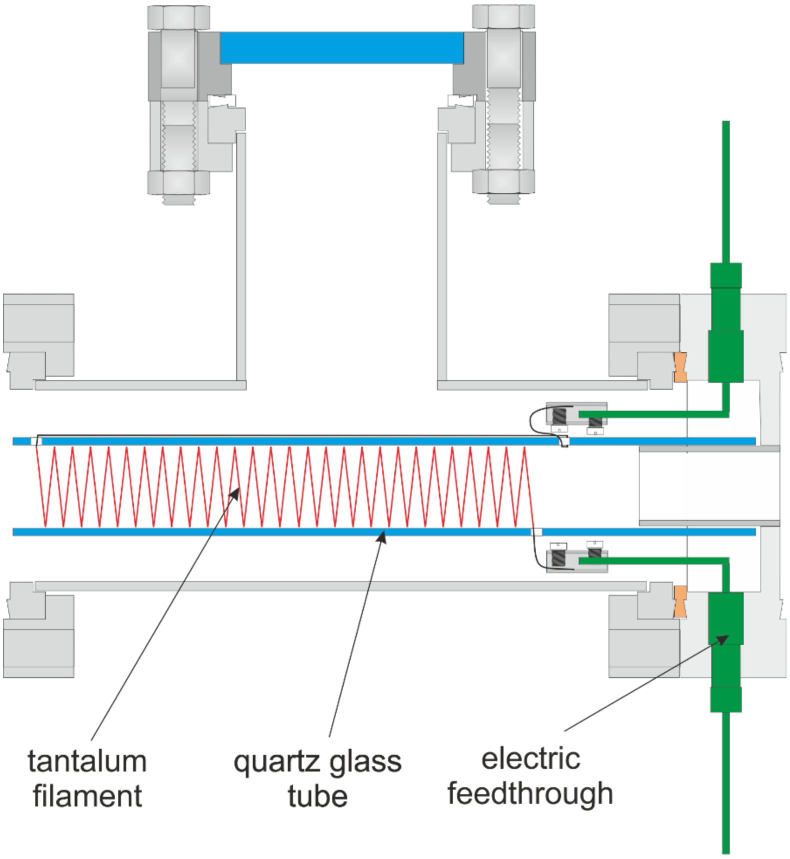

FIG. E. 5: Schematic drawing of the thermolysis cell used for the thermalization of AsH_3 and P_4.

The thermolysis cell consists of two quartz tubes pushed into each other (FIG. E. 5). The tantalum winding serves as a heating wire. In this work, temperatures of approximately 1600 °C were reached in the thermolysis cell. FIG. E. 6 shows the thermolysis cell at working temperature.

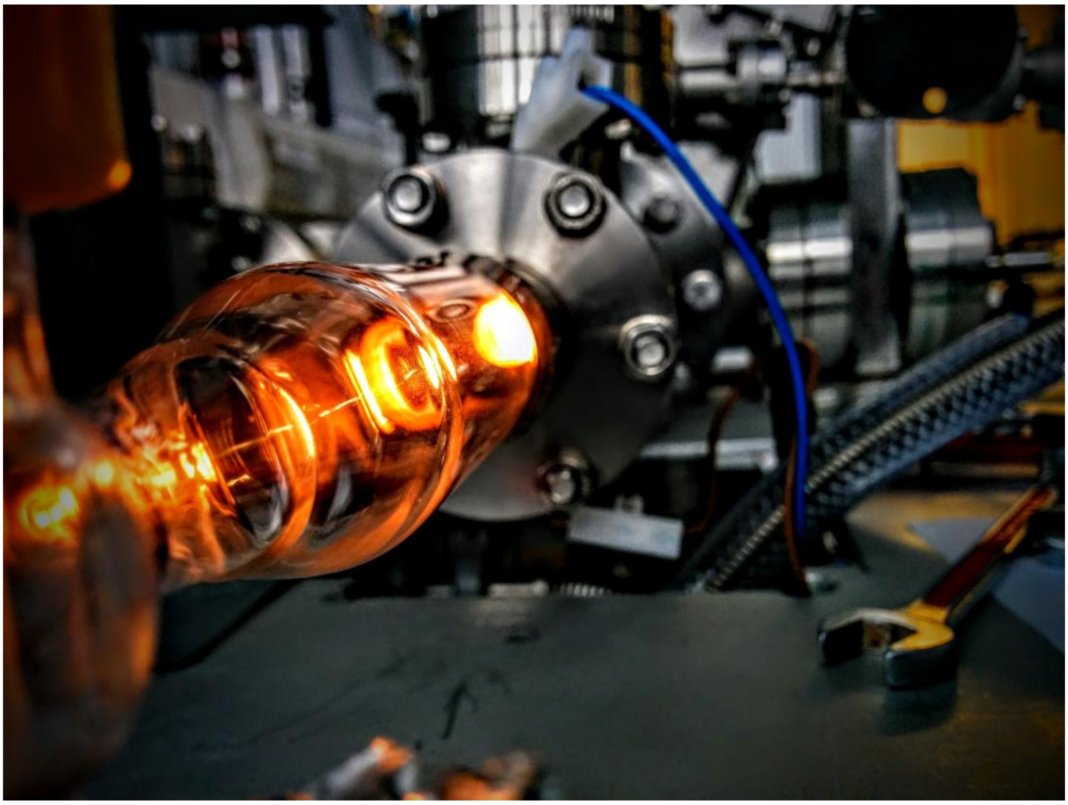

FIG. E. 6: Picture of the thermolysis cell attached to the matrix isolation NMR apparatus at 1600°C.

6.5 NMR MATRIX ISOLATION SPECTROSCOPY

The gram scale co-condensation apparatus has already been described in Chapter 4.2.1. In this chapter additional information is given. The samples of P_4 in adamantane and the P_4/P_2 mixture in adamantane were prepared using a specially designed gram scale co-condensation apparatus. A schematic drawing of the apparatus is presented in FIG. E. 7 and FIG. E. 8. It consists of a cylindrical, rotatable copper cold tip (2) (diameter 40 mm) mounted to the recipient with a custom-built ultra-high vacuum rotational feedthrough (1) (manufactured by *Ferrotec*), which ensures leak ratios below 10^{-6} mbarLs^{-1} throughout rotation and a thermolysis cell (6), which is described in Chapter 6.4

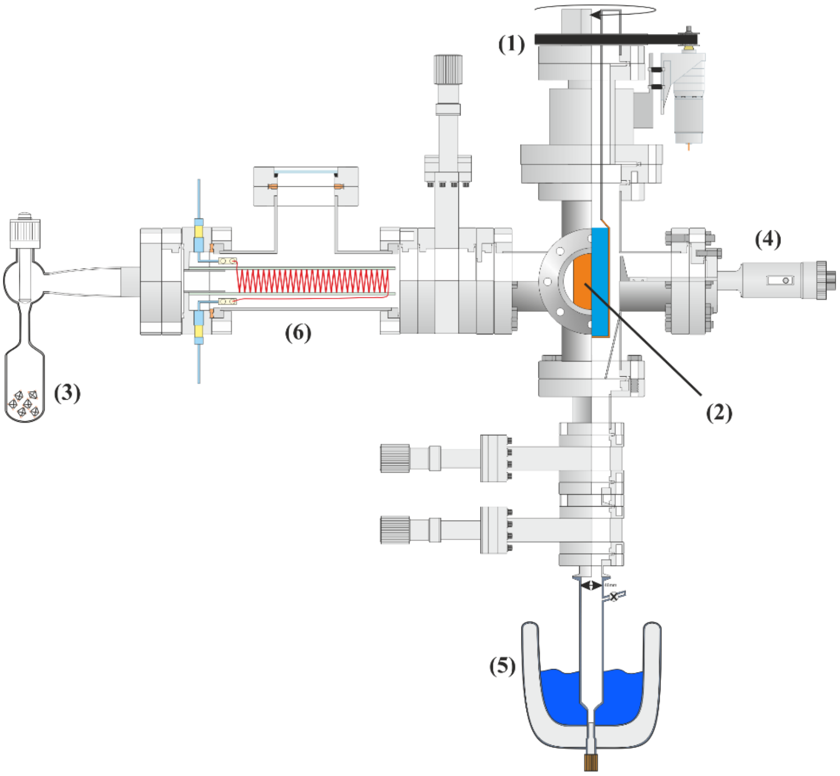

FIG. E. 7: Gram scale co-condensation apparatus equipped with the transfer tool (5).

The recipient is equipped with two orifices directed to the cold tip which allow an independent supply with adamantane vapor (3) and the guest species, respectively. A linear manipulator with a PTFE tip (4) allows to scratch the matrix layer from the cold tip. Under the rotating cold surface different matrix collection vessels can be mounted. For the diffusion control experiments a special designed transfer tool (5), which enables cooling to 195 K under inert gas atmosphere and a subsequent cooled transfer into a precooled MAS NMR spectrometer, was used. The transfer tool is described in in the supporting information of Chapter 4.. For the other experiments a sealable Schlenk vessel which can be transferred into a glove box was employed. A picture of the apparatus is given in FIG. E. 9.

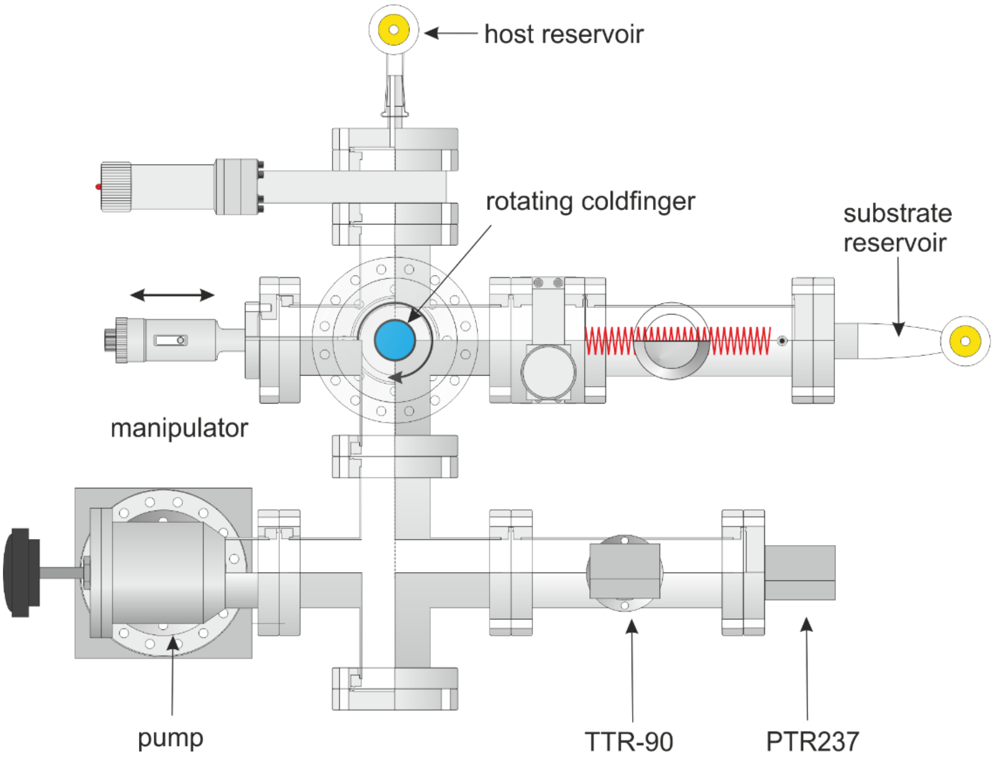

FIG. E. 8: Gram scale co-condensation apparatus from the top.

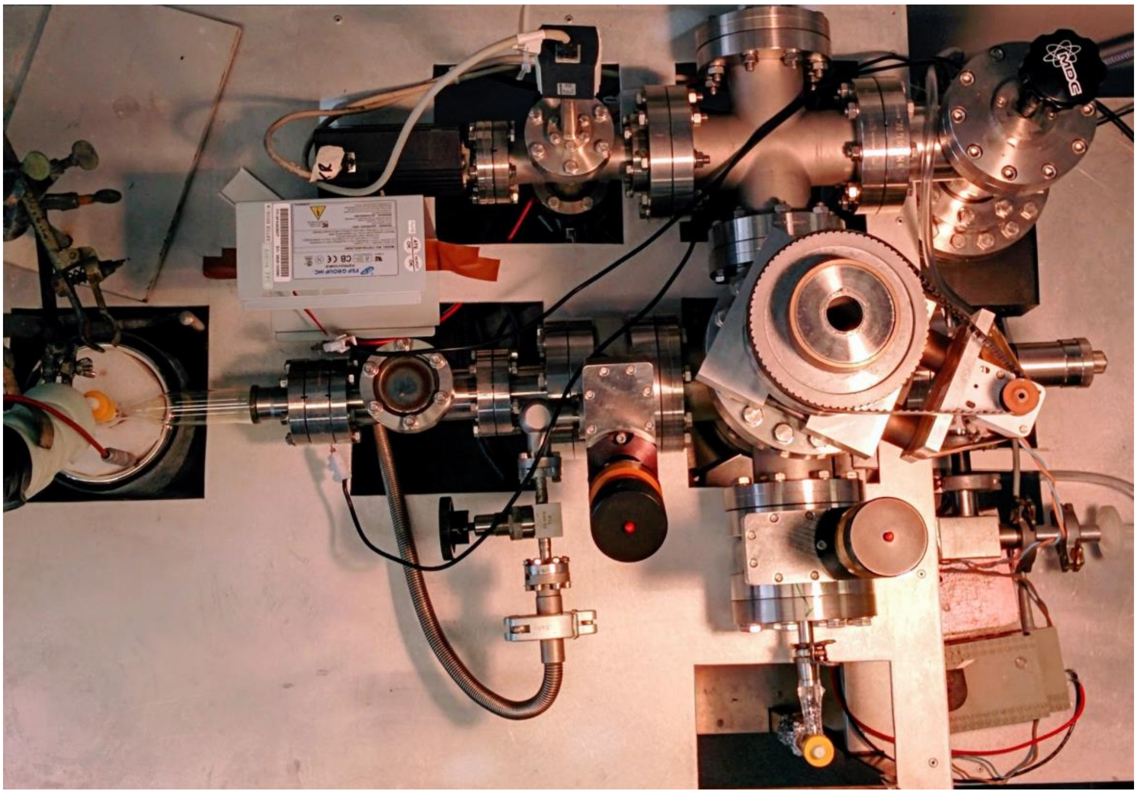

FIG. E. 9: Picture of the gram scale co-condensation apparatus.

All MAS NMR experiments were recorded on a Bruker DSX Avance 500 FT NMR Spectrometer. The magnetic field strength of the device is 11.7 T. The proton frequency is 500 MHz. The matrices were measured in commercially available rotors with a diameter of 4 mm. The usual rotation frequency of the measurements was 10 kHz. During the experiments at low temperatures, the sample was cooled with tempered nitrogen. The rotation frequency during these measurements was 4 kHz in order to avoid excessive heat input due to friction during the measurement.

7 Appendix

7.1 List of Abbreviations

Å	Angström
δ_{as}	Antisymmetric bending mode
ν_{as}	Antisymmetric stretching mode
δ	Bending mode
BDE	Bond dissociation energy
CCD	Charged coupled device
CF	Conflat
CCSD	Coupled Cluster Singles Doubles
cm^3	Cubic centimeter
cm^3/h	Cubic centimeter per hour
°	Degree
°C	Degree Celsius
eV	Electron volt
g	Gaseous
X	Halogen
HRTOF	High resolution time of Flight
h	Hour
K	Kelvin
kJ	kilo joule
kJ/mol	kilo joule per mol
l	liquid
MAS	Magic angle spinning
mbar	Millibar
mmol	Millimole
mW	Milliwatt
mmol/h	Mmol per hour
molec/cm2	Mole equivalents per square centimetre
mol	Mole
NIST	National Institute of Standards and Technology
Nd:YAG	Neodymium-doped yttrium aluminum garnet; Nd:$Y_3Al_5O_{12}$
NMR	Nuclear magnetic resonance
ppb	Parts per billion
ppm	Parts per million
%	Percentage
Pn	Pnictogen
MP2	Second order Møller-Plesset Correction
Ω	Standard Deviation

ν	Stretching mode
S/M	Substrate to Matrix ratio
δ_s	Symmetric bending mode
ν_s	Symmetric stretching mode
TS	Transition state
2D	Two dimensional

7.2 Table of Figures [FIG.]

7.3 Table of Figures [FIG S.]

7.4 Table of Figures [FIG E.]

7.5 List of Tables [TABLE.]

7.6 List of Tables [TABLE S.]

7.7 Bibliography

1. Whittle, E., D.A. Dows, and G.C. Pimentel, *Matrix Isolation Method for the Experimental Study of Unstable Species.* The Journal of Chemical Physics, 1954. **22**(11): p. 1943-1943.
2. Norman, I. and G. Porter, *Trapped Atoms and Radicals in a Glass 'Cage'.* Nature, 1954. **174**(4428): p. 2.
3. Becker, E.D. and G.C. Pimentel, *Spectroscopic studies of reactive molecules by the matrix isolation method.* The Journal of Chemical Physics, 1956. **25**: p. 224.
4. Cradock, S. and A. Hinchcliffe, *Matrix Isolation: A technique for the study of reactive inorganic species*. 1975: CUP Archive.
5. Gough, T.E., D.G. Knight, and G. Scoles, *Matrix spectroscopy in the gas phase: IR spectroscopy of argon clusters containing SF6 or CH3F.* Chemical Physics Letters, 1983. **97**(2): p. 155-160.
6. M. J. Almond, A.J.D., Advances in Spectroscopy, 1989. **17**(17): p. 1.
7. [04.July.2016]; Available from: https://scifinder.cas.org/scifinder/view/scifinder/scifinderExplore.jsf.
8. Weidlein, J., U. Müller, and K. Dehnicke, *Schwingungsspektroskopie: eine Einführung*. 1988: Thieme.
9. Brandmüller, J. and R. Claus, *Raman und seine Theorie der Gitterschwingungen.* Physikalische Blätter, 1971. **27**(7): p. 295-301.
10. Pringsheim, P., *Der Ramaneffekt, ein neuer von C. V. Raman entdeckter Strahlungseffekt.* Naturwissenschaften, 1928. **16**(31): p. 597-606.
11. Nibler, J.W. and D.A. Coe, *Depolarization Measurements in Raman Matrix Isolation Spectroscopy.* The Journal of Chemical Physics, 1971. **55**(10): p. 5133-5134.

12. Shirk, J.S. and H.H. Claassen, *Raman Spectra of Matrix-Isolated Molecules.* The Journal of Chemical Physics, 1971. **54**(7): p. 3237-3238.

13. Boal, D., et al., *Matrix Isolation Laser Raman Spectroscopy in Inorganic Chemistry.* Nature Physical Science, 1971. **231**(25): p. 174-175.

14. Beck, R. and J.W. Nibler, *High resolution Raman loss spectra of solid α-nitrogen and of matrix-isolated molecules.* Chemical Physics Letters, 1989. **159**(1): p. 79-84.

15. Hu, Z., et al., *Absorption, fluorescence, and Raman spectra of mass-selected rhenium dimers in argon matrices.* The Journal of Chemical Physics, 1994. **101**(1): p. 95-103.

16. Wang, H., et al., *Absorption, resonance Raman, and Raman excitation spectra of hafnium trimers.* The Journal of chemical physics, 1997. **106**(20): p. 8339-8343.

17. Dong, J.G., et al., *Raman spectra of mass-selected cobalt dimers in argon matrices.* The Journal of Chemical Physics, 1994. **101**(11): p. 9280-9282.

18. Kohl, J.E., M.G. Semack, and D. White, *Pulsed NMR studies of matrix isolated hydrogen chloride monomer and hydrogen chloride dimer.* The Journal of Chemical Physics, 1978. **69**(12): p. 5378-85.

19. Zilm, K.W., et al., *Low-temperature natural-abundance carbon-13 NMR spectroscopy of matrix-isolated species. The anisotropy of the shielding tensor in ethylene.* Journal of the American Chemical Society, 1978. **100**(25): p. 8038-8039.

20. Murphy, M. and D. White, *Matrix isolation nuclear magnetic resonance studies of methyl group spin–rotation coupling.* The Journal of Chemical Physics, 1989. **91**(8): p. 4504-4514.

21. Murphy, M., M.G. Semack, and D. White, *Zeeman and dipolar coherences in dilute spin I = 32 powders. matrix-isolated* CH_3CN. Journal of Magnetic Resonance (1969), 1987. **72**(1): p. 143-158.

22. Greenberg, M.M., et al., *Structure of the carrier of the cross-polarization magic angle spinning carbon-13 nuclear magnetic resonance signal assigned to 3,4-dimethylenethiophene. Multiple position-labeling and chemical trapping in annealed glasses.* Journal of the American Chemical Society., 1991. **113**(6): p. 2318-19.

23. Zilm, K.W., et al., *Two-dimensional solid-state NMR of a captive intermediate. Structure of the radical centers in 3,4-dimethylenethiophene.* Journal of the American Chemical Society, 1989. **111**(4): p. 1533-5.

24. Zilm, K.W., et al., *The first magic angle spinning NMR spectrum of a captive intermediate: direct observation of a singlet ground state biradical, 3,4-dimethylenefuran.* Journal of the American Chemical Society, 1987. **109**(5): p. 1567-9.

25. Yannoni, C.S., H.P. Reisenauer, and G. Maier, *Detection by carbon-13 CPMAS NMR of molecules photochemically generated in organic glasses at low temperature.* Journal of the American Chemical Society, 1983. **105**(19): p. 6181-6182.

26. Zilm, K.W. and D.M. Grant, *Carbon-13 dipolar spectroscopy of small organic molecules in argon matrixes.* Journal of the American Chemical Society, 1981. **103**(11): p. 2913-22.

27. Zilm, K.W., et al., *Carbon-13 magnetic resonance dipolar spectroscopy. Orientation of the chemical shift tensor in cyclopropane.* Journal of the American Chemical Society, 1981. **103**(8): p. 2119-20.

28. Zilm, K.W., et al., *Low-temperature carbon-13 magnetic resonance of solids. 1. Alkenes and cycloalkenes.* Journal of the American Chemical Society, 1980. **102**(22): p. 6672-6.

29. Kaufmann, A., *Homonukleare Cluster in Wirtsgittern*. 2009, LMU.

30. Technology, N.J.P.L.C.I.o.; Available from: https://www.jpl.nasa.gov/spaceimages/details.php?id=PIA21046.

31. Guillemin, J.C., *Laboratory photolysis of gaseous mixtures of planetary interest*, in *Exo-/Astro-Biology*, P. Ehrenfreund, O. Angerer, and B. Battrick, Editors. 2001. p. 141-144.

32. Fouchet, T., et al., *Upper limits on hydrogen halides in Jupiter from Cassini/CIRS observations.* Icarus, 2004. **170**(1): p. 237-241.

33. Teanby, N.A., et al., *New upper limits for hydrogen halides on Saturn derived from Cassini-CIRS data.* Icarus, 2006. **185**(2): p. 466-475.

34. Jutzi, P., *Advanced Inorganic Chemistry. Von F. A. Cotton und G. Wilkinson. 5. Aufl. John Wiley & Sons, New York 1988. 1455 S., Tab., Abb., geb. £ 21.95. ISBN 0-471849979.* Chemie in unserer Zeit, 1989. **23**(1): p. 35-36.

35. Heinemann, A., *Infrarotspektroskopische Untersuchungen an kristallinem Phosphorwasserstoff, Phosphoniumbromid und Phosphoniumchlorid.* Berichte der Bunsengesellschaft für physikalische Chemie, 1964. **68**(3): p. 280-286.

36. Lang, K.R., *The Cambridge Guide to the Solar System*. 2011: Cambridge University Press.

37. Atreya, S.K., et al., *A comparison of the atmospheres of Jupiter and Saturn: deep atmospheric composition, cloud structure, vertical mixing, and origin.* Planetary and Space Science, 1999. **47**(10): p. 1243-1262.

38. Noll, K.S. and H.P. Larson, *The spectrum of Saturn from 1990 to 2230 cm−1: Abundances of* AsH_3*,* CH_3D*, CO,* GeH_4*,* NH_3*, and* PH_3. Icarus, 1991. **89**(1): p. 168-189.

39. Guillemin, J.-C. *Laboratory photolysis of gaseous mixtures of planetary interest*. in *Exo-/Astro-Biology*. 2001.

40. Heinemann, A., *Infrarotspektroskopische Untersuchungen an AsH_3, SbH_3 und den Systemen AsH_3/Halogenwasserstoff und SbH_3/Halogenwasserstoff im Kristallzustand Ein infrarotspektroskopischer Nachweis des Arsoniumions.* Berichte der Bunsengesellschaft für physikalische Chemie, 1964. **68**(3): p. 287-295.

41. Balimann, G. and P.S. Pregosin, *Arsenic-75 nuclear magnetic resonance. A study of some arsenic salts.* Journal of Magnetic Resonance (1969), 1977. **26**(2): p. 283-289.

42. Gut, R., *The phosphonium - sulfonium - and arsonium — salts of TaF_6− and Ta2F_{11}−.* Inorganic and Nuclear Chemistry Letters, 1976. **12**(2): p. 149-152.

43. Kornath, A., *Multi-Channel Raman Matrix Isolation Spectroscopy.* Journal of Raman Spectroscopy, 1997. **28**(1): p. 9-14.

44. Brauer, G., *Handbuch der präparativen anorganischen Chemie*. Vol. 3. 1981.

45. Bartlett, R.J. and M. Musiał, *Coupled-cluster theory in quantum chemistry.* Reviews of Modern Physics, 2007. **79**(1): p. 291-352.

46. Čížek, J., *On the Use of the Cluster Expansion and the Technique of Diagrams in Calculations of Correlation Effects in Atoms and Molecules*, in *Advances in Chemical Physics*. 2007.

47. Purvis, G.D. and R.J. Bartlett, *A full coupled-cluster singles and doubles model: The inclusion of disconnected triples.* The Journal of Chemical Physics, 1982. **76**(4): p. 1910-1918.

48. Scuseria, G.E., C.L. Janssen, and H.F. Schaefer, *An efficient reformulation of the closed-shell coupled cluster single and double excitation (CCSD) equations.* The Journal of Chemical Physics, 1988. **89**(12): p. 7382-7387.

49. Scuseria, G.E. and H.F. Schaefer, *Is coupled cluster singles and doubles (CCSD) more computationally intensive than quadratic configuration interaction (QCISD)?* The Journal of Chemical Physics, 1989. **90**(7): p. 3700-3703.

50. Frisch, M.J., M. Head-Gordon, and J.A. Pople, *A direct MP2 gradient method.* Chemical Physics Letters, 1990. **166**(3): p. 275-280.

51. Frisch, M.J., M. Head-Gordon, and J.A. Pople, *Semi-direct algorithms for the MP2 energy and gradient.* Chemical Physics Letters, 1990. **166**(3): p. 281-289.

52. Head-Gordon, M. and T. Head-Gordon, *Analytic MP2 frequencies without fifth-order storage. Theory and application to bifurcated hydrogen bonds in the water hexamer.* Chemical Physics Letters, 1994. **220**(1): p. 122-128.

53. Head-Gordon, M., J.A. Pople, and M.J. Frisch, *MP2 energy evaluation by direct methods.* Chemical Physics Letters, 1988. **153**(6): p. 503-506.

54. Møller, C. and M.S. Plesset, *Note on an Approximation Treatment for Many-Electron Systems.* Physical Review, 1934. **46**(7): p. 618-622.

55. Sæbø, S. and J. Almlöf, *Avoiding the integral storage bottleneck in LCAO calculations of electron correlation.* Chemical Physics Letters, 1989. **154**(1): p. 83-89.

56. Davidson, E.R., *Comment on "Comment on Dunning's correlation*-consistent basis *sets".* Chemical Physics Letters, 1996. **260**(3): p. 514-518.

57. Dunning, T.H., *Gaussian basis sets for use in correlated molecular calculations. I. The atoms boron through neon and hydrogen.* The Journal of Chemical Physics, 1989. **90**(2): p. 1007-1023.

58. Kendall, R.A., T.H. Dunning, and R.J. Harrison, *Electron affinities of the first-row atoms revisited. Systematic basis sets and wave functions.* The Journal of Chemical Physics, 1992. **96**(9): p. 6796-6806.

59. Peterson, K.A., D.E. Woon, and T.H. Dunning, *Benchmark calculations with correlated molecular wave functions. IV. The classical barrier height of the H+H2→H2+H reaction.* The Journal of Chemical Physics, 1994. **100**(10): p. 7410-7415.

60. Wilson, A.K., T. van Mourik, and T.H. Dunning, *Gaussian basis sets for use in correlated molecular calculations. VI. Sextuple zeta correlation consistent basis sets for boron through neon.* Journal of Molecular Structure: THEOCHEM, 1996. **388**: p. 339-349.

61. Woon, D.E. and T.H. Dunning, *Gaussian basis sets for use in correlated molecular calculations. III. The atoms aluminum through argon.* The Journal of Chemical Physics, 1993. **98**(2): p. 1358-1371.

62. Frisch, M.J., et al., *Gaussian 09, Revision B.01*. 2009: Wallingford CT.

63. Andrews, L. and T.C. McInnis, *Cocondensation reaction of arsine and fluorine: matrix infrared spectrum of fluoroarsine.* Inorganic Chemistry, 1991. **30**(15): p. 2990-2993.

64. Dixon, R.N., et al, *The analysis of a* $^2A_1$-$^2B_1$ *electronic band system of the* AsH_2 *and* AsD_2 *radicals.* Proceedings of the Royal Society of London. Series A. Mathematical and Physical Sciences, 1968. **305**(1481): p. 271-290.

65. R. Minkwitz, A.K., W Sawodny, H. Härtner, Zeitschrift für anorganische und allgemeine Chemie, 1994. **620**(4): p. 753-756.

66. Noble-Eddy, R., et al., *Molecular structures of vinylarsine, vinyldichloroarsine and arsine studied by gas-phase electron diffraction and quantum chemical calculations.* Journal of Molecular Structure, 2010. **978**(1): p. 26-34.

67. Kutzelnigg, W., *Die chemische Bindung bei den höheren Hauptgruppenelementen.* Angewandte Chemie, 1984. **96**(4): p. 262-286.

68. *Über die Darstellung der Pnikogenoniumsalze AsH4+SbF6−, AsH4+AsF6−,* $SbH_4^+SbF_6^-$. Zeitschrift für anorganische und allgemeine Chemie, 1994. **620**(4): p. 753-756.

69. Enjalbert, R. and J. Galy, *Crystal structure of arsenic trifluoride* AsF_3 *at 193 K.* C. R. Hebd. Seances Acad. Sci., Ser. C, 1979. **289**(16): p. 441-3.

70. Holleman, A.F., E. Wiberg, and N. Wiberg, *Lehrbuch der anorganischen Chemie*. 2007: Walter de Gruyter.

71. Maier, L., *Phosphorverbindungen und ihre technische Bedeutung.* Chemie in unserer Zeit, 1975. **9**(4): p. 109-116.

72. Gray, T. and N. Mann, *Die Elemente: Bausteine unserer Welt*. 2010: Fackelträger-Verlag.

73. Ridgway, S., L. Wallace, and G. Smith, *The 800-1200 inverse centimeter absorption spectrum of Jupiter.* The Astrophysical Journal, 1976. **207**: p. 1002-1006.

74. Larson, H., U. Fink, and R. Treffers, *Phosphine in Jupiter's atmosphere-The evidence from high-altitude observations at 5 micrometers.* The Astrophysical Journal, 1977. **211**: p. 972-979.

75. Schäfer, H., *Elektromagnetische Strahlung: Informationen aus dem Weltall*. 1985: Springer.

76. Gillett, F. and W. Forrest, *The 7.5-to 13.5-micron spectrum of Saturn.* The Astrophysical Journal, 1974. **187**: p. L37.

77. Greicius, T. *Jupiter: A New Point of View*. 2017; Available from: https://www.nasa.gov/image-feature/jpl/pia21778/jupiter-a-new-point-of-view.

78. Melville, H., *The photochemistry of phosphine.* Proceedings of the Royal Society of London. Series A, Containing Papers of a Mathematical and Physical Character, 1932. **138**(835): p. 374-395.

79. Norrish, R. and G. Oldershaw, *The flash photolysis of phosphine.* Proceedings of the Royal Society of London. Series A, Mathematical and Physical Sciences, 1961: p. 1-9.

80. Loeffler, M.J. and R.L. Hudson, *Coloring Jupiter's clouds: Radiolysis of ammonium hydrosulfide (NH_4SH).* Icarus, 2018. **302**: p. 418-425.

81. Ferris, J.P. and R. Benson, *Diphosphine is an intermediate in the photolysis of phosphine to phosphorus and hydrogen.* Nature, 1980. **285**(5761): p. 156-157.

82. Ferris, J.P. and H. Khwaja, *Laboratory simulations of PH3 photolysis in the atmospheres of Jupiter and Saturn.* Icarus, 1985. **62**(3): p. 415-424.

83. Andrews, L. and R. Withnall, *Cocondensation reaction between phosphine and fluorine: matrix infrared spectra of difluorophosphorane, difluorophosphine and fluorophosphine.* Inorganic Chemistry, 1989. **28**(3): p. 494-499.

84. Beckers, H., *Gasphasenreaktionen von H_3PF_2: Darstellung der Monohalogenphosphane H_2PF und H_2PCl.* Zeitschrift für anorganische und allgemeine Chemie, 1993. **619**(11): p. 1880-1886.

85. Beckers, H., H. Burger, and M. Paplewski, *High-Resolution FTIR Study of the PH Stretching Bands v^1 and v^5 of PH_2F and PH_2Cl.* Journal of Molecular Spectroscopy, 1995. **171**(2): p. 546-554.

86. Minkwitz, R., et al., *Schwingungsspektren und Kraftfeldberechnungen an Fluorphosphoniumkationen $PX_{4-n}F_n^+$ (X= H, D; n= 0-4)/Vibrational Spectra and Force-Field-Calculations of Fluorophosphonium Cations $PX_{4-n}F_n^+$ (X= H, D; n= 0-4).* Zeitschrift für Naturforschung B, 1992. **47**(12): p. 1661-1666.

87. Shimanouchi, T., *Tables of molecular vibrational frequencies. Consolidated volume I.* 1972: Washington, D.C. : National Bureau of Standards, 1972.

88. Rush, J.J., A.J. Melveger, and E.R. Lippincott, *Laser-Raman spectra of PH_4I, PH_4Br, and PH_4Cl.* J. Chem. Phys., 1969. **51**(7): p. 2947-55.

89. Abraham, P., et al., *Raman spectroscopy of PH_3 and PH_2 at high temperature and simulation of PH_3 Raman spectrum.* Journal of Raman Spectroscopy, 1992. **23**(7): p. 379-384.

90. Hoffman, J., H. Nielsen, and K.N. Rao, *v_2 and v_4 Bands in the Infrared Spectrum of Phosphine*. Berichte der Bunsengesellschaft für physikalische Chemie, 1960. **64**(5): p. 606-616.

91. Gutowsky, H.S. and A.D. Liehr, *The Infrared Spectra of PF_3, POF_3, and PF_5*. The Journal of Chemical Physics, 1952. **20**(10): p. 1652-1653.

92. Dixon, B.E. and P.R. Kiff, *The decomposition of stibine*. Journal of Applied Chemistry, 1958. **8**(10): p. 631-636.

93. Swart, M., E. Roesler, and F.M. Bickelhaupt, *Proton affinities of maingroup-element hydrides and noble gases: trends across the periodic table, structural effects, and DFT validation*. Journal of Computational Chemistry, 2006. **27**(13): p. 1486-1493.

94. Nielsen, H., *The Structure of the Molecules PH_3, AsH_3, and SbH_3*. The Journal of Chemical Physics, 1952. **20**(4): p. 759-759.

95. Nielsen, H.H., *The Molecular Structure of Arsine*. The Journal of Chemical Physics, 1952. **20**(12): p. 1955-1956.

96. Sirvetz, M.H. and R.E.W. Jr., *The Structure of Phosphine*. The Journal of Chemical Physics, 1953. **21**(5): p. 898-902.

97. Klapdor Martin, F., et al., *Die Kristallstrukturen von PHF_4, PH_2F_3 und PHF_2. Moden molekularer Packung bei tiefer Temperatur [1] / The Crystal Structures of PHF_4, PH_2F_3 and PHF_2. Molecular Packing Modes at Low Temperature*, in *Zeitschrift für Naturforschung B*. 1997. p. 1051.

98. Bondi, A., *van der Waals Volumes and Radii*. The Journal of Physical Chemistry, 1964. **68**(3): p. 441-451.

99. Minkwitz, R., et al., *Über die Darstellung der Pnikogenoniumsalze $AsH_4^+SbF_6^-$, $AsH_4^+AsF_6^-$, $SbH_4^+SbF_6^-$*. Zeitschrift für anorganische und allgemeine Chemie, 1994. **620**(4): p. 753-756.

100. Moore, C.E., *Atomic Energy Levels: as derived from the analyses of optical spectra*. 1949: US Department of Commerce, National Bureau of Standards.

101. Desclaux, J.P., *Relativistic Dirac-Fock expectation values for atoms with Z = 1 to Z = 120.* Atomic Data and Nuclear Data Tables, 1973. **12**(4): p. 311-406.

102. Seiff, A., et al., *Thermal structure of Jupiter's atmosphere near the edge of a 5-μm hot spot in the north equatorial belt.* Journal of Geophysical Research: Planets, 1998. **103**(E10): p. 22857-22889.

103. Aoyagi, Y., et al., *Characteristics of laser metalorganic vapor-phase epitaxy in GaAs.* Journal of Applied Physics, 1986. **60**(9): p. 3131-3135.

104. Donnelly, V.M. and R.F. Karlicek, *Development of laser diagnostic probes for chemical vapor deposition of InP/InGaAsP epitaxial layers.* Journal of Applied Physics, 1982. **53**(9): p. 6399-6407.

105. Kukimoto, H., et al., *Selective area control of material properties in laser-assisted MOVPE of GaAs and AlGaAs.* Journal of Crystal Growth, 1986. **77**(1): p. 223-228.

106. Pütz, N., et al., *Photostimulated growth of GaAs in the MOCVD system.* Journal of Crystal Growth, 1984. **68**(1): p. 194-199.

107. Smith-Freeman, L.A., W.P. Schroeder, and C. Wittig, *AsH_3 Ultraviolet Photochemistry.* The Journal of Physical Chemistry A, 2009. **113**(10): p. 2158-2164.

108. Dixon, R.N., G. Duxbury, and H. Lamberton, *The analysis of a 2A1-2B1 electronic band system of the AsH_2 and AsD_2 radicals.* Proc. R. Soc. Lond. A, 1968. **305**(1481): p. 271-290.

109. Ni, T., et al., *The emission spectrum of $AsH_2(\tilde{A}^2A_1 \rightarrow \tilde{X}^2B_1)$ via uv photolysis of AsH_3.* Chemical Physics Letters, 1986. **126**(5): p. 417-420.

110. Fujiwara, H., et al., *Submillimeter-wave spectrum of the AsH_2 radical in the $^2B_1$ ground electronic state.* The Journal of Chemical Physics, 1998. **109**(13): p. 5351-5355.

111. Fujiwara, H. and S. Saito, *Microwave Spectrum of the* $AsD_2(\tilde{X}^2B_1)$ *Radical: Harmonic Force Field and Molecular Structure.* Journal of Molecular Spectroscopy, 1998. **192**(2): p. 399-405.

112. He, S.-G. and D.J. Clouthier, *Laser spectroscopy and dynamics of the jet-cooled* AsH_2 *free radical.* The Journal of Chemical Physics, 2007. **126**(15): p. 154312.

113. Zhao, D., et al., *Absorption spectra of* AsH_2 *radical in 435–510nm by cavity ringdown spectroscopy.* Journal of Molecular Spectroscopy, 2009. **256**(2): p. 192-197.

114. Nast, R., *Über das Diarsin,* As_2H_4*.* Chemische Berichte, 1948. **81**(3): p. 271-277.

115. Omstead, T.R., A.V. Annapragada, and K.F. Jensen, *Microwave plasma generation of arsine from hydrogen and solid arsenic.* Applied Physics Letters, 1990. **57**(24): p. 2543-2545.

116. Jackel, G.S. and W. Gordy, *Electron Spin Resonance of Free Radicals Formed from Group-IV and Group-V Hydrides in Inert Matrices at Low Temperature.* Physical Review, 1968. **176**(2): p. 443-452.

117. Jordan, A.S. and A. Robertson, *Thermodynamic properties of* AsH_3 *and its subhydrides.* Journal of Materials Science: Materials in Electronics, 1993. **4**(3): p. 215-224.

118. Huo, Y., et al., *The study of the properties of the ground- and low.lying states of* AsH_2*,* AsH_2^+ *AND* AsH_2^-. Journal of Theoretical and Computational Chemistry, 2012. **12**(02): p. 1250115.

119. Durig, J.R. and J.M. Casper, *Vibrational Spectra and Structure of Tetramethyldiarsine in the Crystalline and Fluid States.* The Journal of Chemical Physics, 1971. **55**(1): p. 198-204.

120. Kornath, A.J., A. Kaufmann, and S. Cappellacci, *Raman spectroscopic studies on matrix-isolated arsenic and antimony molecules* As_4 *and* Sb_4 *in noble gas matrices.* Journal of Molecular Spectroscopy, 2009. **255**(2): p. 189-193.

121. Downs, A.J., et al., *The molecular structure of tetramethyldiarsine,* $As_2(CH_3)_4$*, in the gas phase as determined by electron diffraction.* Journal of Molecular Structure, 1991. **248**(3): p. 393-406.

122. Leibniz, G.W., *Historia inventionis phosphori.* Miscellanea Berolinensia ad incrementum scientiarum. **1710**(1): p. 91-98.

123. Dainton, F.S., *X—X and X—O bond energies of phosphorus, arsenic and antimony and their importance in the kinetics of the oxidation of these elements.* Transactions of the Faraday Society, 1947. **43**(0): p. 244-256.

124. Barber, J., et al., *Evidence for the Production of* N_4 *via the* $N_2\ A^3\Sigma_u^+ + N_2\ A^3\Sigma_u^+$ *Energy Pooling Reaction.* The Journal of Physical Chemistry A, 2006. **110**(11): p. 3853-3856.

125. Zheng, J.P., et al., *Tetrazete (*N_4*). Can it be prepared and observed?* Chemical Physics Letters, 2000. **328**(1): p. 227-233.

126. Kornath, A., A. Kaufmann, and M. Torheyden, *Raman spectroscopic studies on matrix-isolated phosphorus molecules* P_4 *and* P_2. The Journal of Chemical Physics, 2002. **116**(8): p. 3323-3326.

127. Choi, W., et al., *Safe* P_4 *reagent in a reusable porous coordination network.* Dalton Trans., 2016. **45**(15): p. 6357-6360.

128. Yang, D., et al., *Air- and Light-Stable* P_4 *and* As_4 *within an Anion-Coordination-Based Tetrahedral Cage.* Journal of the American Chemical Society, 2017. **139**(16): p. 5946-5951.

129. Mal, P., et al., *White Phosphorus Is Air-Stable Within a Self-Assembled Tetrahedral Capsule.* Science, 2009. **324**(5935): p. 1697-1699.

130. Seitz, A.E., et al., *Facile storage and release of white phosphorus and yellow arsenic.* Nature Communications, 2018. **9**(1): p. 361.

131. Locke, I.W., et al., *Phosphorus/buckminsterfullerene intercalation compounds, $C_{60}(P_4)_2$*. Chemical Physics Letters, 1994. **225**(1–3): p. 186-190.

132. Douthwaite, R.E., et al., *Synthesis and characterisation of the inclusion complex $\{(P_4)_2C_{60}\}$*. Journal of the Chemical Society, Chemical Communications, 1994(11): p. 1367-1368.

133. Siebert, H., J. Eints, and E. Fluck, *Notizen: Kernresonanzspektrum und Struktur des Trisilylphosphins*, in *Zeitschrift für Naturforschung B*. 1968. p. 1006.

134. Gernot Heckmann, E.F., *^{31}P-Kernresonanzdaten von weißem Phosphor und Lösungen des weißen Phosphors.* Zeitschrift für Naturforschung B, 1969. **24b**: p. 1093-1094.

135. Oschatz, M., et al., *Chapter Four - Interactions Between Electrolytes and Carbon-Based Materials—NMR Studies on Electrical Double-Layer Capacitors, Lithium-Ion Batteries, and Fuel Cells*, in *Annual Reports on NMR Spectroscopy*, G.A. Webb, Editor. 2016, Academic Press. p. 237-318.

136. Cossairt, B.M., et al., *On the Molecular and Electronic Structures of AsP_3 and P_4.* Journal of the American Chemical Society, 2010. **132**(24): p. 8459-8465.

137. Schwarzmaier, C., et al., *Stabilization of Tetrahedral P_4 and As_4 Molecules as Guests in Polymeric and Spherical Environments.* Angewandte Chemie International Edition, 2013. **52**(41): p. 10896-10899.

138. Yang, D., et al., *Correction to "Air- and Light-Stable P_4 and As_4 within an Anion-Coordination-Based Tetrahedral Cage".* Journal of the American Chemical Society, 2017. **139**(20): p. 7130-7130.

139. Heckmann, G. and E. Fluck, *^{31}P nuclear magnetic resonance chemical shifts of elemental phosphorus in the gas phase.* Molecular Physics, 1972. **23**(1): p. 175-183.

140. Di Vaira, M., et al., *Hydrolytic disproportionation of coordinated white phosphorus in [CpRu(dppe)(η*^{1}*-*P_4*)]*PF_6 *[dppe=1,2-bis(diphenylphosphino)ethane].* Journal of Organometallic Chemistry, 2006. **691**(18): p. 3931-3937.

141. Boros, È., et al., *On the dissolution of non-metallic solid elements (sulfur, selenium, tellurium and phosphorus) in ionic liquids.* Chemical Communications, 2010. **46**(5): p. 716-718.

142. Ramireddy, T., et al., *Phosphorus–carbon nanocomposite anodes for lithium-ion and sodium-ion batteries.* Journal of Materials Chemistry A, 2015. **3**(10): p. 5572-5584.

143. F., G.M., et al., *Unexpected Reactivity of Red Phosphorus in Ionic Liquids.* European Journal of Inorganic Chemistry, 2015. **2015**(24).

144. Bytchkov, A., et al., ^{31}*P solid-state NMR studies of the short-range order in phosphorus–selenium glasses.* Physical Chemistry Chemical Physics, 2010. **12**(7): p. 1535-1542.

145. Thomas, W., et al., *Structural Characterization of Phosphorus-Based Networks and Clusters:* ^{31}*P MAS NMR Spectroscopy and Magnetic Shielding Calculations on Hittorf's Phosphorus.* Chemistry – A European Journal, 2011. **17**(31): p. 8739-8748.

146. Lange, S., P. Schmidt, and T. Nilges, Au_3SnP_7*@Black Phosphorus: An Easy Access to Black Phosphorus.* Inorganic Chemistry, 2007. **46**(10): p. 4028-4035.

147. Fort, R.C. and P.v.R. Schleyer, *Adamantane: Consequences of the Diamondoid Structure.* Chemical Reviews, 1964. **64**(3): p. 277-300.

148. Chang, S.-S. and E.F. Westrum, *HEAT CAPACITIES AND THERMODYNAMIC PROPERTIES OF GLOBULAR MOLECULES. I. ADAMANTANE AND HEXAMETHYLENETETRAMINE1.* The Journal of Physical Chemistry, 1960. **64**(10): p. 1547-1551.

149. Wu, P.J., L. Hsu, and D.A. Dows, *Spectroscopic Study of the Phase Transition in Crystalline Adamantane.* The Journal of Chemical Physics, 1971. **54**(6): p. 2714-2721.

150. Nordman, C.E. and D.L. Schmitkons, *Phase transition and crystal structures of adamantane.* Acta Crystallographica, 1965. **18**(4): p. 764-767.

151. Stephenson, C.C., et al., *The thermodynamic properties of elementary phosphorus The heat capacities of two crystalline modifications of red phosphorus, of α and β white phosphorus, and of black phosphorus from 15 to 300 K.* The Journal of Chemical Thermodynamics, 1969. **1**(1): p. 59-76.

152. Spiess, H.W., R. Grosescu, and H. Haeberlen, *Molecular motion studied by NMR powder spectra. II. Experimental results for solid* P_4 *and solid* $Fe(CO)_5$. Chemical Physics, 1974. **6**(2): p. 226-234.

153. Krossing, I. and L. van Wüllen, *Superweak Complexes of Tetrahedral* P_4 *Molecules with the Silver Cation of Weakly Coordinating Anions.* Chemistry – A European Journal, 2002. **8**(3): p. 700-711.

154. Krossing, I., $Ag(P_4)_2^+$*: The First Homoleptic Metal−Phosphorus Cation.* Journal of the American Chemical Society, 2001. **123**(19): p. 4603-4604.

155. Kühl, O., *Phosphorus-31 NMR spectroscopy: a concise introduction for the synthetic organic and organometallic chemist*. 2008: Springer Science & Business Media.

156. Zilm, K.W., et al., *The nature of the phosphorus-phosphorus double bond as studied by solid-state NMR.* Journal of the American Chemical Society, 1988. **110**(7): p. 2032-2038.

157. Latypov, S.K., et al., *Quantum chemical calculations of 31P NMR chemical shifts: scopes and limitations.* Physical Chemistry Chemical Physics, 2015. **17**(10): p. 6976-6987.

158. Antušek, A., M. Jaszuński, and M. Olejniczak, *Ab initio study of NMR shielding constants and spin-rotation constants in N, P and As diatomic molecules.* Computational and Theoretical Chemistry, 2011. **970**(1): p. 54-60.

159. Resing, H.A., *NMR Relaxation Times in Solid White Phosphorus: Diffusion and Rotation.* The Journal of Chemical Physics, 1962. **37**(11): p. 2575-2583.

160. Hohl, D. and R.O. Jones, *Polymerization in liquid phosphorus: Simulation of a phase transition.* Physical Review B, 1994. **50**(23): p. 17047-17053.

7.8 Publications

02/2019 **Front Cover: Investigation of Malonic Acid in Superacidic Solutions**

European Journal of Organic Chemistry

Manuel Schickinger, Florian Zischka, Karin Stierstorfer, Andreas Kornath

DOI: 10.1002/ejoc.201900229

02/2019 **Structural Investigation of Thiourea dioxide in Superacid**

European Journal of Inorganic Chemistry

Dominik Leitz, Alexander Nitzer, Yvonne Morgenstern, Florian Zischka, Andreas J. Kornath

DOI: 10.1002/ejic.201801298

12/2018 **Front Cover: Protonation of *p*-Benzoquinone in Superacidic Solutions**

Zeitschrift für anorganische und allgemeine Chemie

Manuel Schickinger, Markus Siegert, Yvonne Morgenstern,
Florian Zischka, Karin Stierstorfer, Andreas Kornath

DOI: 10.1002/zaac.201870231

11/2018 **Catalyst-Free Enantiospecific Olefination with in-situ Generated Organocerium Species**

Angewandte Chemie

Arif Music, Clément Hoarau, Nicolas Hilgert, Florian Zischka,
Dr. Dorian Didier

DOI: 10.1002/anie.201810327

11/2018 **The Tetrahydroxydicarbenium Cation $[(HO)_2CC(OH)_2]_2^+$: Synthesis and Structure**

ChemistrySelect

Manuel Schickinger, Thomas Saal, Florian Zischka, Joachim Axhausen, Karin Stierstorfer, Yvonne Morgenstern, Prof. Andreas J. Kornath

DOI: 10.1002/slct.201802456

11/2018 **Investigation of Malonic Acid in Superacidic Solutions**

European Journal of Organic Chemistry

Manuel Schickinger, Florian Zischka, Karin Stierstorfer, Andreas Kornath

DOI: 10.1002/ejoc.201801382

10/2018 **Protonation of *p*-Benzoquinone in Superacidic Solutions**

Zeitschrift für anorganische und allgemeine Chemie

Manuel Schickinger, Markus Siegert, Yvonne Morgenstern,
Florian Zischka, Karin Stierstorfer, Andreas Kornath

DOI: 10.1002/zaac.201800394

10/2018 **Cover Feature: Tuning the Anomeric Effect in Sulfamide with Superacids**

Chemistry - A European Journal

Dominik Leitz, Marie C. Bayer, Yvonne Morgenstern, Florian Zischka, Prof. Dr. Andreas J. Kornath

https://doi.org/10.1002/chem.201804741

10/2018 **Preparation and Structure of Protonated Selenourea**

European Journal of Inorganic Chemistry

Dominik Leitz, Alan Virmani, Yvonne Morgenstern, Florian Zischka, Andreas J. Kornath

DOI: 10.1002/ejic.201800933

09/2018	**Investigations on Croconic Acid in Superacidic Media** European Journal of Organic Chemistry Manuel Schickinger, Christoph Jessen, Yvonne Morgenstern, Katharina Muggli, Florian Zischka, Andreas Kornath DOI: 10.1002/ejoc.201801035
09/2018	**Tuning the Anomeric Effect in Sulfamide with Superacids** Chemistry - A European Journal Dominik Leitz, Marie C. Bayer, Yvonne Morgenstern, Florian Zischka, Prof. Dr. Andreas J. Kornath DOI: 10.1002/chem.201804741
09/2018	**The Diprotonation of Guanidine in Superacidic Solutions** Chemistry - A European Journal Yvonne Morgenstern, Florian Zischka, Prof. Dr. Andreas Kornath DOI: 10.1002/chem.201803726
08/2018	**Front Cover: Dimethylhydroxyoxosulfonium (VI) Hexafluoridometallates, $[(CH_3)_2 SO(OX)]^+ [MF_6]^-$ (X = H, D; M = As, Sb)** Zeitschrift für anorganische und allgemeine Chemie Dominik Leitz, Gloria Betzenbichler, Yvonne Morgenstern, Florian Zischka, Andreas Kornath DOI: 10.1002/zaac.201870151
07/2018	**Dimethylhydroxyoxosulfonium(VI) Hexafluoridometallates, $[(CH_3)_2 SO(OX)]^+ [MF_6]^-$ (X = H, D; M = As, Sb)** Zeitschrift für anorganische und allgemeine Chemie Dominik Leitz, Gloria Betzenbichler, Yvonne Morgenstern, Florian Zischka, Andreas Kornath DOI: 10.1002/zaac.201800219

07/2018

Front Cover: Preparation and Characterization of Pure Thiosulfuric Acid

Zeitschrift für anorganische und allgemeine Chemie

Mathias Hopfinger, Florian Zischka, Mathias Seifert, Andreas J. Kornath

DOI: 10.1002/zaac.201870121

06/2018

Investigations on Squaric Acid in Superacidic Media

Chemistry - A European Journal

Manuel Schickinger, Denise Cibu, Florian Zischka, Karin Stierstorfer, Christoph Jessen, Prof. Dr. Andreas Kornath

DOI: 10.1002/chem.201802516

05/2018

Preparation and Characterization of Pure Thiosulfuric Acid

Zeitschrift für anorganische und allgemeine Chemie

Mathias Hopfinger, Florian Zischka, Mathias Seifert, Andreas J. Kornath

DOI: 10.1002/zaac.201800105

04/2018

The Influence of the Counterions $[AsF_6]^-$ and $[GeF_6]_2^-$ on the Structure of the $[ClSO_2NH_3]^+$ Cation

Zeitschrift für anorganische und allgemeine Chemie

Dominik Leitz, Karin Stierstorfer, Yvonne Morgenstern, Florian Zischka, Andreas J. Kornath

DOI: 10.1002/zaac.201800067

7.9 Contributions to Conferences

04/2015	„Chemistry, Environment and Nanotechnology International Science Conference” in Danzig, Poland Awards: best poster presentation **Topic: „Influence of adamantane as a host on matrix-isolated MePDF$_3$**”
08/2015	„21st International Symposium on Fluorine Chemistry / 6th International Symposium on Fluorous Technologies” in Como, Italy Poster presentation **Topic: „Influence of adamantane as a host on matrix-isolated MePDF$_3$”**
12/2015	„International Chemical Congress of Pacific Basin Societies” in Honolulu, USA Poster presentation **Topic: „Matrix effects in Matrix Isolation NMR Spectroscopy”**
06/2016	„Chemistry and Physics at low Temperatures” in Biarritz, France Oral Presentation **Topic: „A new approach to NMR-Matrix-Isolation Spectroscopy”**

09/2016	„Wöhlertagung” in Berlin, Germany
	Poster presentation
	Topic: „Matrix-Isolation-NMR spectroscopy and Matrix”